Experimental and Numerical Investigation of Material Characterization and Flow Monitoring in Liquid Composite Molding Processes

by

Barış Çağlar

A Dissertation Submitted to the
Graduate School of Sciences and Engineering
in Partial Fulfillment of the Requirements for
the Degree of

Doctor of Philosophy
in
Mechanical Engineering

KOÇ
UNIVERSITY

March 2017

Experimental and Numerical Investigation of Material Characterization and Flow Monitoring in Liquid Composite Molding Processes

Koç University

Graduate School of Sciences and Engineering

This is to certify that I have examined this copy of a doctoral thesis by

Barış Çağlar

and have found that it is complete and satisfactory in all respects,
and that any and all revisions required by the final
examining committee have been made.

Committee Members:

_____

E. Murat Sözer, Ph.D. (Advisor)

_____

Can Erkey, Ph.D.

_____

Demircan Canadinç, Ph.D.

_____

Véronique Michaud, Ph.D.

_____

Hatice Sinem Şaş, Ph.D.

Date: 21.03.2017

ABSTRACT

Liquid Composite Molding (LCM) processes are widely used for manufacturing Fiber Reinforced Plastic Composites (FRPCs), and most common of these processes are Resin Transfer Molding (RTM) and Vacuum Infusion (VI). In these processes, parts are manufactured by placing a preform of glass or carbon fibers in a mold and impregnating the preform by a thermoset resin. To ensure the part is completely filled without any dry spots and to achieve this in a repeatable manner with predictable flow patterns and cycle times, a good understanding of resin flow through the porous medium is crucial and requires the knowledge of fabric permeability (*i.e.*, inverse of resistance to flow). Thickness distribution in VI varies spatially and with time due to varying resin pressure (thus, compaction pressure) in the mold. In this context, this thesis investigates (i) characterization of the fabric permeability in the presence of rigid inclusions such as microcapsules or fillers and (ii) monitoring and modeling the thickness variation in VI typically consisting of two stages. In the first filling stage, thickness variation increases due to pressure gradient within the mold; and in the second post-filling stage, the excess resin is removed out of the mold to reduce the thickness and the variation in it.

In some cases, a second solid phase, generally in the form of granular particles, may be introduced to FRPCs, to ease the handling of preform, to improve mechanical, thermal and electrical properties, or to functionalize with self-healing capsules (to introduce self-healing capability) or with hollow microspheres (to improve the buoyancy or to decrease the overall weight). The effect of rigid spherical inclusions on the permeability of textile fabrics was investigated by using glass beads as model inclusions. Glass beads with a range of diameters (40 to 800 μm) and volume fractions (2.5 to 10%) were sieved between layers of woven E-glass fabric targeting a constant fiber volume fraction of 40%. Experimental characterization of permeability was followed by X-ray microtomography to reveal the underlying relationship between permeability and microstructural features including pore size distribution, pore shape anisotropy and spatial bead distribution. Furthermore, permeability of the X-ray samples was estimated using Computational Fluid Dynamics simulations and with a Kozeny model taking into account the porosity and the specific surface of samples, and compared with the experimental permeability results.

Thickness variation in VI and its minimization is usually dealt with a trial and error based approach. This study offers an alternative approach to overcome this drawback of VI process, by integrating thickness monitoring and resin flow modeling in a flexible mold. A Structured Light Scanning system was verified for its suitability of monitoring thickness during VI and was used for full field thickness monitoring in experiments. A Control Volume Finite Element Method (CVFEM) solver, capable of coupling resin flow, fabric compaction and permeability, was implemented. Two different scenarios were studied experimentally and numerically. Full field thickness, resin pressure at some locations and mass of the infused resin were recorded

during filling and post-filling stages of experiments; and simulations were performed with corresponding process parameters. Thickness monitoring system was able to capture the instantaneous thickness distribution of the specimen as well as its evolution during the experiments. Thickness variation within the specimen reached its maximum at the end of mold-filling due to the high resin pressure at the inlet (thus low compaction pressure) compared to vacuum pressure at the exit. The thickness variation was reduced in the post-filling stage by removing the excessive resin and almost equalizing resin pressure. Simulations resulted in a reasonably close estimation of fill time and infused resin mass. Evolution of pressure was simulated successfully as well as the resulting thickness distribution. The thickness variation increased in filling stage and the effects of post-filling actions were in agreement with the experimental results.

ÖZETÇE

Sıvı Kompozit Kalıplama (LCM) yöntemleri Fiber Takviyeli Plastik Kompozit (FRPC) üretimi için yaygınca kullanılmaktadır ve bu yöntemlerin en çok kullanılanları Reçine Trasnfer Kalıplama (RTM) ve Vakum İnfüzyon (VI) yöntemleridir. Bu yöntemlerde, cam veya karbon elyaf bazlı kumaş katmanları kalıp içerisine yerleştirilip, kalıp kapatıldıktan sonra, termoset reçine ile ıslatılmaktadır. Kalıbın kuru yer kalmayacak şekilde doldurulması ve bunun tekrar edilebilirliğinin sağlanması, yani öngörülebilir bir akış ilerleyişiyle, yaklaşık olarak tahmin edilen bir sürede başarılabilmesi için kumaş geçirgenliğinin (yani akış direncinin tersi) doğru karakterize edilmesi gerekmektedir. Ayrıca, VI yönteminde üst kalıp olarak plastik bir torba kullanılmasından ötürü kalıp içerisindeki reçinenin basıncı (dolayısıyla sıkıştırma basıncı) hem konuma hem de zamana bağlı olarak değişmektedir. Bu bağlamda, bu tezde şu konularda inceleme yapılmıştır: (i) elyaf katmanları arasında mikrokapsüller ya da dolgular gibi katı takviyelerin varlığında geçirgenliğin karakterizasyonu ve (ii) kalınlık varyasyonunun basınç dağılımına bağlı olarak arttığı dolum aşaması ve fazla reçinenin kalıptan çıkarılarak kalınlığın ve kalınlık varyasyonunun azaltıldığı dolum sonrası aşamalarından oluşan VI üretim yönteminde, kalınlık değişiminin deneysel olarak gözlemlenmesi ve modellenmesi.

Fiber Takviyeli Plastik Kompozit'lere bazı durumlarda parçacıklar halinde katkı maddeleri katılabilir. Örneğin, elyaf katmanlarının bir arada durmasını sağlamak, mekanik, termal ve elektrik özelliklerini değiştirmek veya kompozitlere ek bir fonksiyonu mesela öz-iyileşme özelliği veya batmazlık özelliği katmak amacıyla çeşitli mikroparçacıklar katılmaktadır. Bu çalışmada, katı takviyelerin kumaş geçirgenliği üzerindeki etkisi kumaş katmanlarının arasına cam tozu eklenerek incelenmiştir. Farklı çaplar (40-800 μm) ve hacim oranlarındaki (%2.5, %5, %10) cam tozları, %40 hacim oranındaki örgü cam elyaf katmanları arasına mikroelek kullanılarak elenmiştir. Geçirgenliğin deneysel karakterizasyonunun yanı sıra, X ışınları mikrotomografisi (μ-CT) aracılığıyla mikroyapı incelenmiş ve geçirgenlik ile boşluk boyut dağılımı, boşluk anizotropisi, ve cam tozu dağılımı arasındaki ilişki araştırılmıştır. μ-CT ile elde edilen görüntüler üzerinde Hesaplamalı Akışkanlar Dinamiği (CFD) ve boşluk oranı ile spesifik yüzey alanını baz alan Kozeny modeli kullanılarak geçirgenlik hesaplanmış ve deneysel sonuçlarla karşılaştırılmıştır.

VI yönteminde karşılaşılan kalınlık varyasyonunun anlaşılması ve azaltılması genellikle deneme-yanılma yoluyla olmaktadır. Bu çalışmada, kalınlığın deneysel olarak takibi ve kalınlık değişimini hesaba katan akış modellemesi kullanılması yoluyla, deneme-yanılma bazlı yaklaşıma bilimsel bir alternatif sunulmuştur. Yapısal Işıkla Tarama (SLS) temelli bir sistem, bu ihtiyaca uygunluğu doğrulandıktan sonra, deneylerde parçanın tamamındaki kalınlık değişimini takip etmek için kullanılmıştır. Kontrol Hacmi Sonlu Eleman Metodu (CVFEM) temelli ve geçirgenlik ile sıkışmanın basınca göre değişiminin hesaba katıldığı bir sayısal çözüm geliştirilmiştir. İki farklı senaryo, deneysel ve sayısal olarak incelenmiştir. Deneylerin dolum ve dolum sonrası aşamalarında, kalınlık dağılımı, reçine basıncı ve kalıba

giren reçine miktarı ölçülmüş ve simülasyonlar aynı sınır koşulları ve üretim parametreleri kullanılarak gerçekleştirilmiştir. Kalınlık tarama sistemi kalınlığın anlık dağılımının yanı sıra, zaman içindeki değişimini de başarıyla ölçmüş ve deneylerde kalınlığın reçine girişine yakın bölgelerde deney süresince artan reçine basıncı (dolayısıyla azalan sıkıştırma basıncı) nedeniyle arttığını, ve reçinenin en son ulaştığı çıkışa yakın bölgelerle arasındaki kalınlık farkının dolum aşamasının sonunda en yüksek düzeye ulaştığını göstermiştir. Benzer şekilde, dolum sonrası aşamada, reçine basıncının tüm kalıpta neredeyse eşitlenmesi sonucunda, kalınlık varyasyonu önemli derecede azalmıştır. Simülasyonlarda elde edilen kalıp dolum süreleri ve kalıba giren reçine miktarları deneysel sonuçlarla uyum içindedir. Bunun yanı sıra, kalınlık dağılımının dolum aşamasındaki artışı ve dolum sonrası aşamadaki azalışı da başarıyla modellenmiştir.

ACKNOWLEDGEMENTS

I am grateful to my advisor Prof. E. Murat Sözer for his support and guidance throughout my long-lasting career at Composite Materials Manufacturing Laboratory (CMML), for granting me the freedom to explore new directions throughout my doctoral studies, for his patience and understanding at hard times and for his heartfelt advices when most needed. I would also like to thank members of my thesis committee Prof. Can Erkey, Prof. Demircan Canadinç, Prof. Véronique Michaud and Prof. Hatice Sinem Şaş for their critical reading, invaluable feedback and insightful comments.

I would also like to thank to the staff of College of Engineering (Derya Ernur, Türkan Eryiğit) and Graduate School of Sciences and Engineering (Elif Tüysüz, Emine Büyükdurmuş) for providing a comfortable working environment and for their support.

Many thanks are also due to TÜBİTAK (The Scientific and Technical Research Council of Turkey) for funding my doctoral studies at Koç University, Istanbul, Turkey through BİDEB Program.

As the saying goes: "It is good to have an end to journey toward, but it is the journey that matters in the end." Throughout my journey, I came across with great people who touched my life one way or the other. Among

these, I would like to thank the former and the current group members of CMML, in no particular order, Dr. Bekir Yenilmez, Talha Akyol, Akif Yalçınkaya, Mustafa Haboğlu, Mert Hancıoğlu, Cem Tekin and Hasan Çağlar who have always been there not only as colleagues and also as true friends. I would like to thank Dr. Güray Kuzu, Dr. Utku Boz, Dr. Engin Çukuroğlu, Yılmaz Adal, Halit Bayer, Bekir Aksoy and Gökçen Göksel for providing a peaceful off-work environment and for the true friendship. I would also like to thank Dr. Mehmet Ali Yatbaz, Enis Sert and Prof. Yusuf Sahillioğlu for all the moments and experiences we shared.

I owe sincere and earnest thankfulness to Prof. Véronique Michaud for the opportunity to experience the great working environment at LPAC (late LTC) with extraordinary people. I am thankful to all my colleagues at LPAC for all the experiences, especially to Damiano Salvatori, Matteo Marascio, Amaël Cohades, Dr. Yonghoon Yoon, Dr. Feyza Karasu Kılıç, Dr. Federica Sordo and Dr. Azadeh Khoushabi.

My deepest gratitude is to my family, my father Ferhat, my mother Ruhan, my sister Dilek, my brother-in-law Fatih, my niece Elif, my sister Nuran and my little (!) brother Hasan for their support and unconditional love. Lastly, I am blessed to have my dear Büşra in my life. I would like thank her for being my inspiration, for her infinite belief in me and for her encouragement to always aim higher.

TABLE OF CONTENTS

LIST OF TABLES

LIST OF FIGURES

1. INTRODUCTION

1.1. Liquid Composite Molding

Fiber-Reinforced Polymer Composites (FRPCs) are manufactured with a reinforcement material (usually carbon or glass) and a polymer matrix. These materials are extensively used in aerospace, automotive, sporting goods and other applications due to their high strength, stiffness and light weight in comparison to traditional materials. They are manufactured by adapting a variety of techniques offering different initial investments, production rates and final properties [1]. In processes like injection molding, compression molding and extrusion, short fibers (aspect ratio less than 100) are blended within the polymer matrix. Even though these processes allow manufacturing of parts with very complex geometries, the use of short fibers limit the mechanical properties. On the other hand, the use of continuous fibers allows production of parts with relatively less complex geometries and significantly better mechanical properties which can be used in structural load-bearing applications.

Main routes for manufacturing the "advanced composites" made of continuous fibers is Autoclave Processing and Liquid Composite Molding. In Autoclave Processing, pre-impragnated layers of fabrics are placed in pre-determined orientations and consolidated in an autoclave under high

pressure (up to 6 bar) at high temperatures (up to 200°C). Even though, the use of autoclave allows the evacuation of air and excess resin which in turn provides superior mechanical properties, this process requires a high initial investment of autoclave and manufacturing of large parts with this processing route is not very feasible.

Conversely, Liquid Composite Molding (LCM) processes offer the capability to manufacture complex parts for semi-structural and structural components at low-cost investments. The two most common LCM techniques are Resin Transfer Molding (RTM) and Vacuum Infusion (VI, a.k.a. Vacuum Assisted Resin Transfer Molding (VARTM)).

1.1.1. Resin Transfer Molding (RTM)

Figure 1.1 shows the steps of RTM process. Firstly, layers of dry fabric are cut to desired dimensions and then placed onto lower mold and compacted to the final thickness by the upper mold. Resin is then injected into the mold, to fill the cavities in the preform, by an injection machine which operates under pressure or flow rate control. Part is kept in the mold until resin cures partially, and then it is demolded. Two sided mold allows manufacturing parts with a good surface finish and high fiber volume fractions, ϕ_f. Thus, RTM is preferred for manufacturing structural parts at mid to high production rates.

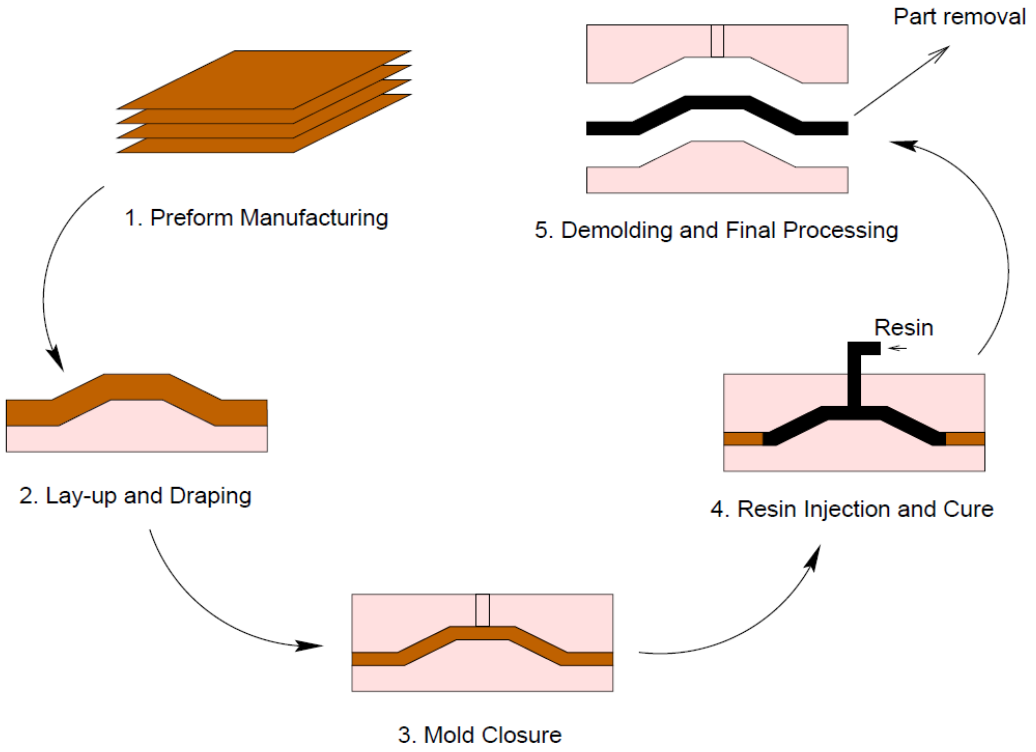

Figure 1.1 Schematic of the steps in RTM process [1].

To achieve a desired cycle time and ensure the complete impregnation of the part, a good understanding of the flow propagation and resin curing is necessary in RTM process [2–4]. For this need, resin flow modeling enables to estimate the fill time and predict the flow pattern. Several numerical simulation tools have been developed in order to optimize the mold design as well as the production cycle [5–8]. The most common approach is to couple Darcy's law and continuity equation. Darcy's law represents the flow through a porous medium as follows:

$$\vec{u} = -\frac{1}{\mu}\begin{bmatrix} K_{xx} & K_{xy} \\ K_{yx} & K_{yy} \end{bmatrix}\begin{Bmatrix} \partial P/\partial x \\ \partial P/\partial y \end{Bmatrix} = -\frac{1}{\mu}[K]\cdot\nabla P \qquad (1.1)$$

where $\vec{u}$ is the average fluid velocity or Darcy's velocity, $\vec{u} = u\hat{\imath} + v\hat{\jmath}$ for 2D flow (since composites are usually thin parts and flow is in the in-plane directions), μ is the viscosity of the liquid resin, $[K]$ is the in-plane

permeability tensor of the porous medium and P is resin pressure. Darcy's velocity is related to the superficial resin velocity, $\vec{u}_r$, by

$$\vec{u} = \phi_p \vec{u}_r \tag{1.2}$$

where ϕ_p denotes porosity and related to fiber volume fraction ϕ_f as $\phi_p = 1 - \phi_f$. Flow of an incompressible fluid in infinitesimal volume with height, h, continuity equation is as follows [9]:

$$\frac{\partial h}{\partial t} + \nabla \cdot (h\vec{u}) = 0 \tag{1.3}$$

1.1.2. Fabric permeability

In Eq. (1.1), permeability tensor defines the inverse of resistance of the porous bed to the flow and should be characterized in advance for accurate prediction of flow pattern. Permeability is characterized either by one-dimensional rectilinear flow experiments along each of the two principal directions of the permeability [10–13] or a radial flow experiment [11,14–17]. Radial flow experiments provide the two principal permeability values simultaneously, while one-dimensional (or linear) rectilinear flow experiments are usually preferred since the experiments are easier to set-up, saturated and unsaturated permeability for a pre-determined volume fraction can be obtained from a single experiment, and reproducibility of the results is high with standardized test equipment and procedure [11].

In linear permeability experiments with constant injection pressure, unsaturated permeability is calculated by recording the flow propagation and flow front arrival to pre-determined locations to construct the flow front location (x_{ff}) versus time (t) curve. The following equation is then used to obtain the unsaturated permeability following the Squared Flow Front (SFF) approach

$$K_{SFF} = \frac{m\phi_p\mu}{2P_{inj}} \tag{1.4}$$

where P_{inj} is the injection pressure and m is the slope of the x_{ff}^2 versus t curve, x_{ff}^2 being the square of x_{ff}. Once the rectangular mold is filled, flow rate (Q) of the fluid coming out of the mold is recorded and used to calculate the saturated permeability as follows:

$$K_{sat} = \frac{Q\mu L}{AP_{inj}} \tag{1.5}$$

where L and A are the length and the cross-sectional area of the fabric specimen in the mold cavity, respectively.

1.1.3. In-plane permeability and microstructure of fabrics in the presence of inclusions

In some cases, a second solid phase, generally in the form of granular particles, may be introduced to FRPCs. As an example, reactive or non-reactive binders (or tackifiers) are introduced at the preforming stage to ease the handling of multiple layers of reinforcement and improve the efficiency of processing [1,18]. Particles may also be integrated to the polymer matrix to improve mechanical, thermal and electrical properties [19–23]. In addition, for composite functionalization, self-healing capsules are sieved between the layers of reinforcement [24,25], hollow microspheres are introduced to improve the buoyancy or to produce lightweight parts [26,27], and powders are added to tailor capillarity effects in porous structures [28].

The effect of the presence of a second solid phase on the mechanical properties of FRPCs has been extensively investigated and reported in the literature [18,19,24–26,29–34]. It is also well known that additional solid

phases in FRPCs alter the manufacturing processes. For instance, in the Liquid Composite Molding (LCM) processes, where a fibrous preform is compacted in a mold and resin is injected into the preform, the preform should be fully impregnated before resin gelation [9]. Hence, an accurate estimate of the permeability of a fibrous structure is essential to predict the flow kinetics and mold filling time [10,11,35,36]. Studies on the flow of particle blended matrix show that introduction of particles increases the viscosity of suspension and particles are clogged progressively during processing which results in spatially varying permeability [37–39]. Flow is either modeled by coupling the resin flow with particle filtration by a retention function [40–43] or by simulating the solid-liquid interaction at individual particle level [44–46].

In the case of functionalization by introducing a second solid phase between the layers of fabric, both in-plane and out-of-plane permeabilities are influenced. Out-of-plane is typically one to two order of magnitude lower than the in-plane permeability [47]. For investigation of influence of inclusions on permeability, Shih and Lee [48] studied the tackification of carbon fiber woven fabrics and used PT 500 binder from 3M with various binder size between 25 μm and 1000 μm. They noted that smaller powders tended to have a better coverage of the fabric surface and showed that holding the preforms at temperatures higher than the melting temperature of the binder resulted in an increase of the in-plane permeability. Similar to Rohatgi and Lee [49], they explained the increase of permeability by the shrinkage of fiber tows following the penetration of molten binder which results in larger channels outside the fiber tows. Both studies showed that if the system was held at low temperatures, binder stayed between the fiber tows and caused a decrease of permeability at high binder concentrations.

Estrada et al. [50] investigated the binder influence by modeling the flow in unit cells obtained from micrographs of cut specimens. Unit cell based model resulted in different permeabilities in principal directions of the anisotropic fabric, but was limited in permeability value prediction mainly because the unit cell lacked the repeatability due to distribution of binders and the selection of a coarse grid. Recently, Becker and Mitschang [51] investigated the influence of preforming technologies (sewing, binder application, shearing and pre-compaction) on out-of-plane permeability and they reported that out-of-plane permeability of a glass fiber woven fabric decreased by addition of both activated and not activated binders. Results showed a lower permeability with activated binder since activated binders caused a more homogenous reduction of available space while not activated binders hindered nesting thus some flow channels remained available. In another study [52], they studied the out-of-plane permeability of preforms manufactured by dry fiber placement, which exhibit one to two order of magnitude lower out-of-plane permeability than conventional fabrics and they investigated the potential strategies to enhance the out-of-plane permeability of these preforms. They studied the effect of binder particle size by sieving three different particle size ranges: medium sized (125-250 μm), coarse (>250 μm) and mixed (in delivery condition) at same concentration. Highest permeability was observed with the medium sized particles and they discussed that coarse binders were expected to result in a higher permeability by impeding nesting, but a lower number of binder particles was introduced at same concentration thus the positive effect of sieving large particles was reduced. They also studied the influence of binder concentration by sieving different amounts of mixed (in delivery condition) binders and reported that a slight increase was observed with increasing binder concentration, but

positive effects of preserved flow channels was counteracted by blockage of resin flow at high concentrations.

Contrary to the binders whose effect on permeability and microstructure depend on the degree of melting, particle size and concentration; self-healing capsules are rigid inclusions and Manfredi and Michaud [53] investigated the influence of capsule concentration on in-plane permeability by sieving capsules with a size of 125-250 μm. They reported an increase of permeability by addition of self-healing capsules in comparison to samples with no capsules, but without a correlation between capsule concentration and permeability.

1.1.4. Vacuum Infusion (VI)

Vacuum Infusion (VI, or Vacuum Assisted Resin Transfer Molding, VARTM) is a variant of RTM and the main difference of this process is the use of a plastic bag as the upper mold instead of a rigid mold. Process steps of VI are shown in Figure 1.2. Firstly, layers of dry fabric are cut to desired dimensions and then placed onto lower mold. After placing the inlet and vent tubes, a plastic bag is placed to cover the preform and sealed to the lower mold by a sealant tape. In the next step, a vacuum is applied to the mold and the preform is compacted. In addition, applied vacuum creates the pressure differential which allows driving the resin into the preform.

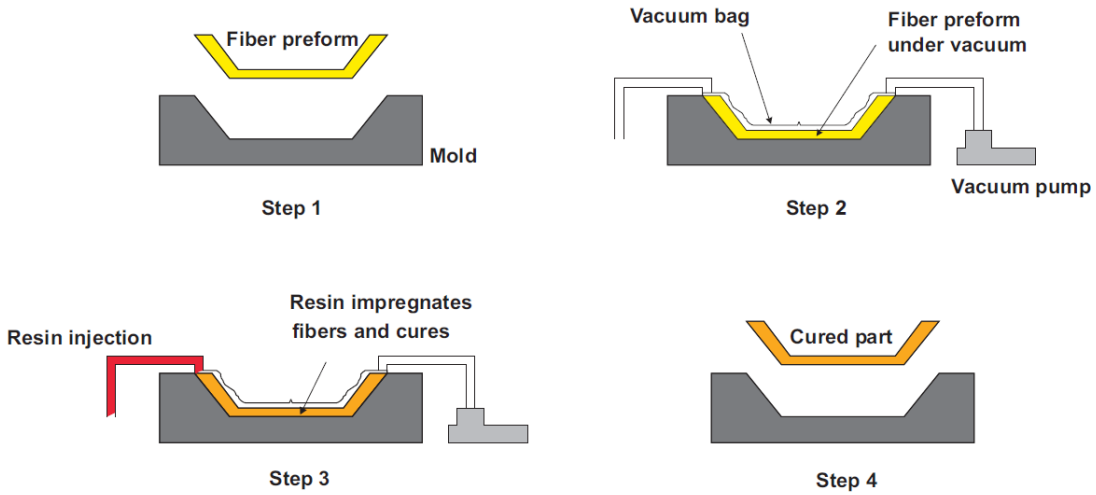

Figure 1.2 Schematic of the steps in VI process [1].

The use of a vacuum bag as an upper half mold decreases the overall tooling cost significantly and allows the visual tracking of flow front propagation during infusion. However, pressure differential cannot exceed 1 bar, thus requires the optimization of inlet and vent design to optimize the cycle time and ensure complete mold-filling without dry spots. Optimization of cycle time is achieved by carefully designing the placement of inlet tubes and highly permeable layer [54–56] and can be linked to minimization of dry spots [56]. Formation and transport of microscale voids in FRPCs is linked to the unsaturated flow as summarized in [57,58].

Prior to infusion, whole preform is under the same compaction pressure (see Figure 1.3 for definition of compaction pressure). However, once the resin reaches a particular location and then propagates away, compaction pressure starts decreasing with time (*i.e.*, resin pressure increases), which in turn results in a spatially varying thickness distribution. The relationship between resin pressure, P, compaction pressure, P_c and thickness is shown in Figure 1.3.

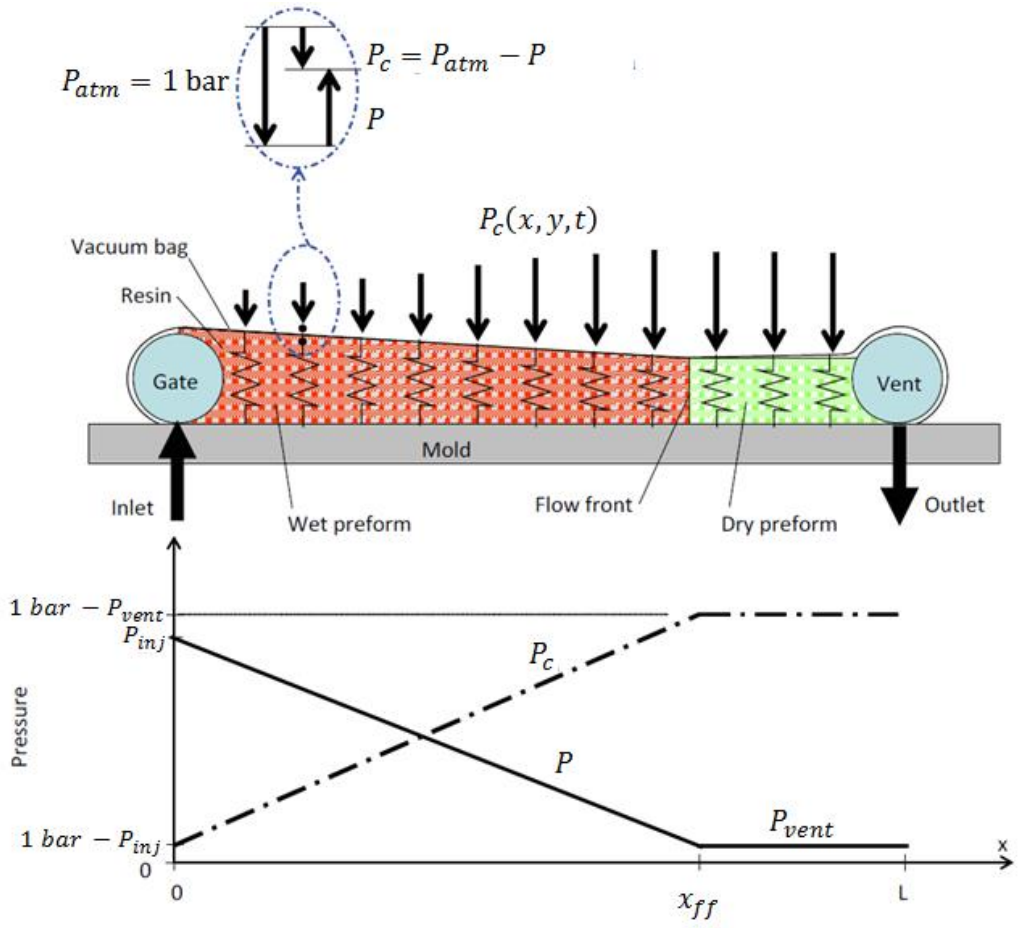

Figure 1.3 Spatially varying resin pressure, P, and compaction pressure, P_c [1].

1.1.5. Modeling of thickness in VI

To achieve the thickness with acceptable dimensional tolerances, a good understanding of the relationship between the part thickness and the compaction pressure (*i.e.* compaction behavior) is essential. To couple the resin flow and compaction behavior, several studies experimentally characterized the compaction behavior and integrated it with the resin flow simulation tools. In addition to the studies where an analytical solution is attempted [59–62], some researchers also used commercially available Resin Transfer Molding (RTM) simulation tools (e.*g.* LIMS, PAM-RTM or others) for the analysis of VI or validation of VI models [63–65] by introducing

additional subroutines to consider the pressure dependency of the thickness. The most common approach in modeling the resin flow in LCM is to couple the pressure and thickness distributions, using finite element based solvers [4,9,66–69]. In these solvers, resin pressure solution obtained by Finite Element Method (FEM) solution is coupled with a flow propagation algorithm using Control Volumes (CV), and this combined approach is called Control Volume Finite Element Method (CVFEM). In literature, it was reported that the mass balance was achieved for 1D flow while mass imbalance issues arise for 2D and 3D flow due to discretization of flow surface [65,70]. Temporally and spatially varying nature of thickness in VI necessitates the integration of refinement algorithms to resin flow simulation tools in order to gain the capability of modeling the evolution of thickness distribution and flow front propagation accurately while minimizing the mass imbalance. To this end, several researchers offered ways to minimize the mass imbalance as well as improving the flow front update scheme, mostly by refining and/or adapting mesh [70–73] or by defining floating nodes [74], all coming at an expense of computational load. In this study, a new solution approach will be exploited to combine resin pressure distribution and flow front propagation in filling and post-filling stages of VI by coupling the compaction behavior and resin pressure while advancing the pressure distribution and flow front at small time intervals without refining the existing mesh.

1.1.6. Monitoring of thickness in VI

For experimental investigation of evolution of thickness distribution during VI, researchers employed various methods. In several studies [75–78], dial gages have been used for measuring the part thickness during part

manufacturing as well as measuring the thickness in compaction experiments. However, use of dial gages are limited due to several reasons: (1) owing to the fact that, despite the magnitude is small, dial gages apply a force on the fabric which may result in a thickness measurement error; (2) taking measurements from multiple points is troublesome since each dial gage takes a certain space, making it difficult to use multiple dial gages in a limited space. A more practical approach for thickness measurement is to use non-contact laser displacement sensors [79,80]. This type of sensor is useful for measuring the time dependent thickness at a certain location, thus have limited capability in terms of capturing the inherent variation within the fabrics. If full field measurement of thickness is desired using laser displacement sensors, they need to be carried between successive measurements by integrating them with a mobile platform. However, sample rate decreases significantly since it takes a certain amount of time for the mobile platform to complete one cycle and return to the same location [81]. Optical methods have proven to be useful for full field measurement of thickness in VI. These non-contact methods are based on either the use of multiple cameras as in the case of speckle stereophotogrammetry [82–85] or the use of a projector and a camera for Structured Light Scanning systems [86]. Feature matching between the stereo images is the main hurdle in speckle stereophotogrammetry method and it does not guarantee that the same points (features) will be matched in measurements at different times [87]. Conversely, Structured Light Scanning systems are based on reflecting pre-determined fringe patterns on a surface and they capture the detected fringe patterns to estimate the depth map.

1.2. Objectives & Outline of the Thesis

This thesis focuses on the processing of Fiber Reinforced Plastic Composites (FRPCs) by Liquid Composite Molding (LCM) techniques and investigates the impregnation phase where the cavities within the fabric preform are filled with a resin. In both Resin Transfer Molding (RTM) and Vacuum Infusion (VI), fabric permeability determines the flow pattern during impregnation and the fill time, and it should be well characterized to ensure complete filling. Permeability is subject to change by inclusions and requires an in-depth analysis to reveal the relationship between the permeability and microstructure. A final part should not only be fully impregnated but also have desired dimensional tolerances. In this context, thickness distribution in VI requires attention since it varies spatially and with time, contrary to RTM where thickness is constant (*i.e.*, does not vary with time) and dictated by the rigid mold parts.

In Chapter 1, RTM and VI are introduced and literature review on following subjects are reported: (i) permeability characterization and investigation of microstructure in the presence of inclusions, (ii) modelling of thickness variation in VI and (iii) monitoring of thickness variation experimentally (during both mold filling and post-filling stages).

Influence of spherical rigid inclusions on microstructure and permeability of a woven fabric is investigated in Chapter 2. In addition to experimental characterization of permeability in the presence of inclusions with different concentrations and diameter ranges, X-ray microtomography measurements are conducted to estimate the permeability by (i) Computational Fluid Dynamics simulations, and (ii) a semi-analytical approach based on Kozeny equation. In addition, spatial distribution of

beads, pore shape anisotropy and pore size distribution are analyzed and their relationship with fabric permeability is revealed.

In Chapter 3, a full field thickness monitoring system is integrated to an experimental VI setup. Thickness distribution, pressure at several locations and mass of the infused resin are analyzed in two different scenarios. A numerical simulation tool is developed to combine resin flow with the spatially and temporally varying thickness by considering the permeability and compaction models. Experimental and numerical results are analyzed to assess the capabilities and limitations of the thickness monitoring system and of the numerical simulation tool.

Chapter 4 is devoted to summarizing the main findings of this thesis and to presenting an outlook for future work.

2. IN-PLANE PERMEABILITY AND MICROSTRUCTURE OF TEXTILE FABRICS WITH SPHERICAL INCLUSIONS

2.1. Introduction

Studies on the permeability in the presence of rigid inclusion is limited and the novelty of this work is the investigation of the effect of the second phase content, morphology, granulometry and spatial distribution on both the porous structure topology and permeability to develop general guidelines and constitutive models to optimize flow kinetics, a feature which lacked in the composites literature.

This study, thus, investigated the effect of rigid inclusions on both the porous structure and the permeability of textile fabrics, by introducing spherical glass beads with a range of bead volume fractions and diameters. The 3D porous structure of the reinforcements and the role of the beads were finely characterized using X-ray microtomography. In parallel, the in-plane permeability of the reinforcements was estimated using both in-plane permeability experiments and pore-scale Computational Fluid Dynamics (CFD) simulations using the scanned volumes from microtomography analysis. Guidelines were then provided to assess the effect of inclusion size

and inclusion volume fraction on the textile permeability, as a function of the microstructural features of the textile.

2.2. Materials and methods

2.2.1. Materials

A 2×2 twill weave E-glass fabric (Suter Kunststoffe AG) with a superficial density, $\rho_{sup} = 390$ g/m^2 and a fiber specific mass, $\rho_{bulk} = 2.60$ g/cm^3 was used in this study. The fabric properties were given as follows by the manufacturer: fabric was made of fibers with a diameter of 9 μm and consisted of 6 ends/cm along warp direction and 6.7 picks/cm along weft direction with 340 and 272 tex, respectively. Rounded glass beads (Microbeads AG) with specific mass, $\rho_b = 2.45$ g/cm^3 were used as model inclusions. As summarized in Table 2.1, various bead diameter ranges, d_b, were used (40-70, 70-100, 100-200, 200-300, 300-400, and 400-800 μm), as well as various bead volume fractions, ϕ_b (2.5, 5.0 and 10%). Figure 2.1(a-b) shows two typical micrographs corresponding to the 40-70 and 100-200 μm beads. The bead-diameter distributions in Figure 2.1(c) were calculated from the micrographs using the Matlab function *imfindcircles* (~7600 beads were examined under a microscope for 40-70 μm range, and similarly ~4200 beads for 100-200 μm range).

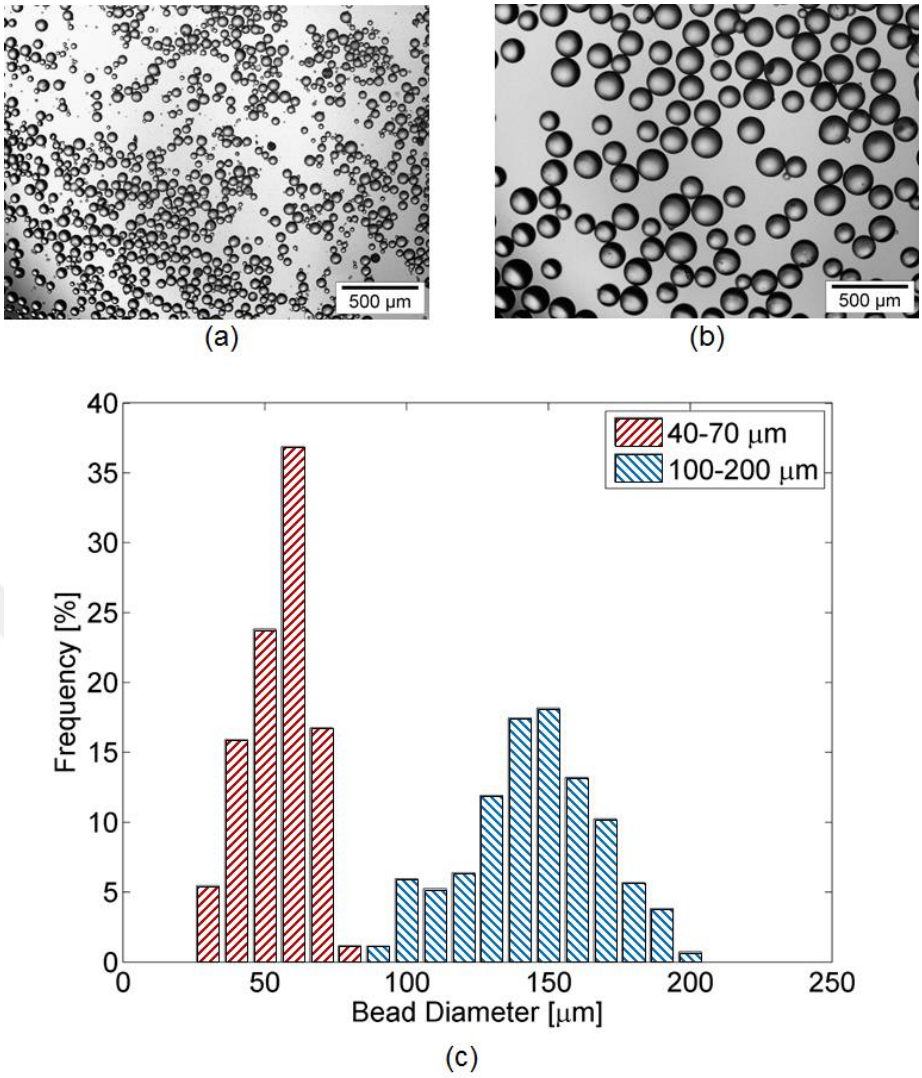

Figure 2.1 Optical micrographs of beads with two different diameter, d_b ranges: (a) 40-70 μm, (b) 100-200 μm. (c) Corresponding diameter distribution of the beads.

Table 2.1 Experimental, numerical and normalized permeability, and specific surface results of studied configurations.

Sample #	Bead Properties		Permeability, K [10^{-11} m^2]		Specific Surface, S [10^3 m^{-1}]	Normalized Permeability, K^*		
	Bead Diameter, d_b [μm]	Bead Volume Fraction, ϕ_b [%]	Experiment, K_{exp}	Simulation, K_{num}		Experiment, K^*_{exp}	Simulation, K^*_{num}	Semi-Analytical, K^*_S
1	0	0	7.92	12.2	6.31	1.00	1.00	1.00
2	40-70	2.5	6.50	11.4	5.98	0.82	0.93	0.98
3		5.0	4.04	5.77	8.05	0.51	0.47	0.47
4		10	1.86	4.29	10.1	0.23	0.35	0.23
5	70-100	5.0	3.71	6.78	7.32	0.47	0.56	0.57
6	100-200	2.5	4.96	9.70	6.20	0.63	0.80	0.91
7		5.0	3.89	7.29	7.01	0.49	0.60	0.62
8		10	3.01	5.40	7.22	0.38	0.44	0.44
9	200-300	5.0	5.65	10.6	6.05	0.71	0.87	0.84
10	300-400	5.0	5.94	10.6	5.67	0.75	0.87	0.95
11	400-800	2.5	6.05	12.2	5.78	0.76	1.00	1.05
12		5.0	6.50	13.3	5.62	0.82	1.09	0.97
13		10	6.84	12.1	5.01	0.86	0.99	0.92

The samples consisted of $n = 8$ layers of fabrics. During sample preparation, the prescribed mass, m_b, of beads was manually sieved between adjacent layers and the resulting stack was then compacted in a mold of volume V_m and thickness $h = 3$ mm. The volume fractions of fibers ϕ_f, of beads ϕ_b, as well as the porosity ϕ_p of processed samples could thus be estimated as $\phi_f = (n\rho_{sup})/(h\rho_{bulk}) = 40.0 \pm 0.1\%$, $\phi_b = m_b/(\rho_b V_m)$, and $\phi_p = 1 - \phi_f - \phi_b$ (see Table 2.1). For the permeability experiments, samples had rectangular in-plane dimensions, *i.e.*, 260 mm along the weft direction (the direction along which the permeability was measured, see below) and 60 mm along the warp direction. For X-ray microtomography analysis (see below), the in-plane shape of samples was circular with a 40 mm diameter.

To characterize the permeability of the samples, a solution of polyethylene glycol (PEG, Sigma Aldrich, 35000 molar mass) was diluted in distilled water with a concentration of 5.7 mmol l^{-1} to form the test fluid. The shear viscosity μ of the PEG solution was measured using a Couette rheometer (AR 2000ex, TA Instruments) in continuous flow mode. For characterization of temperature dependency between 18°C and 25°C, temperature was increased with a ramp of 0.1°C min^{-1} and viscosity was measured at a constant shear rate of 1 s^{-1}. For shear rate dependency between 0.1 s^{-1} and 100 s^{-1}, the viscosity was measured at a constant temperature of 20°C. The PEG solution exhibited a Newtonian behavior as illustrated in Figure 2.2 in which the shear viscosity μ *versus* temperature and shear rate was plotted.

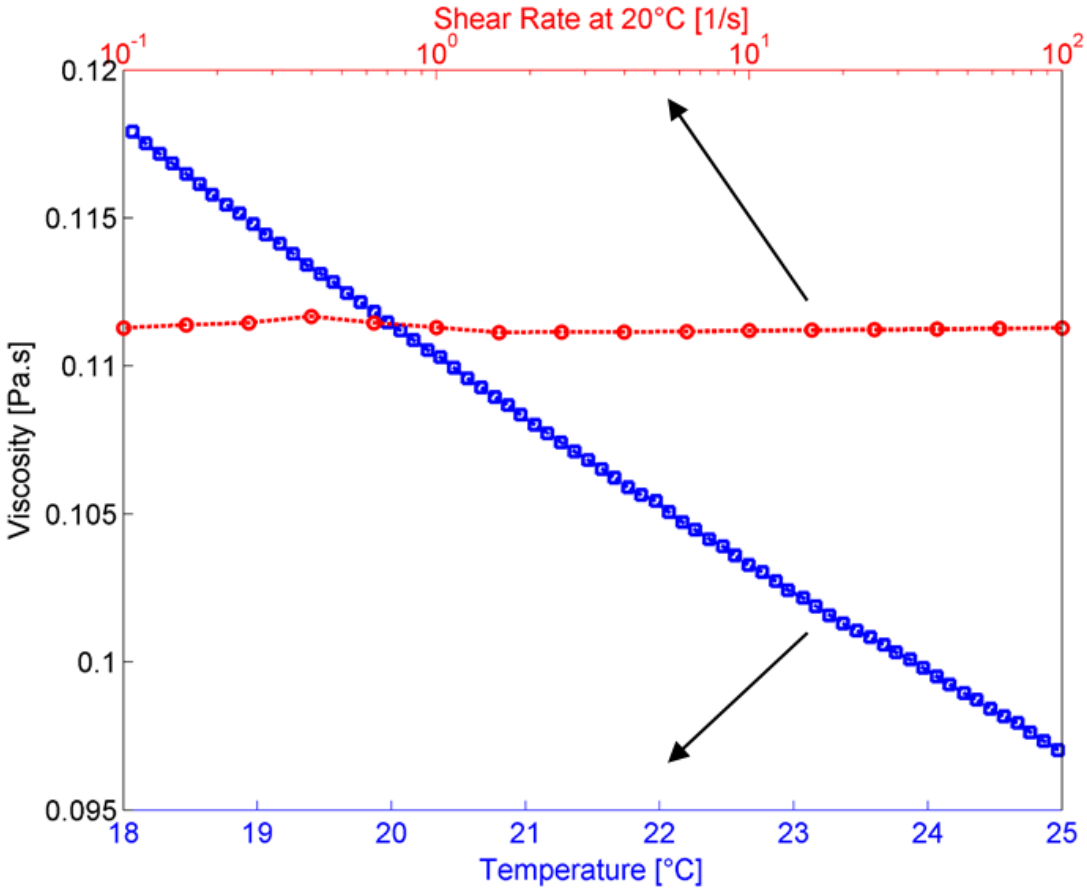

Figure 2.2 Shear viscosity μ of the tested PEG solution as a function of temperature (blue data) and shear rate (red data).

2.2.2. *Permeability experiments*

Permeability measurements along the weft direction of the fabrics were conducted under constant injection pressure using the mold illustrated in Figure 2.3(a-b). The guidelines proposed in a recent round-robin study for 1D flow was followed [10] except that a different test-fluid was used. The saturated permeability, denoted as K_{exp}, was measured in all experiments and to this end injection pressure, p, as well as the temperature of the test fluid were recorded by a Keller S35X piezoresistive transmitter (0 - 10 bar, 0.02 bar accuracy for pressure, -20 - 150°C, 0.05% relative accuracy for temperature) placed between the pressure pot and resin inlet. A Mettler

Toledo PM2500 scale was placed at the exit to record the mass with an accuracy of 0.001 g at a data acquisition rate of 8 Hz. Mass flow rate was calculated using the acquired mass and time data; additionally, the density of resin was used for calculating the volumetric flow rate, Q. The saturated permeability was then calculated as $K_{exp} = (Q\ \mu\ L)/(Ap)$, L being the specimen length along the flow direction (260 mm) and A its cross-sectional area (60 mm x 3 mm).

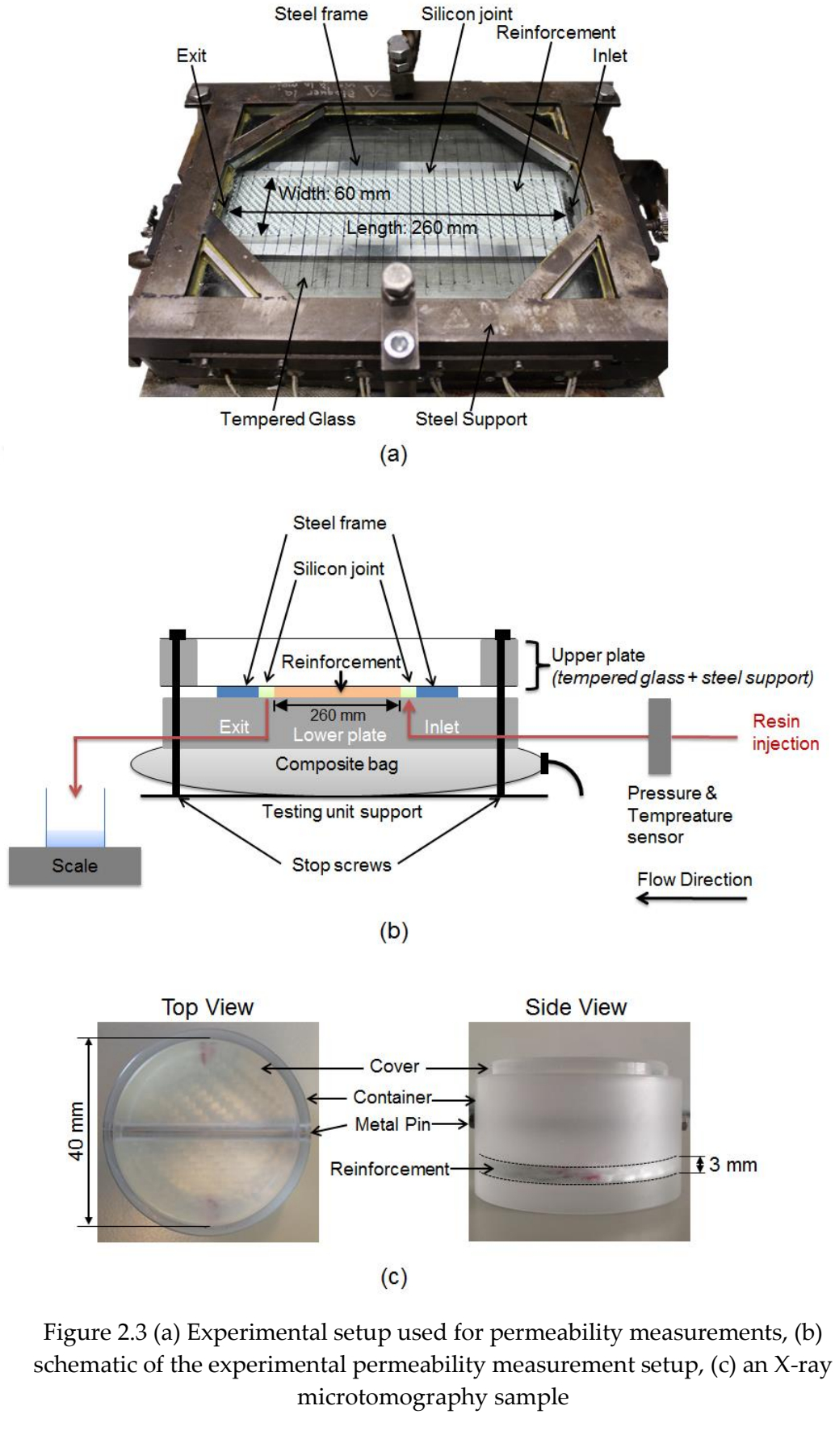

Figure 2.3 (a) Experimental setup used for permeability measurements, (b) schematic of the experimental permeability measurement setup, (c) an X-ray microtomography sample

In order to determine the permeability of the plain fabric (without bead) for a range of fiber volume fractions, the experiments initially conducted at h = 3.0 mm were also carried out at h = 2.8 and 2.5 mm, and the following empirical exponential relation between K_{exp} and ϕ_f (a first order polynomial relation between $\ln K_{exp}$ and ϕ_f) was fitted to the experimental data

$$K_{exp} = Ae^{-b\phi_f} \tag{2.1}$$

by a least-square method to determine the constants A and b.

2.2.3. X-ray microtomography

2.2.3.1. Image acquisition

Cylindrical fabric samples with a diameter of 40 mm were prepared for all configurations listed in Table 2.1, inserted into cylindrical PMMA containers and compacted to the same thickness, h, of 3 mm as in the permeability experiments, with help of cylindrical PMMA covers held in place with pins (see Figure 2.3(c)). The samples' microstructures were characterized using a laboratory X-ray microtomograph (RX Solutions, 3SR Lab, Grenoble, France). To acquire the 2500 radiographs of size 1840 × 1456 pixels during the 360° rotation of samples with respect to the X-ray source, the generator voltage and the current intensity were set to 120 kV and 83 μA, respectively. After suitable reconstruction, filtering and smoothing operations, 3D greyscale images of the sample absorption coefficients were obtained with a voxel size of 9.85 × 9.85 × 9.85 μm^3. Regions Of Interests (ROIs) of size 1244 × 1244 × 304 voxels were then extracted and subjected to the image analysis procedure detailed hereafter. Figure 2.4 shows small crops (304 × 304 × 304 voxels) achieved inside the reconstructed ROIs to

qualitatively illustrate the typical 3D microstructures of four different samples with different bead diameters.

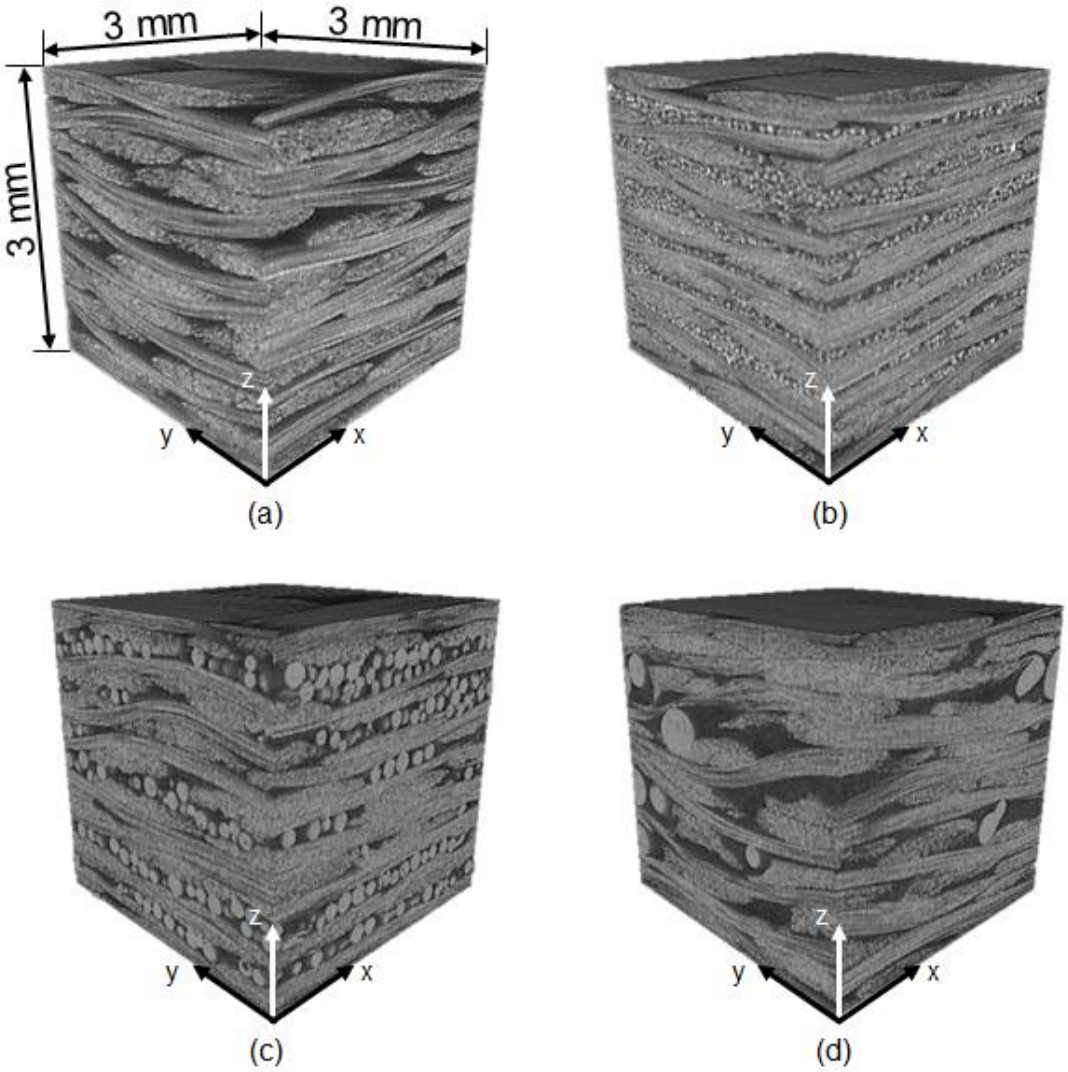

Figure 2.4 3D images (304 × 304 × 304 voxels) showing the structure of (a) a plain sample (*i.e.*, with no beads), and samples with embedded beads with diameters of (b) 40-70 μm, (c) 100-200 μm, and (d) 400-800 μm. Sample thickness, h, in z direction is the same in all samples in (a) – (d); and volume fraction of beads is $\phi_b = 10\%$ in all samples in (b) – (d).

2.2.3.2. Image analysis

In order to assess relevant microstructure descriptors from the scanned samples (see below), the 3D images were first segmented using ImageJ [88] so that the porous phase, the fibers and the beads could be extracted and analyzed independently. The segmentation of the porous phase was readily achieved using a standard thresholding operation due to its strong absorption contrast with respect to the glass fibers and beads. A procedure was used to extract beads from the remaining glass phase, as a consequence of the poor absorption contrast between beads and fibers (see Figure 2.5). Thus, in each greyscale slice along the thickness of the imaged samples, *i.e.*, along the z direction, the structure tensor was computed using the plugin FeatureJ of ImageJ [89], and beads were isolated as they exhibited a more isotropic shape than the fibrous network (see Figure 2.5(b-c)). Thereby, additional analyses were conducted:

- The bead segmentation allowed us to locate the beads. Consequently, the normalized z-distribution of the bead content was computed as $\phi_{bz}^{*} = \phi_{bz}/\phi_b$ where ϕ_b is volume fraction of beads in the entire specimen and ϕ_{bz} is the bead content in each slice parallel to xy plane (*i.e.*, fraction of the slice occupied by the beads). We also built in-plane 2D maps of the bead content ϕ_{bxy}, defined as the volume fraction of beads in the vertical column of height h and cross section area of 1 pixel located at the position (x, y). That means, ϕ_{bxy} can have a value between 0 and 100% such that $\phi_{bxy} = 100\%$ if all of the 304 slices have a bead at a pixel coordinate of (x, y).
- From the binarized image of the porous phase, it was possible to estimate the pore size distribution: (i) by using successive dilation and erosion

morphological operations with a cubic structural element; (ii) by counting the remaining voxels after these operations; and (iii) by repeating these operations for increasing sizes of the cubic element [90,91].

- We estimated the mean intercept number of the images, the chord lengths of pores in three principal directions (l_x, l_y, and l_z), their mean values ($\overline{l_x}$, $\overline{l_y}$, and $\overline{l_z}$) as well as the specific surface S of the porous structures, using the method proposed by Rolland du Roscoat *et al.* [92]. Ratio of mean chord lengths, $r_{xy} = \overline{l_x}/\overline{l_y}$, $r_{xz} = \overline{l_x}/\overline{l_z}$ and $r_{yz} = \overline{l_y}/\overline{l_z}$ were calculated to quantify the anisotropy of the pores. The specific surface S, defined as the surface area of the pore-solid interface per unit volume, is closely linked to the permeability [93]. For example, the following Kozeny equation for unidirectional porous media relates the permeability K to the radius of fibers, R [94,95]:

$$K = \frac{R^2}{4c}\frac{\phi_p^3}{\left(1-\phi_p\right)^2} \tag{2.2}$$

where c is the Kozeny constant. Considering that the porous structure is uniquely made of a network of non-overlapping cylinders of radius R and volume fraction ϕ_f, one gets $S = 2\phi_f/R$ so that:

$$K = \frac{\phi_p^3}{cS^2} \tag{2.3}$$

These equations will be further discussed in section 3.

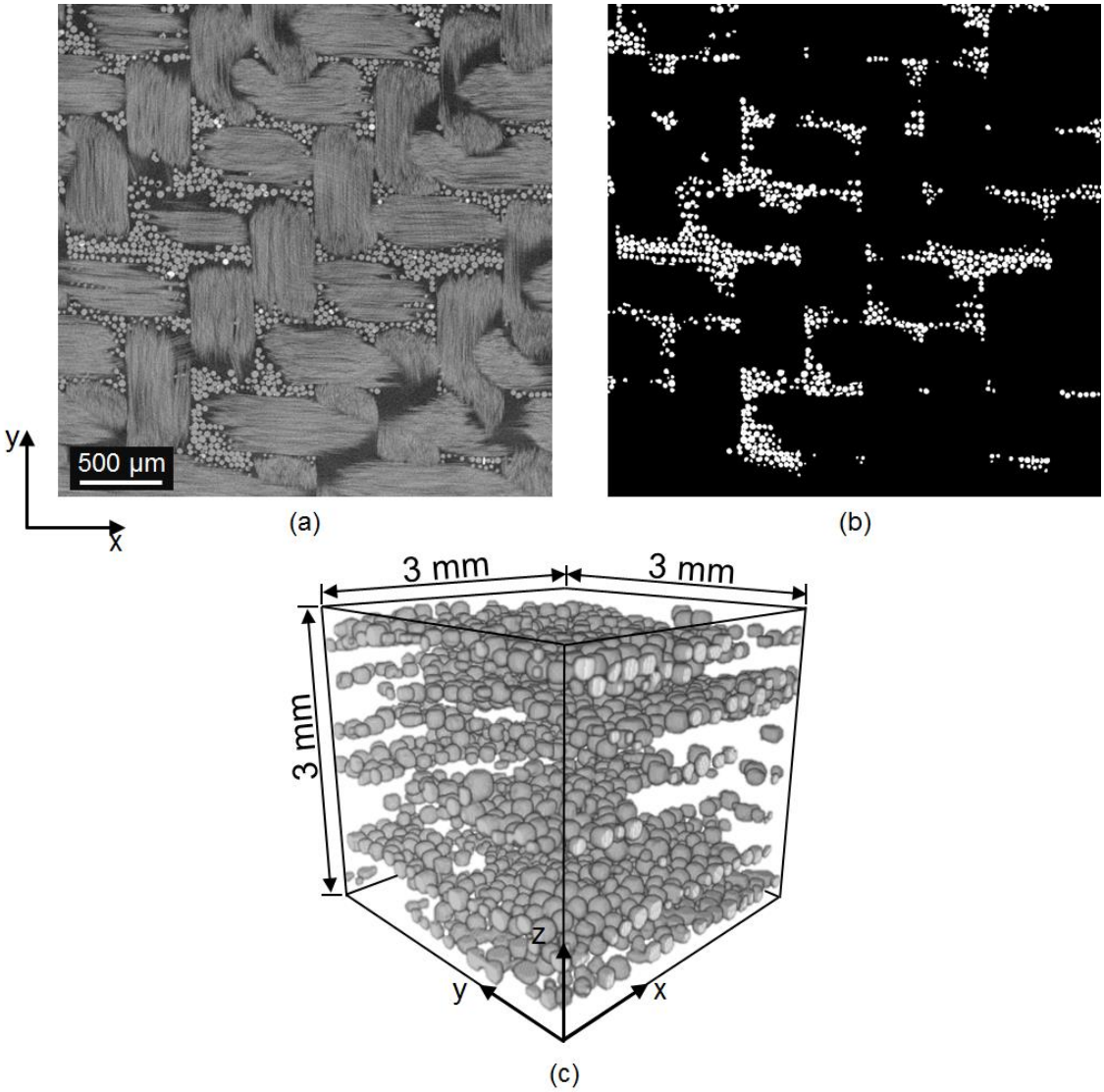

Figure 2.5 (a) Slice along thickness direction (*i.e.,* in *xy* plane) of a sample with 100-200 µm beads at ϕ_b = 10%. (b) The beads are seen as white circles after the image treatment of the same slice. (c) 3D volume (304 × 304 × 304 voxels) showing the segmented beads (see Figure 2.4(c) for 3D reconstruction of the original volume).

2.2.3.3. Numerical estimation of permeability

The permeability of the samples along the weft direction was also estimated numerically. For these estimations, fluid flow simulations were performed using the commercial Finite Volume software GeoDict [96]. Using the CFD module FlowDict and the Explicit Jump-Stokes (EJ-Stokes) solver,

localization Stokes flow problems, deduced from the homogenization method with multiple scale asymptotic expansions [97], were solved within the 3D binary volumes of the pore structures with sizes of 812 × 812 × 304 voxels; the local velocity field as well as the first order pressure fluctuation field were considered as in-plane periodic and the in-plane macroscale pressure-gradient was imposed [98,99].

2.3. Results and discussion

2.3.1. Permeability measurements

2.3.1.1. Experimental results

Experimental values of the textile in-plane permeability $K_{exp,i}$ for each tested sample i (the index $i = 1$ stands for the twill weave) are reported in Figure 2.6(a) and Figure 2.6(b) as a function of porosity and bead diameter, respectively. They have also been gathered in Table 2.1. The permeability of plain fabrics decreased with increasing ϕ_f, and thus with decreasing ϕ_p, as expected. The parameters of Eq. (2.1) were found to be $A = 5.99\times10^{-8}$ m^2 and $b = 17.2$. Figure 2.6(a) shows that increasing ϕ_b of the smallest beads category (40-70 μm), thus decreasing ϕ_p, had a similar effect on permeability as increasing ϕ_f of the plain fabric. Permeability decreased as ϕ_b increased with a similar trend of the permeability curve as for the plain samples, except for the lowest bead content where the permeability was slightly higher than that recorded for the twill weave at the same volume fraction of solid. Introducing beads with 100-200 μm diameters had a similar effect on permeability and caused an initial decrease in permeability for increasing volume fraction ϕ_b. However, when $\phi_b \geq 5.0\%$, the trend for this range of bead diameter diverged from the trend observed with the plain fabrics, the decrease of the permeability with decreasing porosity being less pronounced. Surprisingly,

for the largest beads (400-800 μm), when $\phi_b \geq$ 2.5%, the deviation from the plain fabrics data was significant and such that the permeability even increased when increasing ϕ_b, although the overall porosity decreased. In addition, data plotted in Figure 2.6(b) for ϕ_b = 5.0% shows that the permeability was in the same range for d_b < 200 μm (samples #3, #5 and #7), whereas it was significantly higher for d_b > 200 μm (samples #9, #10, and #12). These trends suggest that small beads have mainly filled the existing pores while larger ones have deformed the fabric, mainly forming new pores and/or enlarging existing ones.

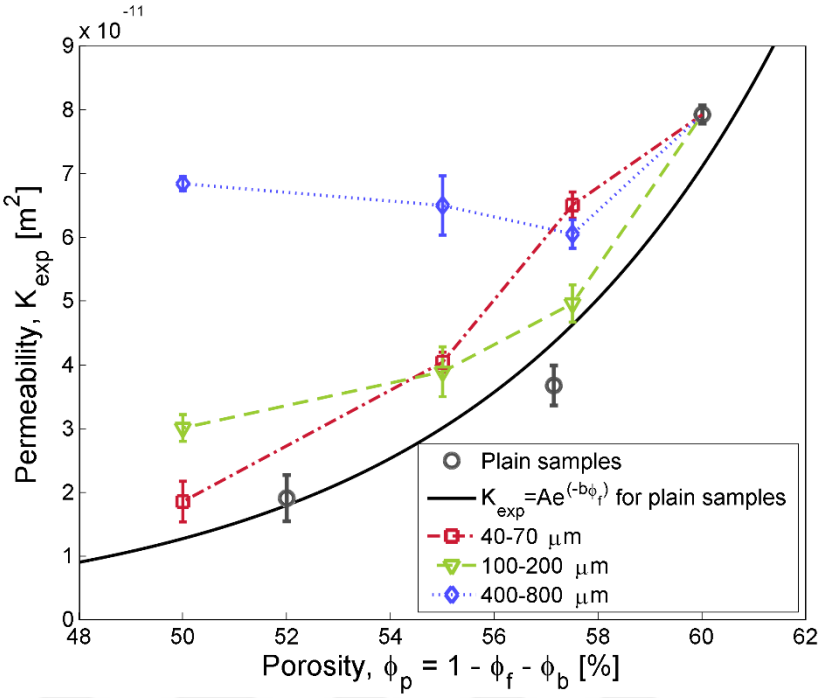

(a)

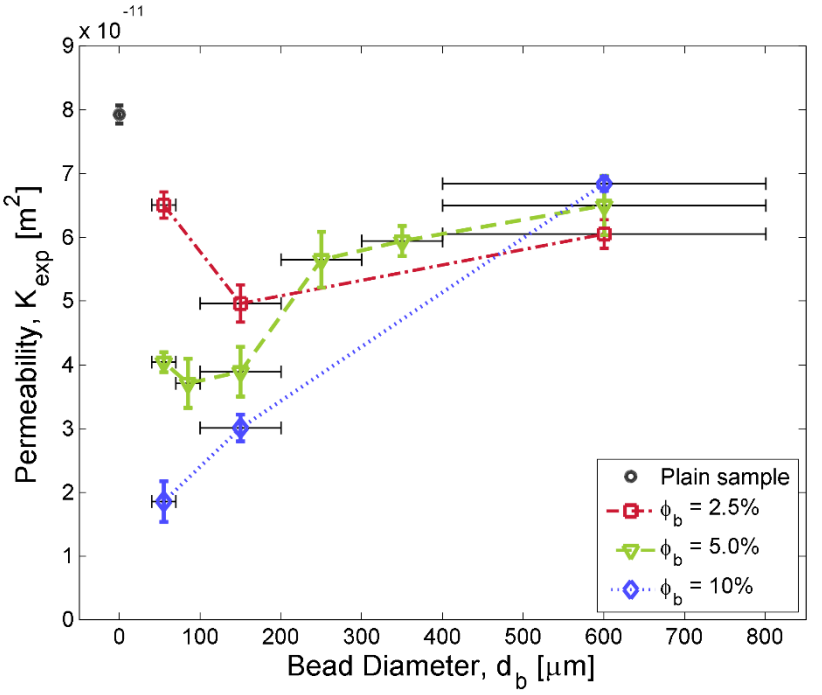

(b)

Figure 2.6 Textile permeability measured along the weft direction as a function of (a) porosity and (b) bead diameter. In (b), permeability at zero bead diameter corresponds to the permeability of the twill fabric without bead, the horizontal error bars indicate the range of particle size within one type of sample and the vertical error bars are standard deviations in three samples.

2.3.1.2. Numerical results

Table 2.1 reports numerical estimations of the permeability $K_{num,i}$ based on the acquired 3D images and pore-scale fluid-flow simulation (see subsection 2.4). As seen in Table 2.1, simulated trends were in good agreement with the experimental results from a qualitative standpoint. However, as already observed for other fibrous structures [100], numerical values were higher than experimental ones: the ratio, K_{num}/K_{exp} ranged between 1.43 and 2.31. Various factors can cause this discrepancy. The two most probable ones may be related to the spatial resolution used for scanning the samples and to the subsequent image analysis operations. Indeed, we chose a voxel size of (9.85 μm)^3 in order to have sufficiently large images with representative volumes of the textiles and beads. However, in doing so, microstructure details lower than the characteristic length of voxels (9.85 μm), such as the fiber scale surface roughness and fiber scale narrow channels in between fiber bundles or inside fiber bundles, could not be numerically captured very well, although they could contribute significantly to the fluid drag [101,102]. In addition, the filtering and smoothing operations required to delete noise and contributions from other tomography artefacts could have smoothed these microstructural features and thus to slightly overestimate the permeability. Taking into account these uncertainties, permeability results were normalized in order to provide a suitable quantitative comparison between experimental and numerical results [99,100]. Thus, the following dimensionless experimental $K^*_{exp,i} = K_{exp,i}\ /K_{exp,1}$ and numerical $K^*_{num,i} = K_{num,i}\ /K_{num,1}$ permeability was introduced. As seen in Table 2.1 and Figure 2.7, values of $K^*_{exp,i}$ and $K^*_{num,i}$ were very similar quantitatively, the numerical estimates being slightly higher: both of them captured the effects of the bead content and diameter well.

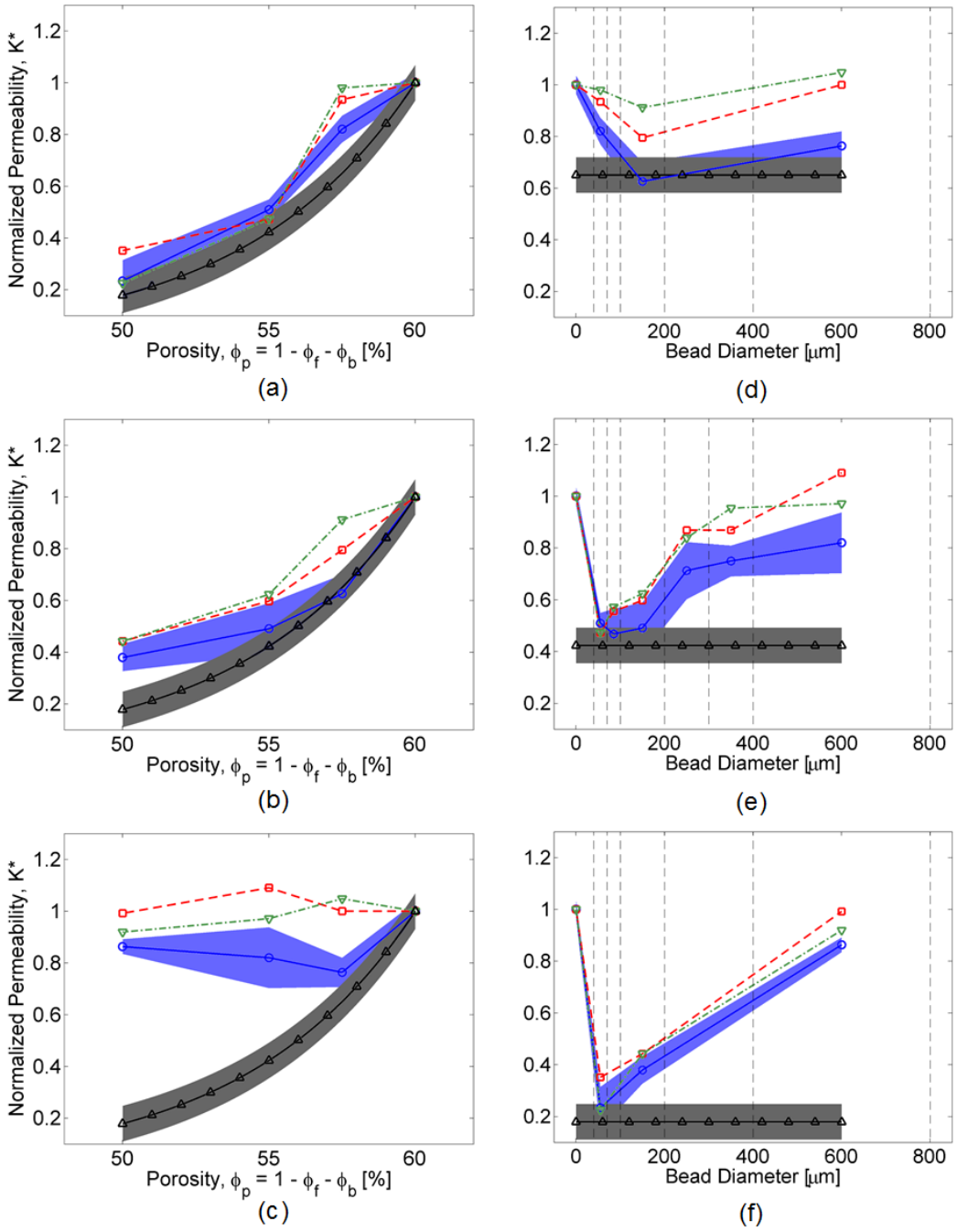

Figure 2.7 Normalized permeability as a function of ϕ_p for samples with diameter ranges of 40-70 μm (a), 100-200 μm (b), 400-800 μm (c), and as function of bead diameter for samples with ϕ_b of 2.5% (d), 5.0% (e) and 10% (e). In (a) – (c), —△— denotes the fitted curve using Eq. (2.1), normalized with respect to its value at ϕ_p = 60%. In (d) – (f), —△— denotes the value of the same curve at corresponding ϕ_p values of 57.5%, 55.0% and 50.0% respectively. In (a) – (f), data shown with symbols —○—, —□—, and ···▽··· denote experimental results, CFD results and semi-analytical permeability results, respectively. Colored clouds around experimental trends account for the experimental uncertainties.

2.3.2. Microstructures

2.3.2.1. Spatial bead distributions

Figure 2.8(a) and Figure 2.8(b) are 2D maps of the bead content ϕ_{bxy} for samples #7 and #13, respectively. Although the beads were sieved manually, a random bead distribution was achieved when large beads were used (in Figure 2.8(b)), and a quasi-periodic pattern formed when small beads accumulated into the crossing zones of warp/weft bundles (Figure 2.8(a)). These trends are confirmed in Figure 2.8(c) and Figure 2.8(d), which show the change of ϕ_{bz}^{*} along the thickness direction of sample #7 (ϕ_b = 5%, d_b= 100 – 200 μm) and sample #13 ((ϕ_b = 10%, d_b= 400 – 800 μm)), respectively. In these graphs, the mean values of ϕ_{bz}^{*} are close to 1 with corresponding ϕ_{bz} being 5.80% and 9.69% respectively, the small deviations being attributed to the fact that only a small section of a sample was analyzed (the overall volume of a sample was $(\pi(20\ mm)^2) \times 3\ mm = \ 3770\ mm^3$ while the evaluated volume was $12\ mm \times 12\ mm \times 3\ mm = \ 432\ mm^3$). In Figure 2.8(c), ϕ_{bz}^{*} varies with a smooth and quasi-periodic oscillatory distribution where seven peaks are observed. These peaks, together with the pattern observed in Figure 2.8(a), correspond to interlayer spaces within which beads tend to accumulate during the sample fabrication (see also Figure 2.4(b)). On the contrary, in accordance to what is observed in Figure 2.8(b), such a quasi-periodic distribution is not observed in Figure 2.8(d). During the fabrication of these samples, the large beads rather deformed the fibrous fabrics, mainly by consolidation but also bending fiber bundles: this is clearly illustrated in Figure 2.4(d) in the case of beads with d_b of 400-800 μm, where fiber bundles are severely bent along the z direction. It should be noted that for all the

samples with d_b smaller than 200 μm (samples #2 - #8), the distribution of ϕ_b was similar to that of sample #7 showing quasi-periodic in-plane and out-of-plane distributions. In addition, for samples with d_b larger than 200 μm (samples #9 - 13), in-plane and out-of-plane distributions were similar to that of sample #13 with a more pronounced deviation from the smooth oscillatory behavior for increasing bead diameter.

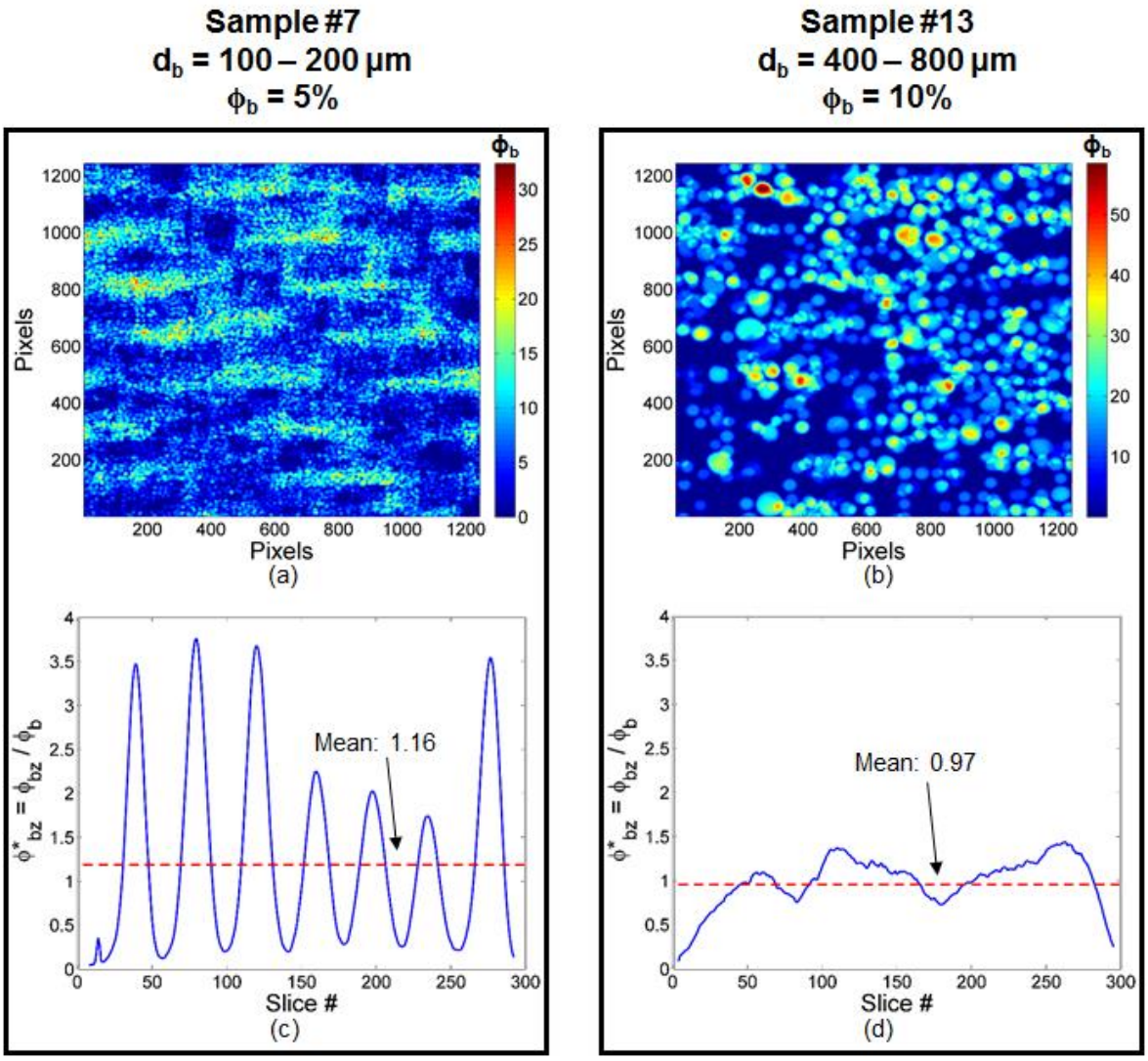

Figure 2.8 Analysis of bead distribution in slices along thickness direction, z. (a) – (b) Superposed bead distribution at pixels, ϕ_{bxy}, (c) – (d) variation of ϕ^*_{bz} within 304 slices along z direction of samples #7 and #13, respectively. Dashed lines in (c) and (d) correspond to the mean ϕ_b values of 5.80% and 9.69%, respectively.

2.3.2.2. Pore size distributions

Resulting cumulative pore size distributions for three different d_b ranges (40-70, 100-200, and 400-800 μm) are plotted as a function of pore size in Figure 2.9(a-c) (colored curves) along with the pore size distribution of the plain sample (black curve). Figure 2.9(a) reveals that the cumulative frequency increased faster with increasing ϕ_b values so that corresponding curves were skewed towards the left. Though the effect was not very clear for the smallest ϕ_b value of 2.5%, for larger ϕ_b values it is obvious from this graph that large pores present in the plain samples were progressively filled with increasing ϕ_b. In Figure 2.9(b), a similar trend is observed for samples containing beads with a larger diameter range of 100-200 μm. In Figure 2.9(c), the opposite trend is observed so that cumulative pore size distribution were skewed towards right with increasing ϕ_b, due to formation of new and larger pores when the embedded beads have d_b = 400-800 μm (see previous subsection).

To better understand the effect of bead diameter on pore size distribution, Figure 2.9(d-f) shows the pore size distribution for the samples with beads at a fixed ϕ_b of 2.5%, 5.0%, and 10%, respectively, along with the pore-size distribution of the plain sample. The pore-size distribution of the samples with ϕ_b of 5.0% in Figure 2.9(e) verifies that sample #9 had a similar pore-size distribution as the plain sample (#1), indicating that the embedded beads with $d_b = d_{b,critical}$ = 200-300 μm did not alter the pore-size distribution whereas beads with $d_b < d_{b,critical}$ and $d_b > d_{b,critical}$ altered the distribution with opposite effects. In other words, at $\phi_b = 5.0\%$, this implies that samples with a bead diameter smaller than 200 μm (samples #3, #5, and #7) had pore size distributions that skewed curves towards left and this effect

was more pronounced as the bead diameter decreased. In addition, the opposite is true for samples with bead diameter larger than 300 μm (samples #10, and #12) where larger pores were formed by the consolidation and the bending of fiber bundles. Even though only three different diameter-ranges were studied for ϕ_b of 2.5% and 10%, similar behavior in pore-size distributions was observed, *i.e.*, beads with diameter smaller than 200 μm filled the existing pores whereas beads with diameter larger than 300 μm formed larger pores as seen qualitatively in the 3D reconstructions in Figure 2.4(b-d).

The change in dimensionless permeability reported in Figure 2.7(d-f) directly related to the aforementioned results. Indeed, at fixed porosity, the permeability is highly affected by the pore space, which is in turn affected by the dimensions of solid (fiber and beads) making the porous medium [103–105]: increasing the particle diameter, or more generally shifting the particle size distribution towards larger characteristic lengths usually leads to an increase of the permeability. As shown in Figure 2.7(d-f), this is in accordance with the results, except for samples with $\phi_b = 2.5\%$ and 5% of the smallest beads. Presumably, particle locations for these samples may have differed from those observed for other beads contents or sizes.

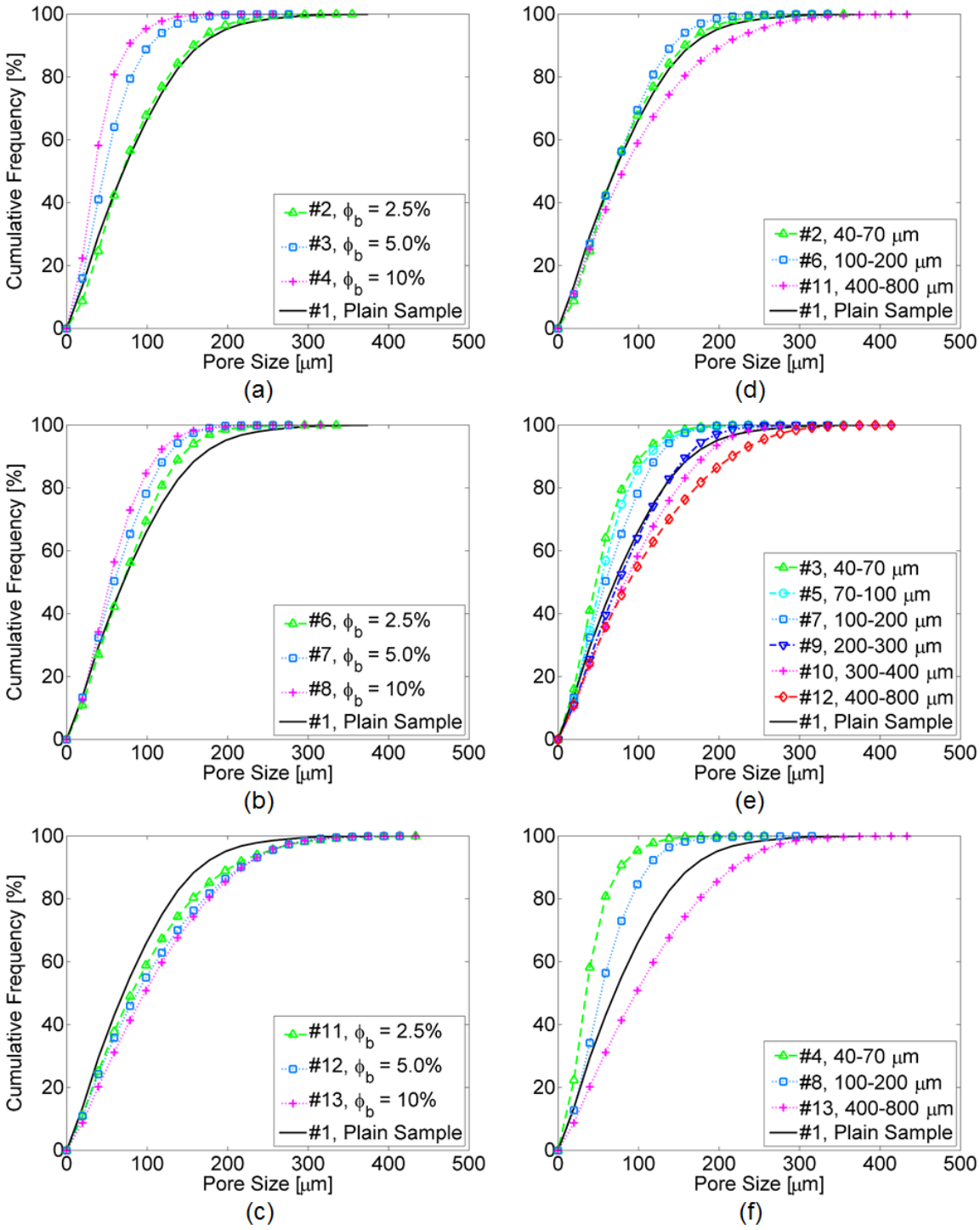

Figure 2.9 Cumulative pore size distribution of samples with embedded beads which have a diameter range, d_b, of 40-70 μm (a), 100-200 μm (b), 400-800 μm (c); and a fixed bead-volume-fraction, ϕ_b, of 2.5% (d), 5.0% (e) and 10% (f). Pore size distribution of twill sample alone (ϕ_b= 0) is included in plots for the purpose of comparison

2.3.2.3. Pore shape anisotropy

Anisotropy ratios of the mean-pore chord-lengths were calculated, $r_{xy} = \overline{l_x}/\overline{l_y}$, $r_{xz} = \overline{l_x}/\overline{l_z}$ and $r_{yz} = \overline{l_y}/\overline{l_z}$ and plotted as a function of ϕ_b of samples with d_b = 100-200 μm in Figure 2.10(a) and plotted as a function of d_b of samples with ϕ_b = 5.0% in Figure 2.10(b). Both figures indicate that the pores exhibited flat shapes. The in-plane anisotropy (r_{xy}) of the twill sample without bead, due to inherent difference between the warp and weft directions of the fabric, was reduced by introduction of the beads. In Figure 2.10(a), increasing ϕ_b resulted in a transition towards more isotropic pores, highlighted by the significant decreases in r_{xz} and r_{yz}. Similar trends were observed among the samples with d_b = 40-70 μm and d_b = 400-800 μm, which were not plotted here for the sake of brevity. In Figure 2.10(b), no clear dependency of anisotropy was observed on d_b, yet all the samples were less anisotropic than the plain sample and same behavior is observed among the samples with ϕ_b = 2.5% and 10%, again not plotted for the sake of brevity.

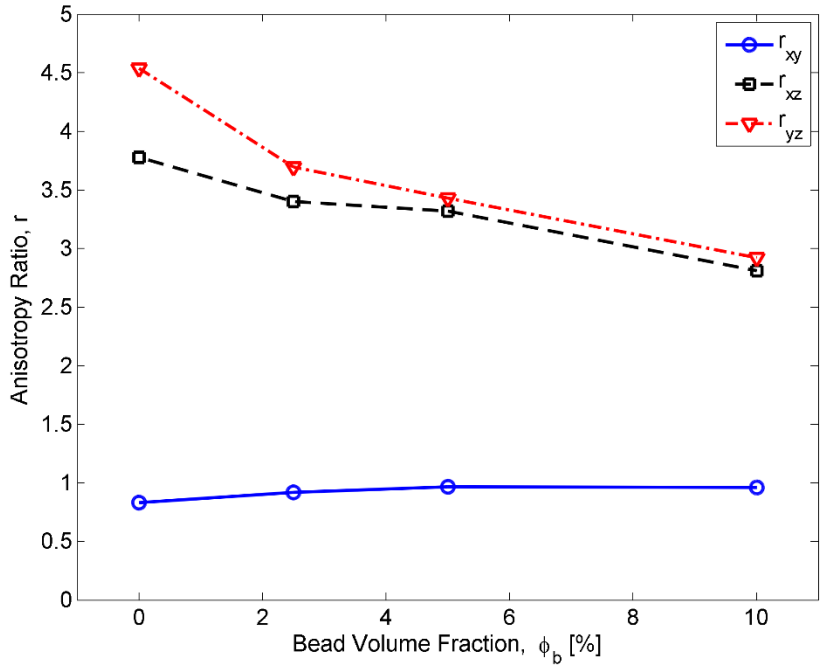

(a)

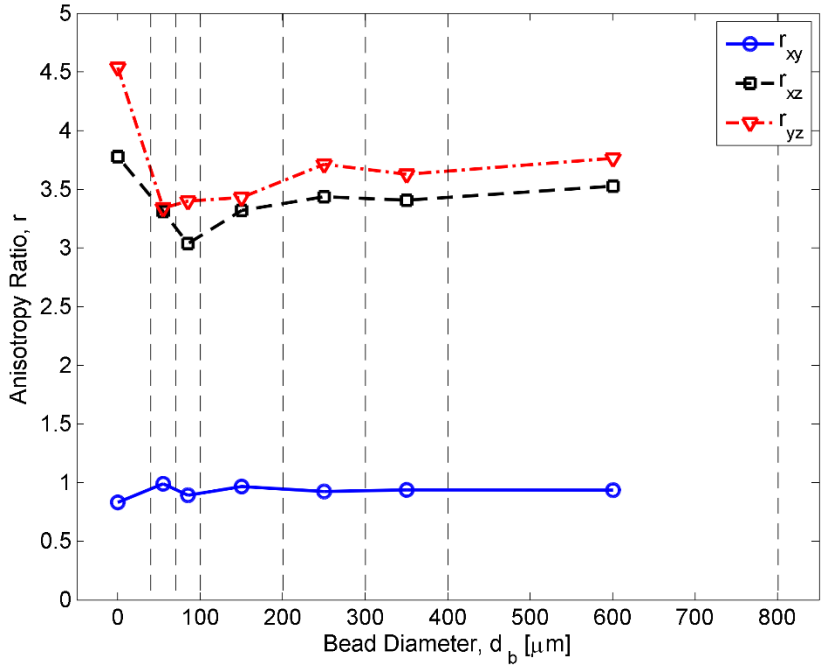

(b)

Figure 2.10 Anisotropy ratio as a function of bead volume fraction ϕ_b for samples with bead-diameter range of 100-200 μm (a), as a function of bead diameter d_b for samples with bead-volume-fraction of 5.0% (b). In (a), ϕ_b= 0 corresponds to the twill sample alone. In (b), d_b= 0 of d_b of samples with ϕ_b of 5.0% in (b). In (a), and the vertical dashed lines correspond to the lower and upper bounds for each diameter range.

2.3.2.4. Specific surface and semi-analytical estimation of permeability

Values of the computed specific surface, S, are listed in Table 2.1. Recall that these values were obtained with a voxel size of (9.85 μm)^3, *i.e.*, with a characteristic length close to the fiber radius (9 μm): they can be considered as mesoscale values, well suited for fiber bundles and beads only. For the sample without bead (#13), following the $S = 2\phi_f/R$ relationship, R was evaluated from the measured surface area and was on the order of hundred microns, which is comparable to the geometric mean of the semi-minor and semi-major axes of ideally elliptical fiber bundles. By embedding beads into a fabric preform, values reported in Table 2.1 prove that the specific surface S of the overall media (fabric preform and beads) exhibited complex trends due to various competing mechanisms:

- At a fixed bead diameter, (i) increasing the bead content was prone to increase S. However, at the same time, this could induce (ii) the consolidation of the fiber bundle and thus a decrease of the mesoscale specific surface. As shown in Table 2.1, mechanism (i) ruled the structure of the assemblies at low bead diameters, whereas mechanism (ii) was predominant at higher bead diameters: for samples with bead diameter higher than 100-200 μm, the resulting specific surfaces were even lower than those recorded for the twill weave alone.
- At a fixed volume-fraction of solids, (iii) decreasing the bead diameter was also prone to increase the mesoscale specific surface, provided that subsequent consolidation mechanisms of the fiber bundles were restrained. Table 2.1 verifies that mechanism (iii) governed the mesostructures of the assemblies for the two highest investigated bead

contents. For the lowest investigated bead content, mechanism (iii) seemed to be important above bead diameters of 100-200 μm. Below this diameter range, mechanism (ii) might be predominant.

Lastly, dimensionless semi-analytical permeability values based on S measurements, $K^*_{S,i} = K_{S,i} / K_{S,1}$, were calculated using Eq. (2.3) as follows

$$K^*_{S,i} = \frac{S_1^2 \, \phi_i^3}{S_i^2 \, \phi_1^3} \tag{2.4}$$

under the assumption that Kozeny constant, c, was equal for all configurations. These estimates are reported in Figure 2.7 and Table 2.1. As obvious from this figure and this table, $K^*_{S,i}$ follow rather closely the trends given both by the experiments ($K^*_{exp,i}$) and the pore scale CFD simulations ($K^*_{num,i}$) and the correlation between $K^*_{S,i}$ and $K^*_{num,i}$ is better as analytical and numerical estimates were obtained from the same volumes. Thus, these results indicate that from a "simple" analytical model and the knowledge of the specific surface of the samples, pretty good semi-analytical estimate of $K^*_{S,i}$ can be obtained, emphasizing the well-known leading roles of the porosity ϕ_b and the specific surface S on the permeability.

2.3.2.5. Pore chord length and bead diameter relationship

As reported in Figure 2.6 and Figure 2.7 for ϕ_b = 5.0 and 10%, a change in permeability regime occurred at critical bead diameters d_b of ≈ 100-200, and 40-70 μm, respectively. Above these critical values, the specimens' permeability was higher than that of the twill weave alone at the same volume fraction of solid. This transition was attributed to the extensive deformation of fabric (consolidation and distortion) as large beads were introduced. Though a similar transition was observed for the pore-size distribution (see Figure 2.9(d)) and bead distribution along the thickness

direction (see Figure 2.8(c) and Figure 2.8(d)), it deserves further attention to disclose the characteristics of the studied fabric.

An analysis on the smallest chord length of the twill weave without bead, *i.e.*, the out-of-plane pore chord length l_z, showed that (i) the porosity exhibited a strong out-of-plane anisotropy (Figure 2.10) and (ii) adding beads into the twill weave mainly resulted in yarns distortion along z direction (see Figure 2.4(c), Figure 2.4(d)). The continuous line in Figure 2.11 plots the dependence of the cumulative porosity ϕ_{pz} on the out-of-plane chord length l_z. Due to the voxel size used to image the sample (9.85 μm)^3, ϕ_{pz} goes from 0 to $\phi_{pz,max} = 35\%$, this value being obviously lower than the overall porosity of the twill weave (60%). However, this difference does not affect the relationship between the pore-size distribution of the mesostructures and the bead diameters, since the smallest of the studied beads has a diameter range of 40-70 μm, which is significantly larger than the voxel size. Thus, for a given value $l_{z,i}$, the corresponding porosity value $\phi_{pz,i}(l_{z,i})$ represents the volume fraction of pores with chord lengths equal to or smaller than $l_{z,i}$. This also means that chords larger than $l_{z,i}$ occupy a porosity of $\phi_{pz,max} - \phi_{pz,i}(l_{z,i})$. Therefore, bearing in mind that pores are highly anisotropic (see Figure 2.10), it is reasonable to imagine two possible scenarios when beads with a diameter d_b close to $l_{z,i}$ are added into the twill weave:

(a) They first fill the empty space of porosity $\phi_{pz,max} - \phi_{pz,i}(l_{z,i})$, without causing significant consolidation or bending of fiber bundles (see Figure 2.4(b)). This would be possible as long as the volume content of beads in these pores remains below a critical bead content which we can here approximate, as a first approach, as the maximal random close packing fraction for spherical particles $\phi_{lp} \approx 0.64$ [106].

(b) Above such a bead content, a consolidation of fiber bundles and/or an out-of-plane bending of fiber bundles takes place; the prevalence of one of the two aforementioned mechanisms may occur as follows:

   i. The lower the bead diameter, the higher the bead content to reach regime (b) and the higher the consolidation of the twill weave, as illustrated in the example shown in Figure 2.4(c).

   ii. Conversely, the higher the bead diameter, the lower the bead content to reach regime (b), and the higher the distortion of the fabrics that result in significant pore opening (Figure 2.4(c), Figure 2.4(d)).

Figure 2.11 reports the values of $d_b, \phi_b/\phi_{lp}$ used in the tested samples, in order to emphasize whether scenarios (a) or (b) (*i.e.*, the points below or above the black curve, respectively) were prone to occur. In addition, the green rectangular points in Figure 2.7 indicate that the experimental dimensionless permeability K^*_{exp} of the samples was close to the permeability of the consolidated twill weave without bead, $K^*_{plain}(\phi_f + \phi_b)$. Similarly, red circular points indicate samples whose experimental dimensionless permeability K^*_{exp} was higher than $K^*_{plain}(\phi_f + \phi_b)$. Figure 2.11 clearly proves that all samples located above the continuous black curve, *i.e.*, those corresponding to the bead-filling scenario (b), exhibited a higher permeability than the twill weave at the same porosity. In addition, as illustrated in Figure 2.4(c) and Figure 2.4(d), these samples all exhibited pronounced bundle bending, *i.e.*, following filling mechanisms (b-ii) with pore opening. Consequently, the prevalence of bundle distortion during the filling of the twill weave with adequately big beads induced pore opening and limited the increase of, or even decreased, the sample specific surface. Thus, in spite of the overall decrease of the sample porosity, the decrease in

sample permeability was less pronounced than the twill weave alone, or even increased (see Eq. (2.4)).

In addition, as emphasized in Figure 2.11, data located below the continuous black curve correspond to filling scenario (a). It is interesting to notice that at given volume fraction of pores, the permeability of most of them is rather close to the fabric without bead (see also Figure 2.7). For these situations, filling mechanisms thus resulted in specific-surface changes similar to that encountered during the compaction of the twill weave alone. This general trend is however not fulfilled by the sample at the lowest bead content and diameter; as mentioned previously, the bead placement of this sample might have differed from the other samples during filling.

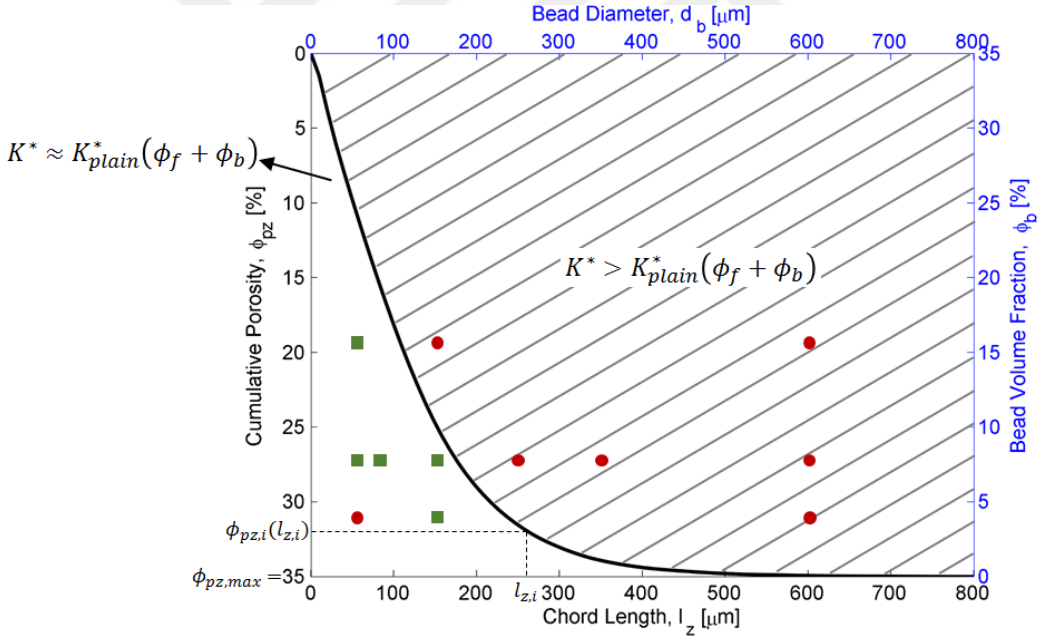

Figure 2.11 The black continuous curve represents the cumulated porosity of the twill sample without bead as a function of chord length in z direction l_z, dividing the domain into two regions: in one region $K \approx K_{plain}(\phi_f + \phi_b)$; and in the other region $K > K_{plain}(\phi_f + \phi_b)$. ■ and ● denote the experimentally studied bead diameter and volume fraction combinations, the former classifies the combinations respecting the $K \approx K_{plain}(\phi_f + \phi_b)$ behavior and the latter classifies the rest.

2.4. Summary

This study investigated the influence of spherical inclusions on textile permeability. For that purpose, we carried out a systematic analysis using a glass twill weave and glass beads with various diameter ranges (40-70, 70-100, 100-200, 200-300, 300-400, and 400-800 μm) and volumetric concentrations (2.5, 5.0 and 10%). The analysis was carried out by combining 3D imaging of the fabric mesostructures (using X-ray microtomography) together with experimental and numerical estimations of fabric in-plane permeability (using a permeability setup and pore scale CFD simulations, respectively). Experimental and numerical results were in good agreement and indicated that the dimensionless permeability was a complex function of the bead content and diameter. For low bead contents and diameters, a permeability decrease was observed with introduction of beads, which mostly followed the trend of the twill weave alone at the same porosity. At a sufficiently large bead diameter, a reversion of this trend was observed.

To better understand these observations, various useful results were obtained from the 3D analysis of the sample mesostructures. It was first shown that during the sample preparation, small beads were accumulated in the meeting zones of warp/weft bundles, thus filling larger mesopores and, at higher bead contents, consolidating the fiber bundles. Conversely, larger beads were randomly distributed and could deform the fiber bundles significantly via consolidation but also via out-of-plane bending and distortion of fiber bundles. Pore-size distributions as well as specific-surface estimations were in agreement with experimental and numerical permeability estimations, showing that the in-plane permeability was influenced by the presence of two competing mechanisms, namely pore filling (mostly in the case of small beads) and new pore formation and/or pore

opening due to fabric distortion (mostly in the case of large beads). In addition, we showed that from the knowledge of the sample porosity and specific surface, together with a Kozeny-like permeability approach, it was possible to give relevant semi-analytical estimates of the dimensionless in-plane permeabilities of the filled fabrics. This could be used for guidelines if one lacks access to experimental or numerical facilities.

Analysis of pore mean chord length inside the 3D images of the samples also showed that both in the absence and in the presence of beads, pore shapes were strongly anisotropic and exhibited flat shapes. The anisotropy was reduced by introduction of the beads, in comparison to the twill sample, especially the anisotropy between in-plane directions. The mean chord length along the thickness direction remained significantly lower than the in-plane ones. In addition, critical couples (d_b, ϕ_b) were emphasized. Below these couples, beads mainly fill the fabric without pronounced modification of its mesostructure. Under such circumstances, both the sample specific surface and permeability follow trends of the compacted fabric alone. Above these couples, beads induce consolidation and high distortion of the fiber bundles (mainly out-of-plane bending), pore opening, modification of the specific surface towards slight increase or even decrease with respect to what could be expected with the compacted fabric, and thus higher permeability. We also showed that critical couples (d_b, ϕ_b) were closely correlated to the distribution of pore chord lengths of the twill weave alone along its thickness. Thus, a simple analysis of the plain fabric mesostructure would be enough to reach first estimates of the influence of inclusions on permeability.

3. MONITORING AND SIMULATION OF PART THICKNESS IN VACUUM INFUSION PROCESS

3.1. Introduction

The aim of this part are twofold. First aim in this part is to integrate a full field thickness monitoring system to a lab scale experimental VI setup containing pressure sensors, pressure controllers and DAQ unit and conduct 1D and 2D flow experiments to monitor the evolution of full field thickness profile and resin pressure. Second aim is to develop a simulation tool capable of simulating the filling and post-filling stages of VI, using incremental evolutions of pressure and flow front through a mesh-free refinement technique. By achieving these objectives, this study aims to contribute to the research in the field by combining experimental and numerical efforts to couple resin flow and thickness variation during the filling and post-filling stages of Vacuum Infusion.

3.2. Experimental setup

Figure 3.1 shows the experimental setup used in this study. Resin, driven by the pressure differential due to the applied vacuum by the vacuum pump, is infused into the part and then carried to a resin trap. Vacuum level is adjusted by an electronic vacuum regulator, SMC ITV2090, which is controlled via a computer. To record the evolution of resin pressure, 10

piezoelectric sensors (Microsensor MPM280, 0-100 kPa range with ±0.3 kPa accuracy) are located on the mold as shown in Figure 3.2(a) and Figure 3.2(b). To track the amount of resin entering the mold, the resin pot is placed on a scale (King EC-312, 0.1 g resolution). For recording the evolution of thickness, a Structured Light Scanning system is used and its details are given in the following section.

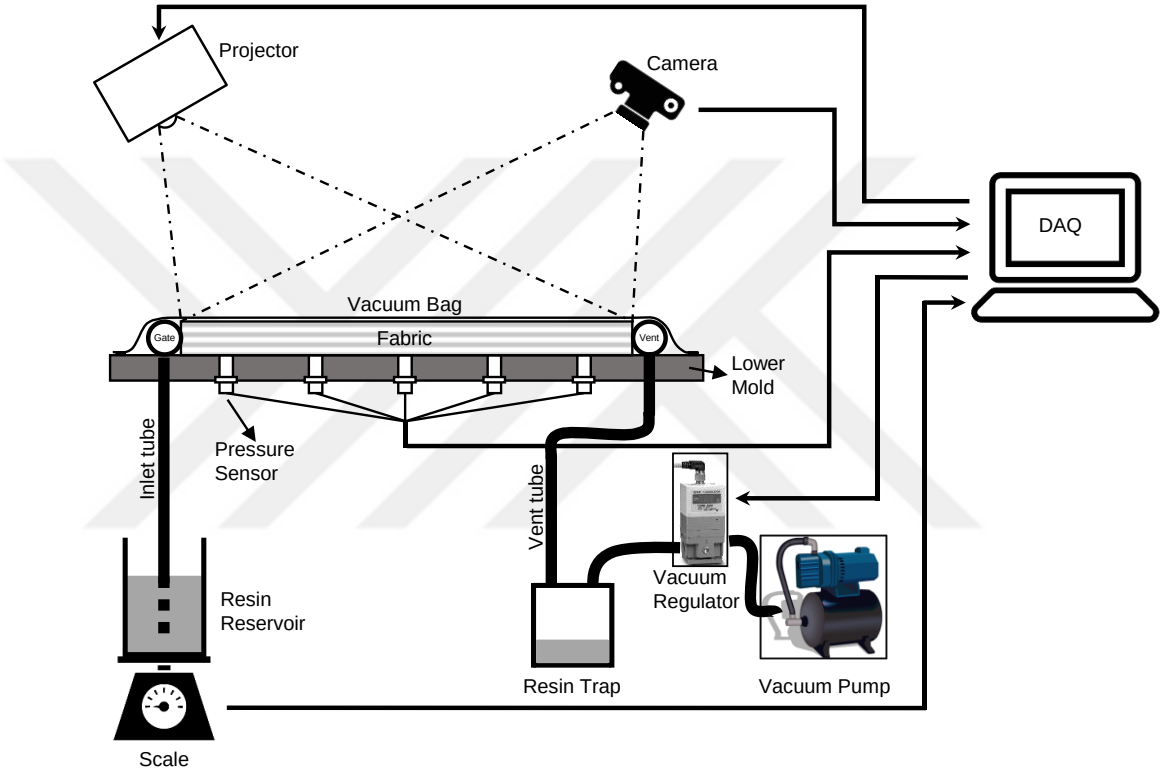

Figure 3.1 Experimental setup.

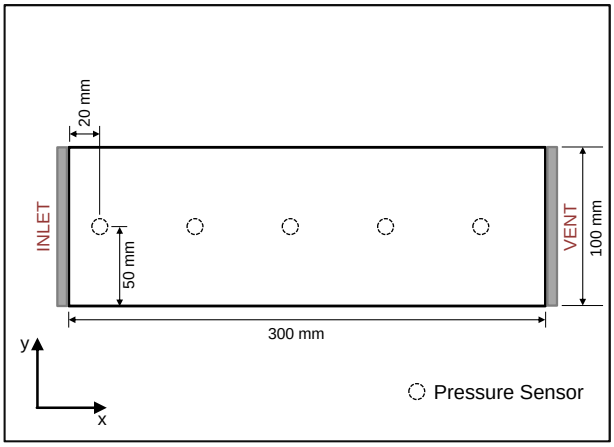

(a)

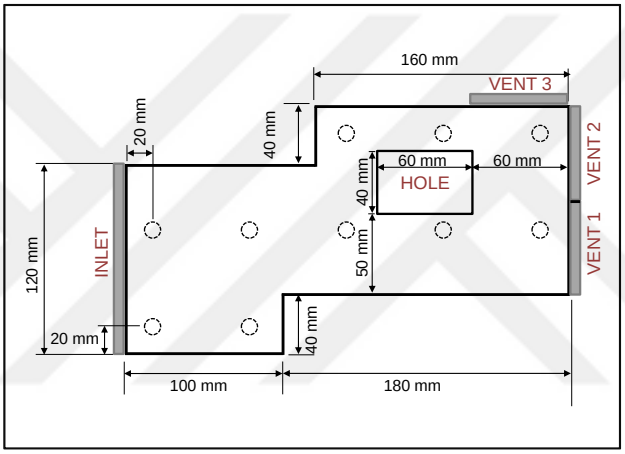

(b)

Figure 3.2 Configuration of inlet, vent and locations of pressure sensors in (a) 1D flow experiment and (b) 2D flow experiment. The distance between sensors is 60 mm in both x and y directions.

3.2.1. Structured Light Scanning (SLS)

Structured Light Scanning (SLS) is an optical metrology method allowing the full field monitoring of the thickness of an object (a composite part in this study) with respect to a reference plane. In this method, thickness of an object visible to a projector and a camera is calculated by relating the amount of phase shift to in-plane position in both absence and presence of the object. Temporal phase-shifting and spatial phase-shifting are the two

methods used for extracting the thickness profile of a geometry using projected fringe patterns [87]. Temporal phase shifting offers lower computational complexity and higher spatial resolution in the absence of high thickness gradients (which is the case in typical VI applications with a constant number of layers throughout the part). Wang et al. [107] demonstrated the suitability of spatial phase-shifting for measuring the thickness at five points along the flow direction in VI in a 1D flow case. In this study, we will exploit temporal phase-shifting in order to measure the full field thickness distribution in VI in both 1D and 2D flow cases.

Three-step phase-shifting algorithm [108] is one of the temporal phase-shifting algorithms, based on reflecting three sinusoidal fringe patterns on the surface using a projector and capturing the corresponding images using a camera. Phase of each reflected sinusoidal fringe pattern is shifted 120^{o} from the previous pattern and in turn camera captures three images with pixel intensities (I_1, I_2, I_3) that can be expressed by the following as detailed in [109–111]:

$$I_1(x,y) = I'(x,y) + I''(x,y)\cos[\phi(x,y) - 120^{o}] \tag{3.1}$$

$$I_2(x,y) = I'(x,y) + I''(x,y)\cos[\phi(x,y)] \tag{3.2}$$

$$I_3(x,y) = I'(x,y) + I''(x,y)\cos[\phi(x,y) + 120^{o}] \tag{3.3}$$

where $I'(x,y)$ is the average intensity, $I''(x,y)$ is the amplitude of the sine wave shaped intensity and $\phi(x,y)$ is the phase of each pixel. Here, $I'(x,y)$ and $\phi(x,y)$ can be calculated as

$$I'(x,y) = \frac{I_1 + I_2 + I_3}{3} \tag{3.4}$$

$$\phi(x,y) = \tan^{-1}\left(\frac{\sqrt{3}(I_1 - I_3)}{2I_2 - I_1 - I_3}\right) \tag{3.5}$$

A phase unwrapping algorithm is then used for removing the discontinuities and obtaining the continuous phase [112]. Due to the similarity between triangles $C_1C_2P_1$ and $P_3P_2P_1$ as noted in [113], height of a point P_1 in Figure 3.3 with respect to the reference plane, with a phase $\phi^{ref}(x, y)$, is

$$h_{P_1} = \frac{|P_2P_3|l}{d + |P_2P_3|} \tag{3.6}$$

where $|P_2P_3|$ is the distance between points P_2 and P_3. Considering that $d \gg |P_2P_3|$, Eq. (3.6) becomes

$$h_{P_1} = \frac{|P_2P_3|l}{d} = c_0\Delta\phi(x, y) \tag{3.7}$$

where $\Delta\phi(x, y) = \phi(x, y) - \phi^{ref}(x, y)$ and c_0 is a function of l and d and it is determined by a calibration procedure [113].

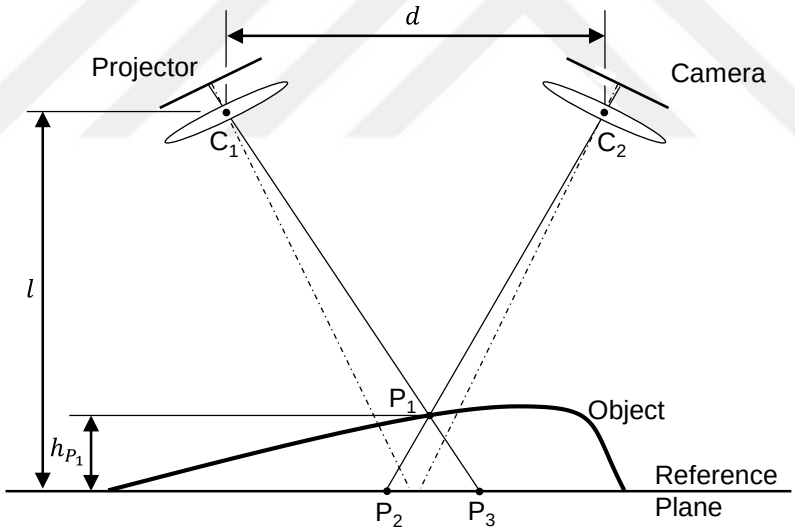

Figure 3.3 Schematic showing the phase-height relationship [113], see Eq. (3.6) for estimation of h_{P_1}.

To ensure the accuracy of the system during the calibration and the measurements, the system is isolated from any external vibration source and a constant level of illumination is attained by minimizing the ambient illumination during the experiments. In order to verify the suitability of SLS system, two types of measurements are conducted, namely static and

dynamic measurements. In both types of measurements, the camera and the projector are focused at a height of 3.5 mm from the reference surface and are calibrated. Results for static measurements are presented in Table 3.1 and they indicate that the maximum deviation from the actual thickness is 0.08 mm in the studied range which is between 2.87 mm and 7.18 mm. However, it should be noted that system is more accurate when the height of the measured is surface is close to the focal distances of camera and projector (approximately 3.5 mm above the reference surface in this case). To ensure the accuracy during the filling experiments, the camera and the projector were focused on the sample surface. The deviation between the caliper measurements and the measurements with SLS system increases slightly as the thickness increases since the measured surface starts becoming out-of-focus.

Table 3.1 Comparison of thickness measurement with caliper and proposed method when camera and projector are focused at approximately 3.5 mm from the reference surface

Caliper Measurements [mm]	Scanner Measurements [mm]
2.87	2.84±0.03
3.59	3.59±0.03
5.03	5.05±0.04
6.46	6.54±0.05
7.18	7.26±0.07

Our previous compaction characterization studies, on the fabric architectures to be used in this study, yielded that the most rapid thickness change occurs in the compaction stage (mimicking the dry loading of the fabric in Vacuum Infusion) where compaction pressure is ramped from its lowest value (1 or 5 kPa) to highest value (100 kPa) with constant pressure

change rate [75,76,114,115]. Thickness change in the compaction stage was observed to be on the order of a few millimeters while the compaction stage's duration was on the order of ten seconds, resulting in a thickness change rate smaller than 1 mm/s. To verify that SLS system is capable of capturing the thickness accurately in the presence of time-dependent changes in thickness, a set of dynamic measurements are conducted by moving a platform away from the reference plane with three different velocities, 2.1, 4.2, and 6.3 mm/s; and recording its height with respect to the reference plane. As seen in Figure 3.4, measured thickness values match the real thickness, even for the 6.3 mm/s case which is much higher than the maximum thickness change rate for the fabric architectures used in this study. As in the static measurements, deviation from the actual thickness increases as the surface moves away from the focal distance. In addition, standard deviation increases as the speed of the platform increases, indicating a dependency of the quality of the image on the rate of thickness change.

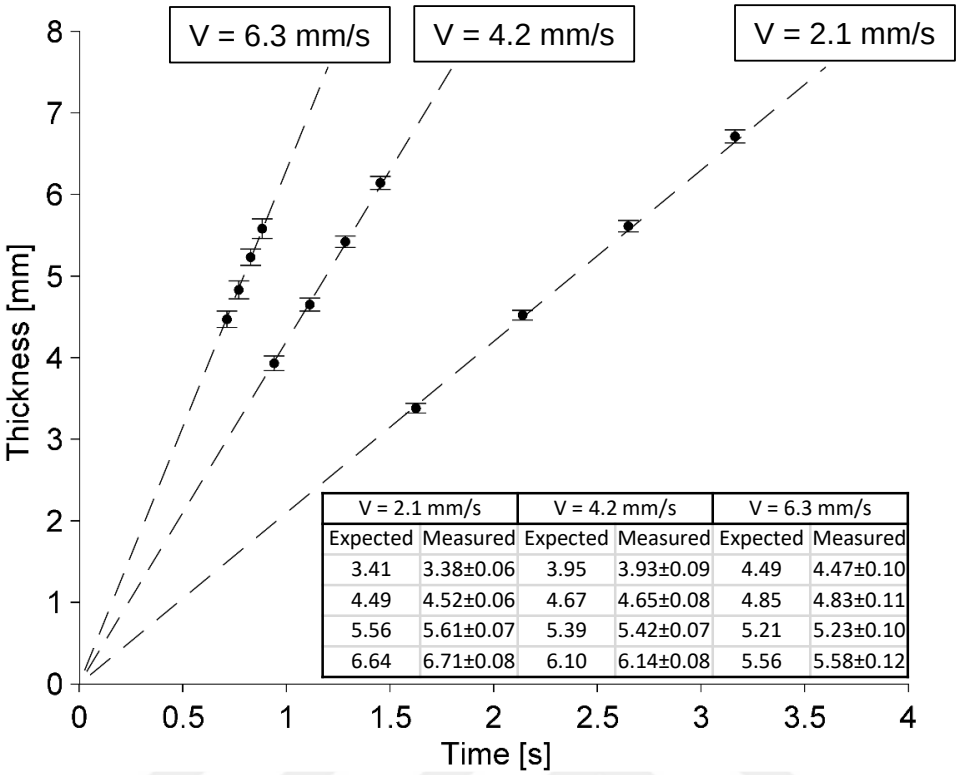

V = 2.1 mm/s		V = 4.2 mm/s		V = 6.3 mm/s	
Expected	Measured	Expected	Measured	Expected	Measured
3.41	3.38±0.06	3.95	3.93±0.09	4.49	4.47±0.10
4.49	4.52±0.06	4.67	4.65±0.08	4.85	4.83±0.11
5.56	5.61±0.07	5.39	5.42±0.07	5.21	5.23±0.10
6.64	6.71±0.08	6.10	6.14±0.08	5.56	5.58±0.12

Figure 3.4 Dynamic measurements at three different speeds, $V = 2.1$, 4.2, and 6.3 mm/s. Dashed lines represent the movement of the platform away from the reference plane with constant speed. All values in the table are in millimeters, and the values denoted as "expected" correspond to the distance of the platform from the reference plane at the half-point of each scan.

3.3. Materials and experimental methods

In this study, two different cases are studied through experiments and simulations of filling and post-filling stages. Case A corresponds to a rectilinear (1D) filling experiment and Case B corresponds to a 2D filling experiment. In these experiments, evolutions of pressure and thickness are recorded and compared with the results of the simulations conducted for the same experimental parameters and material properties. Properties of the fabrics and resin used in Case A and Case B are given in Table 3.2 and photographs of single layers of fabrics along with their corresponding thickness profiles under applied vacuum of 80 kPa are shown in Figure 3.5.

Table 3.2 Material properties

Resin		Diluted Corn Syrup
	Viscosity [Pa.s]	0.180
Random Fabric (Fibroteks)	Superficial density per layer [g/m^2], ρ_{sup}	450
	Number of layers, n	8
Biaxial Fabric (Metyx)	Superficial density per layer [g/m^2], ρ_{sup}	850
	Number of layers, n	8
Bulk density of glass fibers [kg/m^3], ρ_{bulk}		2540

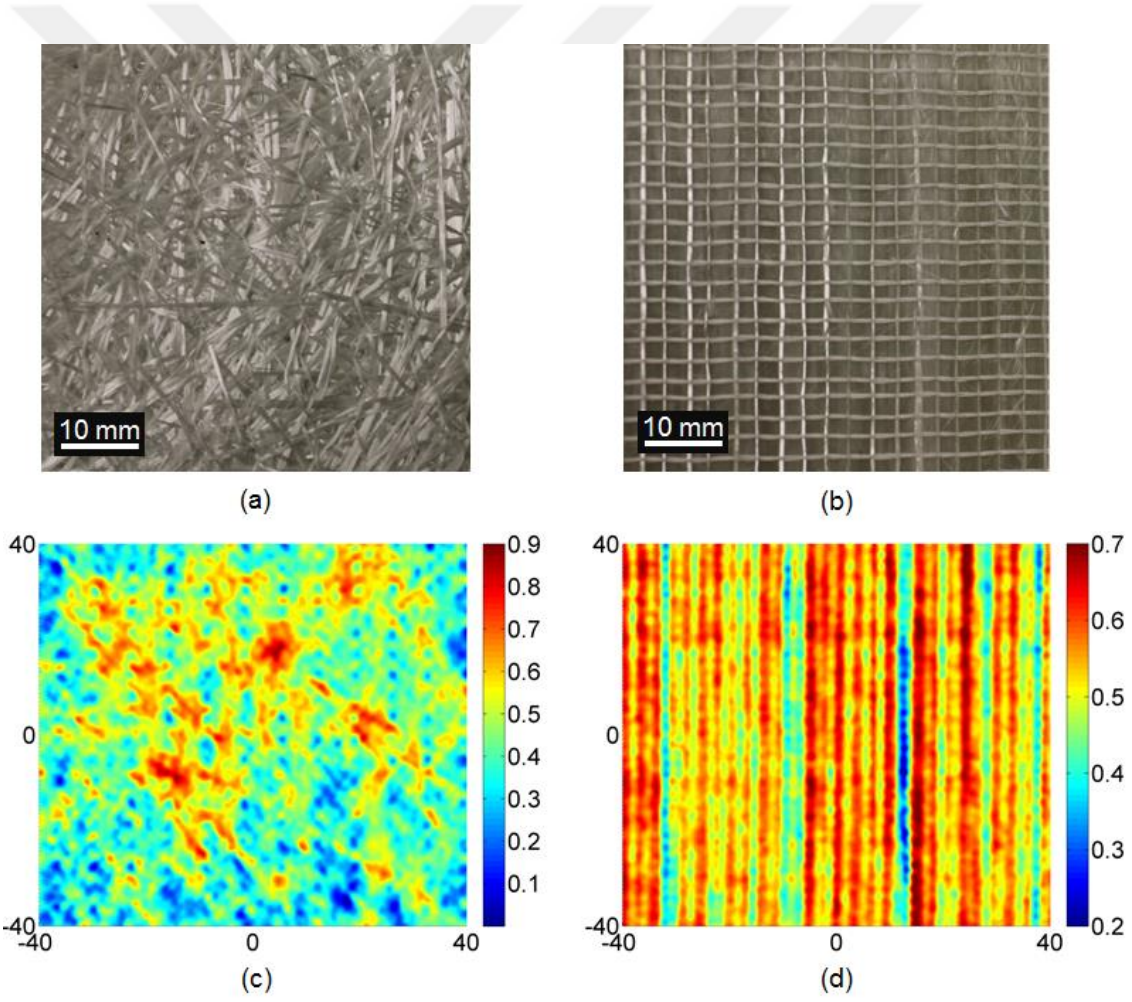

Figure 3.5 (a) Random and (b) biaxial fabrics used in this study. (c) - (d) Thickness distributions of 80mm×80mm samples under applied vacuum of 80 kPa (units in mm).

Eight layers of random and biaxial fabrics are used and placed as shown in Figure 3.5(a) and Figure 3.5(b) and after checking for any potential leakage, 80 kPa of vacuum is applied which in turn infused the resin into the part. In Case A (1D flow experiment), the instance when flow front reaches the tube at the exit is marked as $t = t_{fill}$. At this instant, the inlet is closed and excess resin is ventilated by bleeding through vent until $t = 2t_{fill}$. In Case B (2D flow experiment), resin arrived to the vents in the order of 1, 3, and 2. Vents 1 and 3 are closed 30 seconds after resin arrival to these vents. The instance when resin reaches the Vent 2 is marked as $t = t_{fill}$. At this instant, the inlet is closed in order to bleed excess resin. Second post-filling action is taken at $t = 1.5t_{fill}$ by converting the inlet (which was closed at $t = t_{fill}$) to a vent and post-filling stage continued with this configuration until $t = 2t_{fill}$.

To ensure that the SLS system is not affected from (i) the reflection into the optics of the camera and (ii) the changes in reflection and transparency of the surface that can occur during impregnation with resin, an experiment is designed as shown in Figure 3.6(a) with a vacuum bag divided into three regions: plain, tape-coated, and paint-coated vacuum bag. An instant during the experiment and the corresponding thickness distribution are shown in Figure 3.6(b) and Figure 3.6(c), respectively. Figure 3.6(c) shows that the system is capable of measuring the thickness of the specimen in all three regions and thickness is slightly higher in coated regions (both tape and paint). Though it is not visually evident from Figure 3.6(c), system could not measure the thickness of several points in plain vacuum bag region due to strong reflection into the optics of the camera. In addition, this region is prone to changes of reflectivity by resin arrival. Whereas, paint coating does not allow visual tracking of flow front as seen in Figure 3.6(b), thus tape is used

for coating the vacuum bag in the experiments and its thickness is accounted for in the post-processing stage.

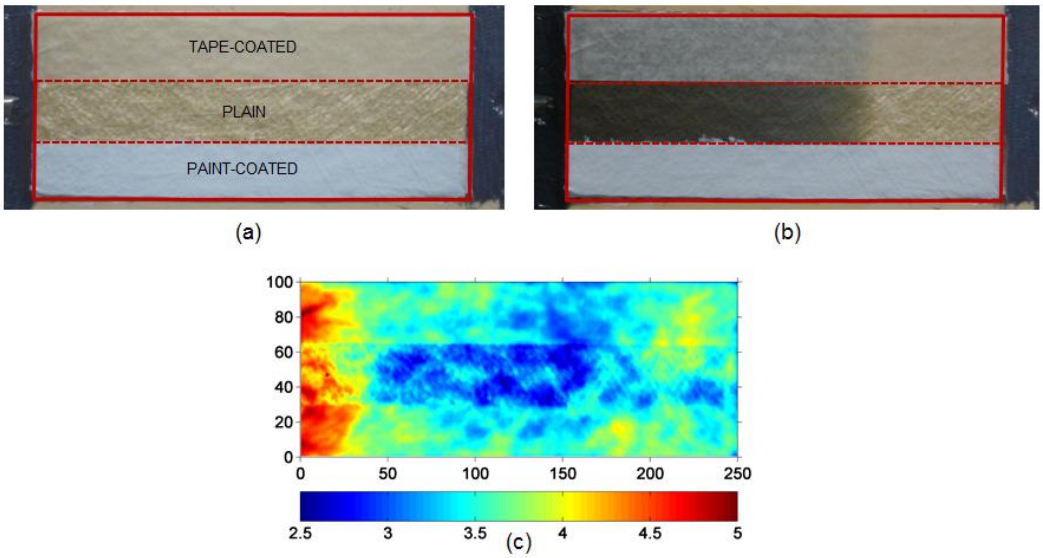

Figure 3.6 (a) Three regions with different coatings. (b) Flow propagation through the specimen. (c) Thickness distribution of the specimen (units in mm).

3.3.1. Compaction characterization

Compaction of random and biaxial fabric reinforcements are characterized to identify the relationship between compaction pressure, P_c, and its fiber volume fraction, ϕ_f, for dry and wet cases. According to Terzhaghi's principle [74], P_c is defined as difference between atmospheric pressure, P_{atm}, and resin pressure, P

$$P_c = P_{atm} - P \tag{3.8}$$

and fiber volume fraction, ϕ_f, is defined as the ratio of the fiber volume to volume of the fabric specimen and calculated as

$$\phi_f = \left(n\rho_{sup}\right)/(h\rho_{bulk}) \tag{3.9}$$

where n is the number of fabric layers, ρ_{sup} is the superficial density of a single fabric layer, h is the thickness of the fabric specimen and ρ_{bulk} is the bulk density of the fibers.

In compaction experiments, a dry specimen is placed on a flat acrylic mold and covered by a vacuum bag. Vacuum pressure is set to 2, 10, 20, 40, 60, and 80 kPa and kept constant for 5 minutes at each vacuum level to allow for thickness to settle. While specimen is under vacuum pressure of 80 kPa, it is impregnated with resin, in approximately 15 seconds, and vacuum pressure is decreased from 80 kPa to 60, 40, 20, 10, and 2 kPa again by keeping it constant for 5 minutes at each level. Thickness is measured using the SLS system at the end of each 5 minute interval and experiment is repeated for three times for both fabric types.

A power law is fitted to the experimental results

$$v_f = AP_c^B \tag{3.10}$$

to determine the constants A and B. The values of A and B for both fabric types are presented in

Table 3.3. Results of compaction experiments and power law fits are presented in Figure 3.7.

Table 3.3 Compaction model coefficients

		A [1/Pa]	B
Random Fabric	Dry loading	0.0567	0.1753
	Wet unloading	0.1525	0.0927
Biaxial Fabric	Dry loading	0.2197	0.0792
	Wet unloading	0.3608	0.0384

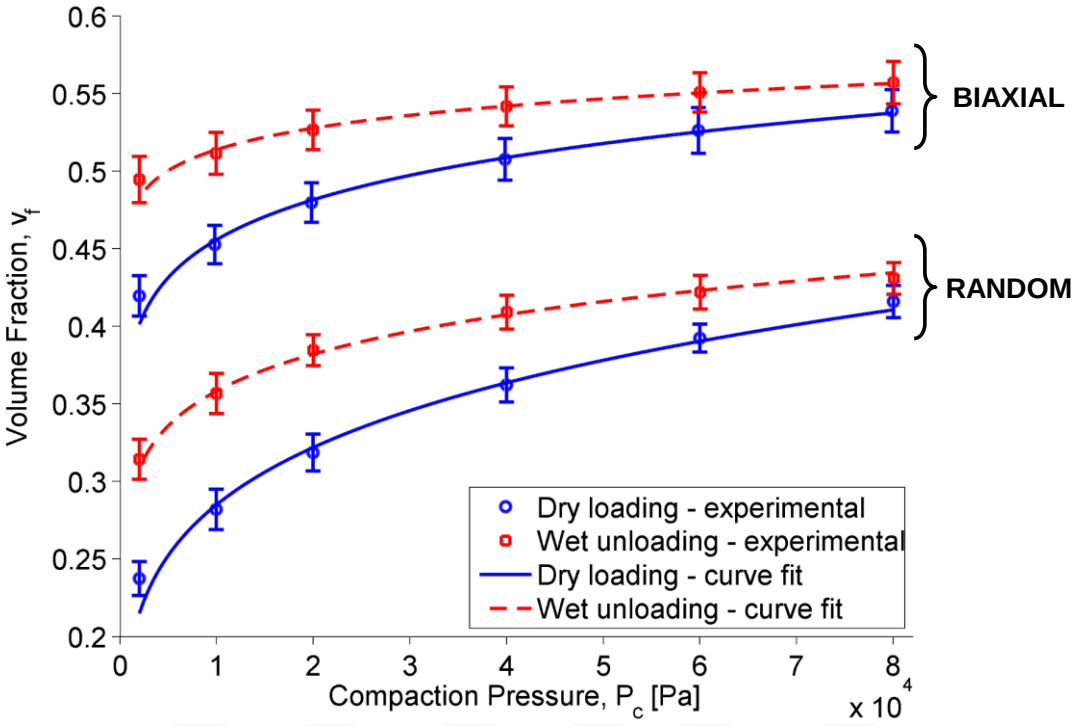

Figure 3.7 Compaction experiment results of both fabrics and corresponding curve fits. See

Table 3.3 for coefficients of the fitted curves.

3.3.2. Permeability characterization

In-plane permeability of the reinforcements used in this study are characterized for unsaturated and saturated flow conditions. Details of the experimental setup, experimental procedure and results are reported elsewhere [12]. The following exponential function is fitted to the saturated and unsaturated permeability experiments separately:

$$K = Ce^{-D\phi_f} \tag{3.11}$$

and the constants C and D are determined.

The constants for unsaturated and saturated flow conditions are presented in Table 3.4. It should be noted that unsaturated permeability values are used in mold-filling modeling since the nature of the unsaturated permeability characterization experiments is similar to the transient filling stage in VI. Saturated permeability values are used in post-filling modeling due to the similarity between the nature of post-filling stage in VI and saturated permeability characterization experiments.

Table 3.4 Permeability model coefficients in [12]. Range of applicability is $0.22 < \phi_f < 0.50$ for random fabric and $0.33 < \phi_f < 0.55$ for biaxial fabric.

		C [m^2]	D
Random Fabric	Unsaturated	3.06 E-09	9.91
	Saturated	8.58 E-09	7.93
Biaxial Fabric	Unsaturated	2.22 E-07	16.05
	Saturated	1.08 E-06	21.61

3.4. Modeling

Combining Darcy's law (Eq. (1.1)) and continuity equation (Eq. (1.3)) yields

$$\frac{\partial h}{\partial t} - \nabla \cdot \left(h \frac{[K]}{\mu} \cdot \nabla P \right) = 0 \tag{3.12}$$

In literature, Eq. (3.12) and its equivalents are solved [116,117] or it can be further re-arranged as follows using chain rule

$$\frac{\partial h}{\partial \phi_f} \frac{\partial \phi_f}{\partial P} \frac{\partial P}{\partial t} - \nabla \cdot \left(h \frac{[K]}{\mu} \cdot \nabla P \right) = 0 \tag{3.13}$$

where $\frac{\partial h}{\partial \phi_f}$ is calculated using Eq. (3.9) and $\frac{\partial \phi_f}{\partial P}$ is calculated using Eq. (3.10).

3.4.1. Solution of pressure

In this study, Eq. (3.13) is solved to obtain P using 4-node hierarchical (diagonally dominant) rectangular finite elements (see Figure 3.8). Elements with side length of 2 mm in both directions (*i.e.*, square elements) are used, after verifying the convergence of the simulated fill times with decreasing side length. Galerkin's approximation is adopted and the corresponding finite element formulation is in the following form

$$[M]\{\dot{P}\} + [C]\{P\} = \{F\} \tag{3.14}$$

where, owing to the solid mechanics literature, $[M]$ is the mass matrix, $[C]$ is the stiffness matrix, $\{F\}$ is the flow vector and $\{\dot{P}\}$ is the first order time derivative vector of resin pressure vector, $\{P\}$. Here, a lumped mass matrix rather than a consistent mass matrix is used to avoid numerical difficulties in transient solution. Mass matrix is constructed for each element, e, and assembled into the global mass matrix, $[M]$

$$[M^e] = \int_{\Omega_e} c_1^e \psi_i^e \, d\Omega \qquad i = 1,2,3,4 \tag{3.15}$$

where $c_1^e = \frac{\partial h^e}{\partial \phi_f^e}\frac{\partial \phi_f^e}{\partial P^e}$ is calculated at the centroid of the element, e, by averaging the nodal values, ψ_i^e is the linear interpolation function, and Ω_e is the domain of the element. Similarly, global stiffness matrix is assembled by first constructing the stiffness matrix at each element, using

$$[C^e] = \int_{\Omega_e} \left[c_2^e \left(\frac{\partial \psi_i^e}{dx}\frac{\partial \psi_j^e}{dx} \right) + c_3^e \left(\frac{\partial \psi_i^e}{dy}\frac{\partial \psi_j^e}{dy} \right) \right] d\Omega \qquad i,j = 1,2,3,4 \tag{3.16}$$

where $c_2^e = \frac{h^e K_{xx}^e}{\mu}$ and $c_3^e = \frac{h^e K_{yy}^e}{\mu}$. h^e is the thickness, K_{xx}^e and K_{yy}^e are the permeability in x and y directions, respectively.

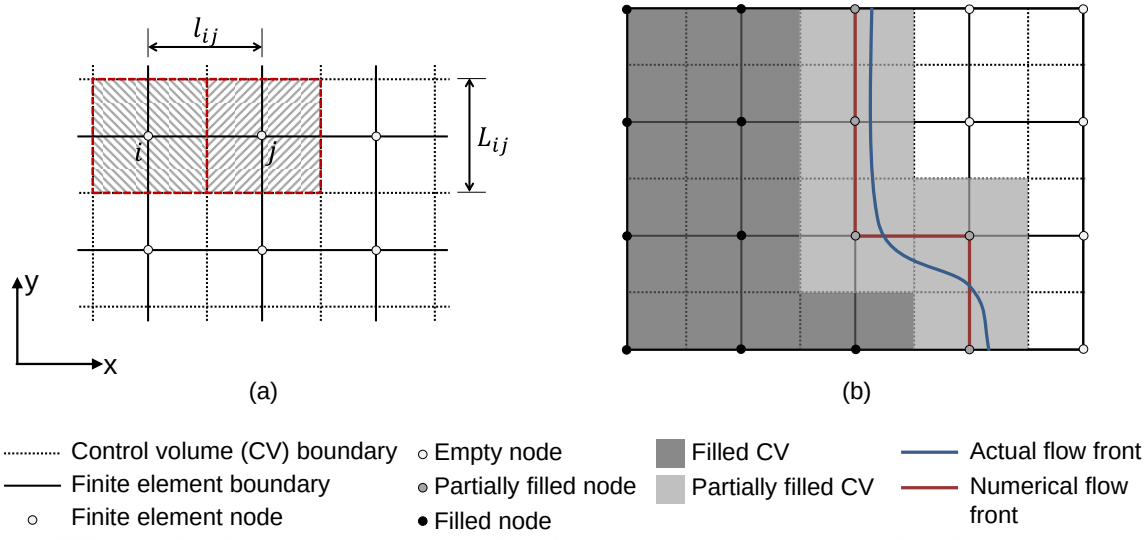

Figure 3.8 Details of the finite elements and control volumes used throughout the study.

Dry and wet reinforcements are known to have different compaction characteristics due to the lubrication and nesting of the fabric layers when they are wetted [75]. To account for the thickness difference between dry and wet states, compaction behavior is characterized for both dry and wet states (see *Materials and Experimental Methods* section) and the corresponding compaction curve fits are used in the simulations in order to calculate the thickness of the specimens.

Flow propagation is handled by defining a term, S, to denote the saturation at each nodal control volume (CV) where S can get any value between 0 and 1 (0 for completely dry state and 1 for completely saturated state) and detailed in the following section. To avoid any discontinuity in the thickness distribution at the nodes around the flow front, which can arise from the difference between dry and wet thickness for a given pressure, thickness of a node i located at the flow front is calculated by using rule of mixture

$$h_i = S_i h_{wet}(P_{c,i}) + (1 - S_i)\, h_{dry}(P_{c,i}) \tag{3.17}$$

where h_i is the thickness, S_i is the saturation, $P_{c,i}$ is the compaction pressure on the i^{th} node. $h_{dry}(P_{c,i})$ and $h_{wet}(P_{c,i})$ are thicknesses at $P_{c,i}$ when the fabric preform is completely dry and wet, respectively.

Flow vector is assembled for each element as

$$\{F^e\} = \int_{\Gamma_e} \vec{u} \cdot \vec{n}\, d\Gamma \tag{3.18}$$

where Γ_e is the boundary of the element domain and $\vec{n}$ is the outward normal unit vector on the domain. Flow vector is non-zero if it is defined as the injection gate for which flow rate can be prescribed as in a constant-flow-rate RTM case. Otherwise, if the pressure is controlled at the inlet and vent, as in the cases of constant-pressure RTM and VI, pressure can be prescribed to the corresponding elements of $\{P\}$ vector.

Evolution of pressure is modeled by solving Eq. (3.14) using Euler method, as summarized in [118,119], according to

$$[M]_n \frac{\{P\}_{n+1} - \{P\}_n}{\Delta t} + [C]_n \{P\}_n = \{F\}_n \tag{3.19}$$

where n denotes n^{th} time step. By re-arranging Eq. (3.19)

$$[M]_n \{P\}_{n+1} = \Delta t\, \{F\}_n + ([M]_n - \Delta t\, [C]_n)\, \{P\}_n \tag{3.20}$$

$\{P\}_{n+1}$ is computed for a pre-determined Δt where Δt is should be lower than the critical time step size Δt_{cr} which is calculated as

$$\Delta t_{cr} = \frac{2}{\lambda_{max}} \tag{3.21}$$

where λ_{max} is the largest eigenvalue of the system such that

$$([M]_n - \lambda [C]_n)\{P\}_n = \{F\}_n \tag{3.22}$$

In conventional CVFEM solvers, time step size is equal to the time required to fill the CV to be filled the earliest [72]. This approach assumes that material properties do not change between the successive steps of solution, which holds true for RTM where the specimen thickness (thus, fiber volume fraction) is constant, therefore permeability (a function of fiber volume fraction), does not change over time. However, in case of VI, thickness, as well as the permeability, is subject to change as flow propagates. The most straightforward way to achieve high accuracy in the presence of varying properties is to refine the mesh which results in smaller time steps, to increase the accuracy at an expense of computational load [70,120].

Here in this study, a new method is proposed which allows for time integration solution with time steps smaller than the time required to fill the CV to be filled the earliest. A graphical comparison between conventional CVFEM solver and the proposed method is given in Figure 3.9(a) and Figure 3.9(b).

In the post-filling stage, evolution of pressure is solved using Eq. (3.20) similar to the filling stage. However, the mold is completely filled in this stage, hence saturated permeability experiments are considered for modeling the permeability behavior. Similarly, for modeling the compaction behavior of the fabric, results obtained by wet specimens are considered.

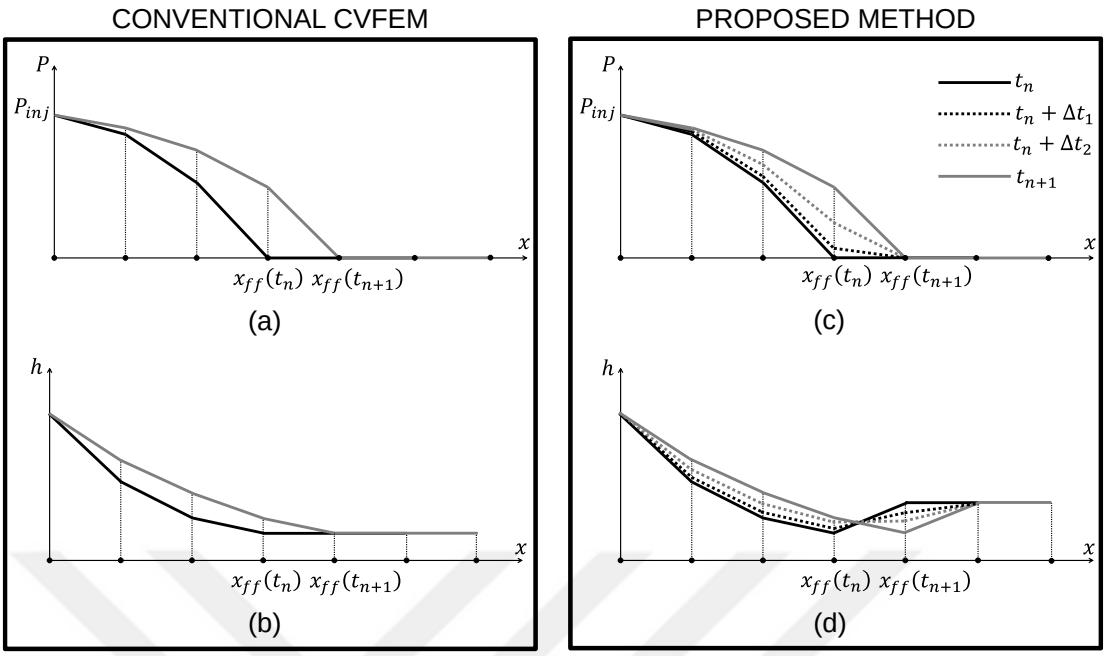

Figure 3.9 Comparison of conventional CVFEM method and proposed method. Evolution of pressure ((a) and (b)) and evolution of thickness ((c) and (d)) between two successive updates of flow front location. x_{ff} denotes the flow front location.

3.4.2. Flow front propagation

As illustrated in Figure 3.9(c) and detailed in the previous section, evolution of pressure distribution over time is achieved by using time step sizes smaller than time required to fill the CV which is to be filled the earliest. In this approach, following the solution of pressure at each time step, t_n, resin flow to each control volume, i, at the flow front is from its filled neighbor control volumes, j, and it is updated using the following equation

$$q_i = \sum_{j=1}^{m} \Delta t \, h_{ij} \frac{K_{ij}}{\mu} \frac{P_j - P_i}{l_{ij}} L_{ij} \tag{3.23}$$

where m is the total number of filled neighbors of the control volume i, h_{ij} and K_{ij} are the average of the thicknesses and permeabilities, respectively, l_{ij} is the distance between the centers, and L_{ij} is the width of the common

surface of the control volumes i and j (see Figure 3.8). Saturation of control volume i is updated at each time step as

$$S_i(t_n) = S_i(t_{n-1}) + \frac{q_i}{V_i} \tag{3.24}$$

where V_i is the volume of the control volume i. As illustrated in Figure 3.9(d), thicknesses of the control volumes at the flow front change as it is saturated thus V_i is updated at each time step.

3.5. Results and discussion

3.5.1. Case A: 1D flow experiment

In the filling experiment, the part was filled in 1212 seconds (*i.e.*, t_{fill} = 1212 seconds) while in simulation it took 1160 seconds, resulting in a deviation of 5.9% between experimental and simulated fill times which is an acceptable deviation considering the inherent unpredictability of VI process that may arise due to the variation in material properties. Figure 3.10 shows the thickness distribution of the specimen in experiment and simulation at five different instants normalized with respect to the fill time, t_{fill} and these instants are $t = 0$, $t = 0.5t_{fill}$, $t = t_{fill}$, $t = 1.5t_{fill}$, $t = 2t_{fill}$. At $t = 0$, thickness is not uniform in the experimental result, due to the random structure of the fiber bundles within the layers of the random fabric. As flow front propagates, thickness around the inlet increases (see Figure 3.10, for $x <$ 150 mm at $t = 0.5t_{fill}$ and $t = t_{fill}$) due to decreasing compaction pressure (*i.e.*, increasing resin pressure, see Figure 3.12(b)). In the post-filling stage, specimen's thickness decreases since the excess resin is ventilated and a more uniform thickness distribution is achieved at the end of the post-filling stage (see also Figure 3.12(a) and the difference between Δh_{mold} at $t = t_{fill}$ and $t =$

$2t_{fill}$). Figure 3.10 shows that thickness is significantly lower in the vicinity of pressure sensors. The decrease of thickness around the pressure sensors is due to extensive deformation of specimen in these regions since pressure sensor surface is lower than the mold surface.

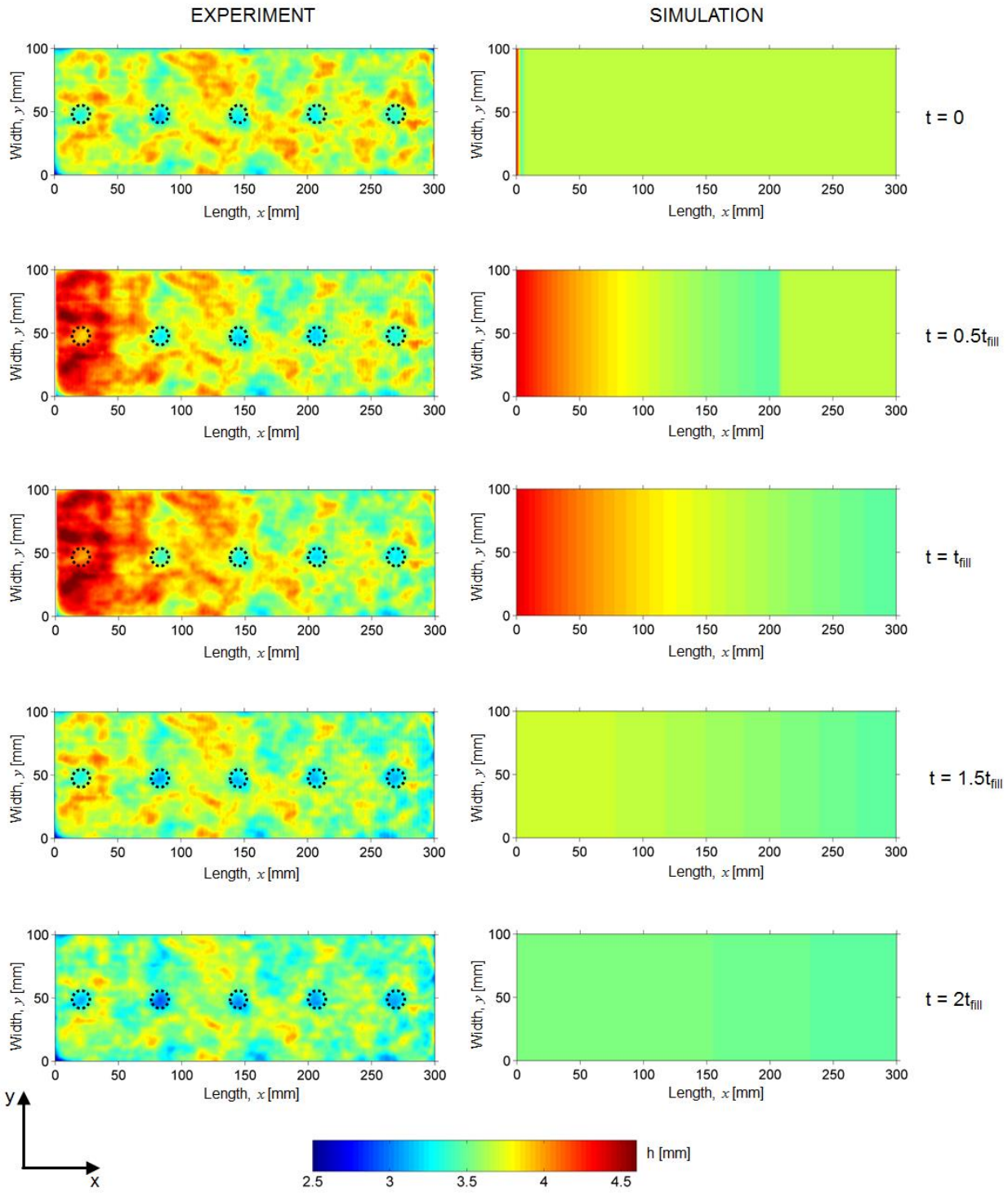

Figure 3.10 Thickness distribution at five different instants in the experiment and the simulation of Case A. Dashed circles in experimental results correspond to the pressure sensor locations.

Experimental and simulation results in Figure 3.10 look different than each other. However, one should be aware that fabric has inherent structural variation and it is observable in the experimental results. To make a comparison without taking the variation into account, one can take the average in the width (*i.e.*, y) direction and compare the thickness variation in length (*i.e.*, x) direction throughout the experiment by calculating $h(x,t)$. Herein, instead of using $h(x,t) = \frac{1}{L_y}\int_0^{L_y} h(x,y,t)dy$ to calculate the average thickness in the width direction, the following is used

$$h(x,t) = \frac{1}{90}\left(\int_0^{45} h(x,y,t)dy + \int_{55}^{100} h(x,y,t)dy\right) \tag{3.25}$$

in order to find the average thickness without taking into account the substantial decrease in thickness due to pressure sensors.

In Figure 3.11, change in thickness is presented as a function of distance to inlet and time normalized with respect to t_{fill}, namely $\sqrt{t^*}$. Change in thickness is calculated by subtracting the initial thickness, $h(x,0)$, from $h(x,t)$. As seen from Figure 3.11(a) and Figure 3.11(b), change in thickness is captured well by the simulation in both filling and post-filling stages (*i.e.*, $\sqrt{t^*} < 1$ and $\sqrt{t^*} > 1$, respectively) and the trends are similar in the simulation and the experimental results. In this figure, black circles indicates the flow front arrival in the experiment and dashed line indicates the flow front progression as a function of $\sqrt{t^*}$. In Figure 3.11(a), flow front arrival is followed by thinning due to further fiber nesting by lubrication effects and similarly a thinning occurs in simulation upon flow front arrival due to transition from dry to wet compaction as detailed in *Modeling* section.

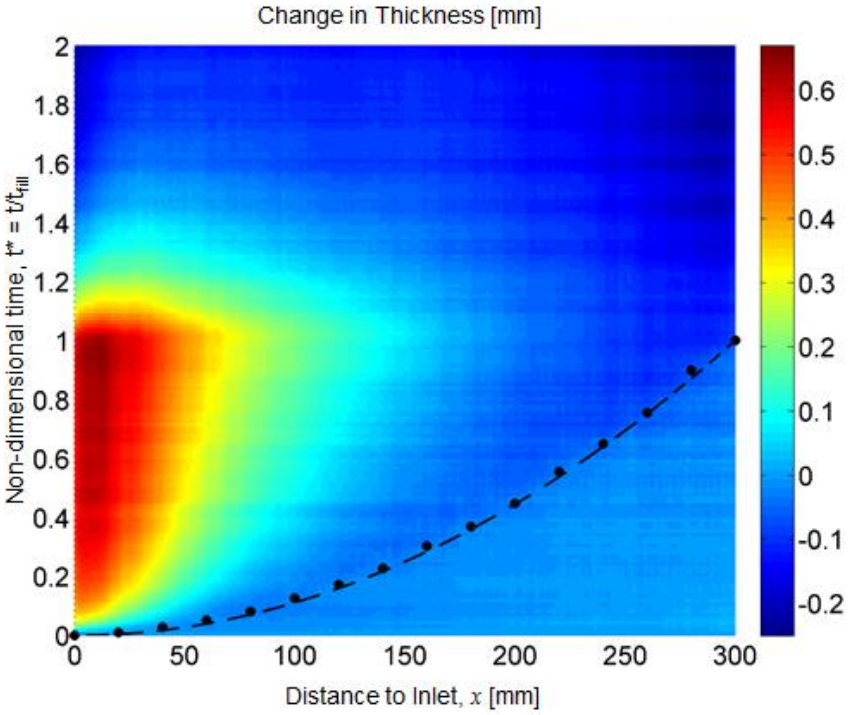

(a)

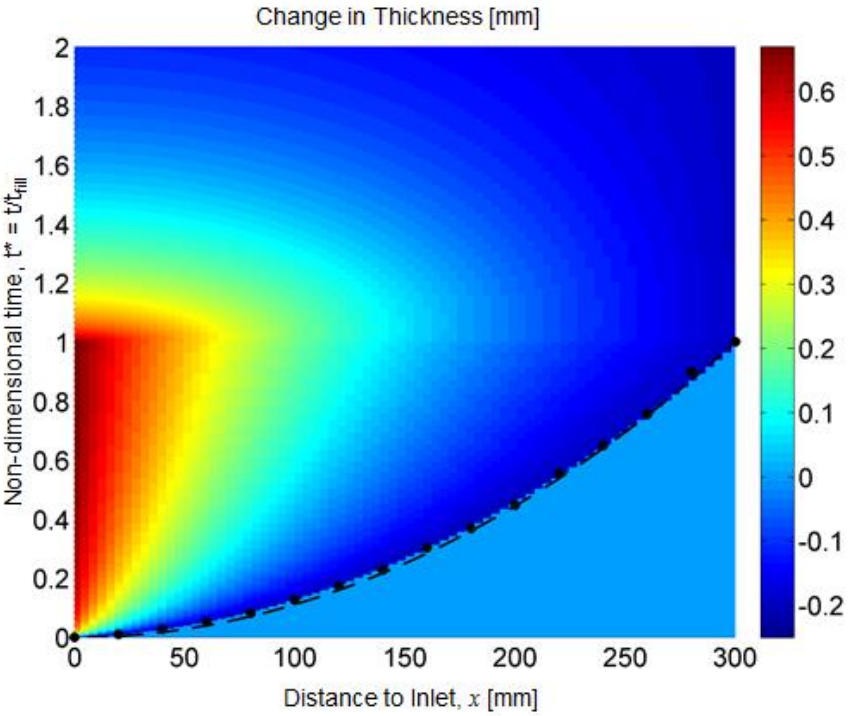

(b)

Figure 3.11 Change of thickness, with respect to the initial thickness, along the flow length of the part during (a) the experiment, (b) the simulation. In (a) and (b), black circles correspond to the flow front arrival in the experiment and dashed curve corresponds to flow front progression as a function of $\sqrt{t}$ (*i.e.*, $x = c\sqrt{t^*}$ where c is a constant).

Figure 3.12(a) shows the evolution of thickness at five different distances from the inlet (x = 25, 85, 145, 205, and 265 mm) which correspond to the distances of the centers of the pressure sensors to the inlet (see Figure 3.12(d)). Similarly, Figure 3.12(b) shows the evolution of pressure at the same locations. As seen in Figure 3.12(a), experimental and simulated thickness values follow similar trends in both filling and post-filling stages. Thickness variation, Δh_{mold} is 0.75 mm at the end of filling stage and it is reduced to 0.05 mm at the end of post-filling by resin bleeding. A sudden drop of thickness is observed in the simulated results and it corresponds to the transition from dry compaction to wet compaction when flow front reaches a location. In addition, the simulated thicknesses of the five points is slightly lower than the experimental ones in the filling stage (*i.e.*, $t^* < 1$), thus the part volume as well as volume of infused resin is slightly underestimated as shown in Figure 3.12(c). This underestimation might be contributing to the difference between the experimental (1212 seconds) and simulated (1160 seconds) fill times. The agreement between experimental and simulated pressures is very good in the filling stage and the slight difference between the two in the post-filling stage is suspected to be due to the relationship between the resin pressure and thickness (*i.e.*, compaction behavior). It should be noted that the wet compaction behavior is characterized in unloading (by decreasing P_c during the measurements) whereas P_c increases with time during the post-filling stage and this difference is likely to contribute significantly to the deviation between experimental and simulated pressure profiles in the post-filling stage [115].

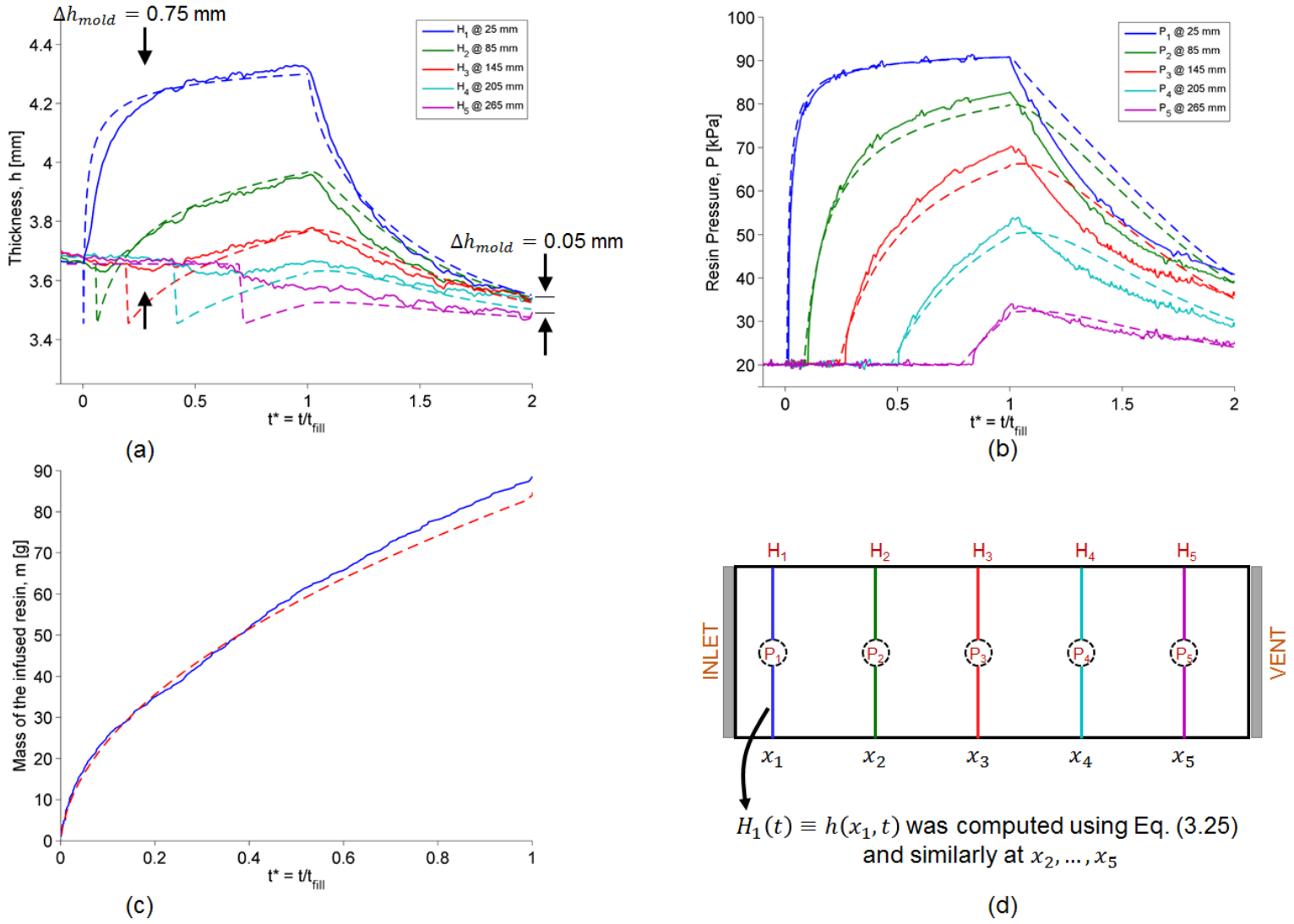

Figure 3.12 (a) Thickness and (b) resin pressure at five different locations and (c) mass of the infused resin in the experiment and the simulation of Case A. (d) Corresponding locations of thickness measurement (colored lines) and numbering of pressure sensors. In (a)-(c), continuous and dashed curves correspond to experimental and simulated results, respectively.

3.5.2. Case B: 2D flow experiment

Experimental and simulated fill times are 1312 seconds and 1343 seconds, respectively. The deviation between the fill times is 2.4%, significantly lower than the deviation in *1D Flow Experiment*. Significant reduction in the deviation is expected to be due to biaxial fabric having less inherent variability with respect to the random fabric used in 1D experiment.

Figure 3.13 shows the thickness distribution of the specimen in experiment and simulation at five different instants normalized with respect to the fill time, t_{fill}, and these instants are $t = 0$, $t = 0.5t_{fill}$, $t = t_{fill}$, $t = 1.5t_{fill}$, $t = 2t_{fill}$. Both experimental and simulated results demonstrate that, in filling stage, thickness variation within the specimen increases as flow propagates because regions close to the inlet get thicker due to decreasing P_c (or increasing P as seen in Figure 3.14(b) for sensors P_1, P_2, P_3 and P_4). In the experimental results shown in Figure 3.13, similar to Case A, the specimen has a lower thickness in the vicinity of the pressure sensors. In this figure, fiber bundles along the length direction of the specimen and wrinkles on the vacuum bag are visible. In addition to the qualitative comparison of thickness distribution in Figure 3.13, Figure 3.14(a) shows the evolution of thickness at five locations ($x = 5$, 50, 110, 170, and 230 mm; and $y = 80$ mm, also visualized in Figure 3.14(d)) during the filling and post-filling stages in order to provide a quantitative comparison of experimental and simulated thickness. In the experiment, a slight decrease is observed in the thicknesses of the three closest points to the inlet (denoted by H_1, H_2, and H_3 in Figure 3.14(a)) upon resin arrival and it is followed by an increase with time due to decreasing compaction pressure. However, thinning upon resin

arrival in the other two points (H_4 and H_5), is not followed by an increase due to relatively higher compaction pressure.

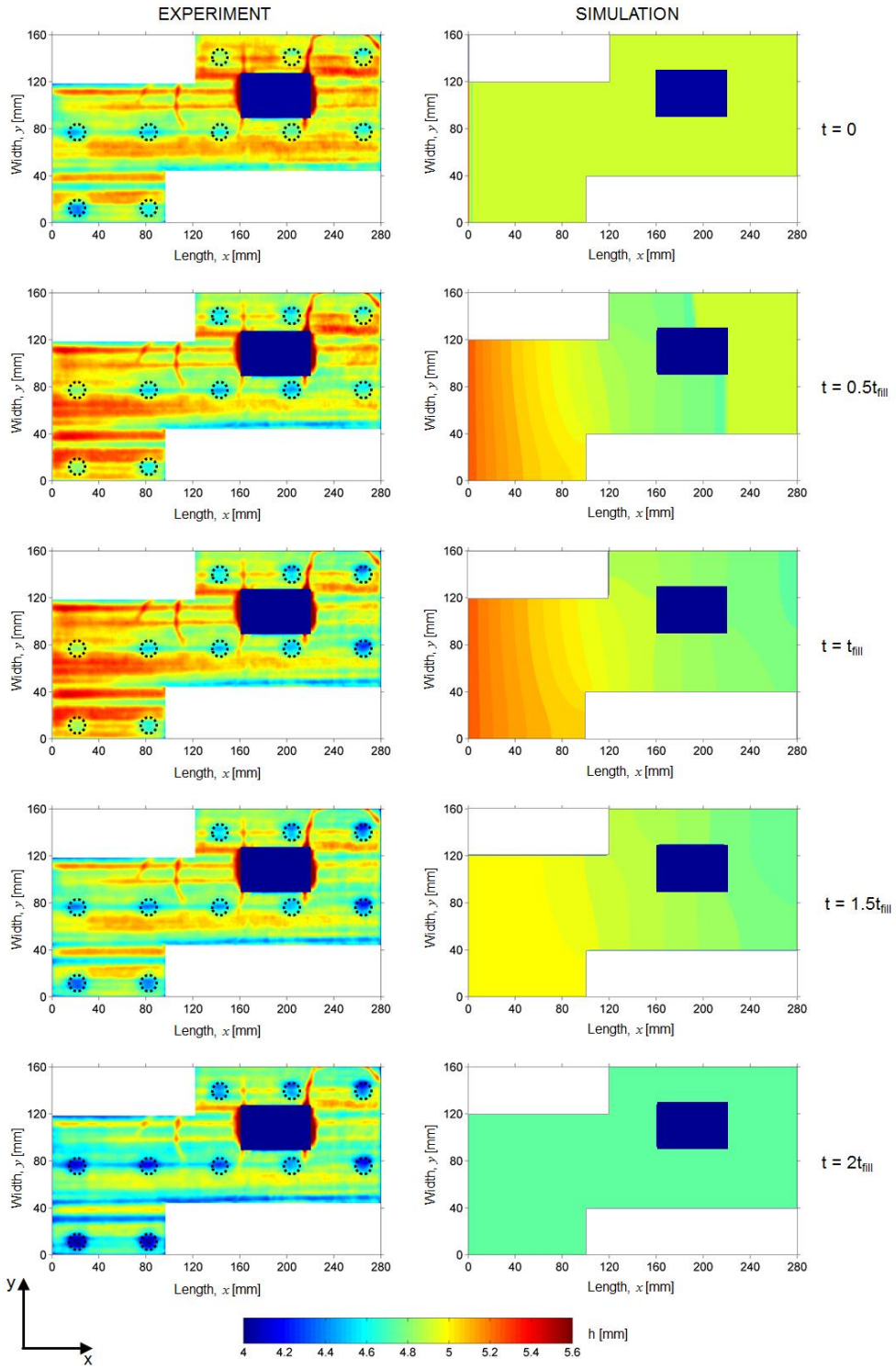

Figure 3.13 Thickness distribution at five different instants in experiment and in simulation of Case B. Dashed circles in experimental results correspond to the ten pressure sensor locations.

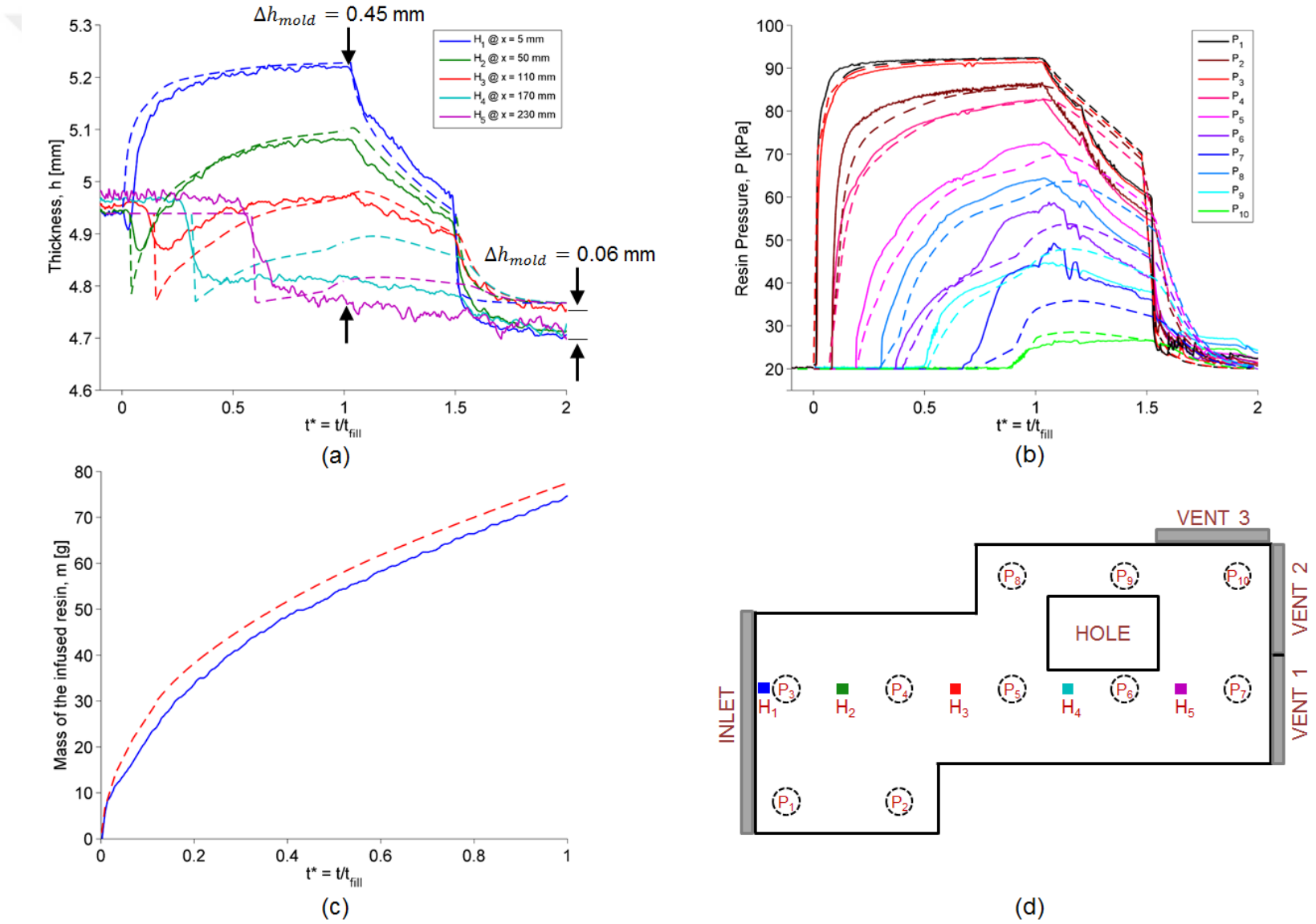

Figure 3.14 (a) Thickness at five different locations and (b) resin pressure, (c) mass of the infused resin as measured in the experiment and the simulation of Case B. (d) Corresponding points of thickness measurement (colored squares) and numbering of pressure sensors. In (a)-(c), continuous and dashed curves correspond to experimental and simulated results, respectively.

Simulated thickness matches well with the experimental thickness for the first three points (H_1, H_2, and H_3) while overestimating the thickness of the other two points (H_4 and H_5). As shown in Figure 3.14(c), mass of infused resin is slightly higher in the simulation which is in agreement with the overestimation of the thickness in simulation. It should be noted that the pressure cycle applied in the compaction experiments is similar to the pressure cycle around the inlet region in the filling experiment. Thus, the evolution of thickness is successfully modeled in this region by using the elastic compaction model. Good agreement between experimental and simulated pressure distributions in this region (see P_3, P_4 and P_5 in Figure 3.14(d), which are located close to H_1, H_2 and H_3) during the filling stage indicates that the flow propagation algorithm and elastic compaction model were successfully coupled.

Interestingly, pressure (P_6 and P_7) is underestimated in the simulation in the regions where thickness (H_4 and H_5) is overestimated. The contradiction between the pressure and thickness results in this region hints at the limitation of the selected compaction model to model time-dependent changes in thickness. Use of detailed compaction look-up tables [75,76,121] or viscoelastic compaction models [115,122,123] in modeling of LCM processes has the potential to model time-dependent changes in thickness. However, these strategies are out of scope and will be investigated in our continued studies.

Thickness variation is minimized in the post-filling stage and the effect of the two post-filling actions are distinctly visible in both experimental and simulated results. The aim of the post-filling actions is to ventilate the excess resin and since most of the excess resin is around the inlet region (evident by the

significantly higher thickness at the end of filling stage, (see H_1, H_2, and H_3 in Figure 3.14(a))), second post-filling action, where the inlet is converted to a vent, has a more significant effect in terms of reducing the thickness variation. At the end of the experiment, thicknesses of four of the five points (H_1, H_2, H_4, H_5) converge to values between 4.70 mm and 4.72 while the thickness of the point denoted by H_3 is 4.76 mm. Considering that the point H_3 is the furthest point to the vents activated in the post-filling stage, it takes longer to bleed the excess resin from H_3 in comparison to H_1, H_2, H_4 and H_5 and results in a relatively higher thickness. Nonetheless, thickness variation, Δh_{mold}, is reduced from 0.45 mm at the end of filling stage to 0.06 mm at the end of post-filling stage as a result of post-filling actions.

In the simulation, thickness distribution (see Figure 3.13 at $t = 2t_{fill}$ and Figure 3.14(a)) and pressure distribution (see Figure 3.14(b)) are more uniform at the end of the experiment. Simulated thickness values converge to 4.77 mm at the end of post-filling stage, close to the experimental thickness of the point H_3, thus the final thicknesses of the aforementioned four points (H_1, H_2, H_4, H_5) are slightly overestimated. In the simulation, two elastic compaction models are used, one for the dry state and one for the wet state; and the wet compaction model is used in both filling and post-filling stages. In reality, the specimen goes through another loading stage (increase in compaction pressure) in the post-filling stage and one may consider characterization of compaction under debulking cycles and use the results of the additional debulking cycles in order to model the compaction behavior in the post-filling stage. In our future work, we will focus on this issue by using more detailed compaction characterization strategies in order to cover a wide range of processing conditions.

3.6. Summary

In this study, a Structured Light Scanning (SLS) system was used for monitoring the full field thickness. SLS system was based on the use of a projector to project pre-determined fringe patterns on a surface and a camera to record the images of the surface with projected patterns; and in the post-processing stage recorded images were used for determining the thickness distribution with respect to a reference surface. SLS system was integrated to a lab scale Vacuum Infusion (VI) experiment setup and in addition to the full field thickness distribution, resin pressure at several points and the mass of the infused resin were measured during filling and post-filling stages of two different VI experiments. In these experiments, namely Case A and Case B, SLS system was able to capture the fabric texture, collapsed regions due to pressure sensor holes and even wrinkles on the vacuum bag in terms of instantaneous thickness distribution. In Case A and Case B, thickness variation within the mold, Δh_{mold}, was, respectively, 0.75 mm and 0.45 mm at the end of the filling stage and it was decreased to 0.05 mm and 0.06 mm at the end of post-filling stage as a result of post-filling actions to bleed out excess resin. In this study, SLS system results were analyzed in the post-processing stage, however, this system allows real-time or near real-time monitoring of thickness. Thus, SLS system can be used in online monitoring and online control of thickness in VI process.

A flow simulation tool, based on Control Volume Finite Element Method (CVFEM) with rectangular finite elements and using Euler method for time integration of pressure distribution, was developed; and permeability and compaction models of the fabrics were incorporated into the simulation. Simulations were performed by defining the part geometries and inlet/vent

configurations in accordance with the experiments. In Case A and Case B, fill times in simulation were close to fill times in experiment with deviations of 5.9% and 2.4%, respectively. Simulated results of pressure distribution and mass of the infused resin were in agreement with the experimental results in both cases and followed very similar trends. Thickening due to decreasing compaction pressure was modeled successfully in filling stage of both cases and yielded comparable results with the experiments. Similarly, thinning in the post-filling stage was modeled with a good agreement between experimental and simulated thickness results. Some discrepancies were observed between simulated and experimental thickness results (see evolution of H_4 and H_5 during filling stage (*i.e.*, $t^* < 1$) in Figure 12(a) and evolution of H_4 during filling stage (*i.e.*, $t^* < 1$) as well as the final thickness of H_3 in Figure 14(a)). These discrepancies were attributed to the limitation of elastic compaction models to account for the rate-dependent and time-dependent thickness changes. In our future studies, we will investigate the possibility of handling this shortcoming by integrating spring-damper based mechanical viscoelastic models and detailed compaction look-up tables to the presented CVFEM tool.

4. CONCLUSION

This thesis aimed at coupling experimental and numerical approaches for permeability characterization and flow monitoring in LCM processes. In Chapter 2, the effect of rigid spherical inclusions such as microcapsules and fillers on the permeability of textile fabrics is investigated by using glass beads as model inclusions. Glass beads with a range of diameters (40-70, 70-100, 100-200, 200-300, 300-400 and 400-800 μm) and volume fractions (2.5, 5 and10%) were sieved between layers of woven E-glass fabric whose volume fraction was fixed at 40%. Saturated permeability was measured experimentally and followed by X-ray microtomography to analyze the pore structure of the fabrics and estimate their permeability using (i) Computational Fluid Dynamics simulations and (ii) a Kozeny model taking into account the porosity and the specific surface. There was a good agreement between the normalized permeability trends of these three calculation methods. Furthermore, the analyses of spatial distributions of the beads, pore shape anisotropy, pore size distribution, and pore chord length showed that the alteration of permeability with respect to that of plain sample was closely linked to the changes in microstructural features. The coupling of permeability and microstructural features was taken one step further by

defining a threshold curve to relate bead diameter and bead volume fraction. Below this curve (relatively small diameter and/or low bead volume fraction) the sample permeability followed that of a packed textile without beads, and above it (relatively high diameter and/or high bead volume fraction) a strong departure from these values was observed, induced by strong distortions of the textile.

Considering the increasing popularity of FRPCs and increasing diversity of its applications, further functionalization of these materials will be of scientific and industrial interest in the future. Even though the results of this study is specific for a specific woven fabric, they are expected to provide an insight on influence of inclusions in other fabric types as well. In this sense, the analyses performed in this study can be extended to other fabric types to characterize the fabric-specific changes in the microstructure and permeability. Also, the permeability analysis can be extended to investigation of unsaturated permeability. Dynamic capillary effects already pose a challenging question for typical fabrics which exhibit a bimodal pore size distribution. Addition of inclusions alters the pore size distribution as well as the topology, so characterization of unsaturated permeability will definitely require an in-depth analysis at a finer scale by considering the capillary effects.

In Chapter 3, an alternative to trial and error based approach is offered to tackle the main hurdle of controlling the part thickness in VI for achieving repeatability during part manufacturing. To this end, experimental and numerical techniques were used: (i) thickness monitoring throughout filling and post-filling stages and (ii) resin flow modeling by taking into account compaction and permeability. A Structured Light Scanning (SLS) system is

verified for its suitability for monitoring thickness during VI and is used for full field thickness monitoring in experiments. A Control Volume Finite Element Method (CVFEM) solver, capable of coupling resin flow, compaction and permeability, is implemented. Two different scenarios are studied both experimentally and numerically. In the first scenario, a random glass fabric (with a superficial density of 450 g/m^2) is used to conduct a one-dimensional filling experiment on planar specimen with a rectangular shape. In the second scenario, a biaxial glass fabric (with a superficial density of 850 g/m^2) is used and a two-dimensional filling experiment is conducted on a specimen with more complex geometry. In both scenarios, mold filling is followed by a post-filling stage where the excess resin is bled out of the specimen. Full field thickness and resin pressure are recorded during filling and post-filling stages of experiments in addition to the mass of the infused resin during filling; and simulations are performed with corresponding process parameters. SLS system captured the evolution of thickness successfully during filling and post-filling stages of both scenarios. In both experiments, the vicinity of the resin inlet was significantly thicker than the regions that are filled the latest. Also, the overall specimen thickness as well as its variation was decreased in the post-filling stage of both experiments. Assigning different compaction and permeability models for filling and post-filling stages resulted in a good agreement between experiments and simulations in terms of thickness, pressure and fill times, and demonstrated the usefulness of this approach to predict the flow and thickness distributions in Vacuum Infusion.

In this study, elastic compaction models were used to relate the compaction pressure and fabric thickness. In elastic models, thickness changes

instantaneously when pressure changes, and recovers to its original value when the pressure on the material is removed. The use of elastic compaction models could be linked to the deviation of simulated thickness from the experimental thickness in the regions where the specimen undergoes significantly different pressure cycles than the pressure cycle in compaction experiments. To improve this shortcoming, use of the viscoelastic compaction models can be considered in future, since they take into consideration not only the instantaneous pressure but also the pressure history. However, these models are generally in the form of ordinary differential equations; thus coupling these models with resin flow is not straightforward.

Thickness monitoring was achieved by recording the image sets during the experiments and analyzing these images in the post-processing stage. However, each image set was obtained in a few seconds and can be further decreased by controlling the trigger timing of the camera and the projector. SLS system is already used in literature to get real time (or near real-time) surface profiling, usually at lower resolution or accuracy. Considering the increasing computational power, reduction of our analysis time to order of seconds seems acceptable. By achieving this task, SLS system can be used for online monitoring of thickness as well as for online control of thickness by creating a closed loop between the thickness input coming from SLS system and inlet/vent settings which can be based on on-off control or proportional control.

BIBLIOGRAPHY

[1] Advani SG, Sozer EM. Process Modeling in Composites Manufacturing 2002:436.

[2] Sozer EM, Bickerton S, Advani SG. On-line strategic control of liquid composite mould filling process. Compos Part A Appl Sci Manuf 2000;31:1383–94. doi:10.1016/S1359-835X(00)00060-9.

[3] Lawrence JM, Hsiao K-T, Don RC, Simacek P, Estrada G, Sozer EM, et al. An approach to couple mold design and on-line control to manufacture complex composite parts by resin transfer molding. Compos Part A Appl Sci Manuf 2002;33:981–90. doi:10.1016/S1359-835X(02)00043-X.

[4] Simacek P, Advani SG. Desirable features in mold filling simulations for Liquid Composite Molding processes. Polym Compos 2004;25:355–67. doi:10.1002/pc.20029.

[5] Mathur R, Fink BK, Advani SG. Use of genetic algorithms to optimize gate and vent locations for the resin transfer molding process. Polym Compos 1999;20:167–78. doi:Doi 10.1002/Pc.10344.

[6] Liu B, Bickerton S, Advani SG. Modelling and simulation of resin transfer moulding (RTM) - Gate control, venting and dry spot prediction. Compos

Part A Appl Sci Manuf 1996;27:135–41. doi:10.1016/1359-835X(95)00012-Q.

[7] Gokce A, Hsiao K-T, Advani SG. Branch and bound search to optimize injection gate locations in liquid composite molding processes. Compos Part A Appl Sci Manuf 2002;33:1263–72. doi:10.1016/S1359-835X(02)00047-7.

[8] Gokce A, Advani SG. Vent location optimization using map-based exhaustive search in liquid composite molding processes. Mater Manuf Process 2004;19:523–48. doi:Doi 10.1081/Amp-120038659.

[9] Caglar B, Yenilmez B, Sozer EM. Modeling of post-filling stage in vacuum infusion using compaction characterization. J Compos Mater 2015;49:1947–60. doi:10.1177/0021998314541305.

[10] Arbter R, Beraud JM, Binetruy C, Bizet L, Bréard J, Comas-Cardona S, et al. Experimental determination of the permeability of textiles: A benchmark exercise. Compos Part A Appl Sci Manuf 2011;42:1157–68. doi:10.1016/j.compositesa.2011.04.021.

[11] Vernet N, Ruiz E, Advani SG, Alms JB, Aubert M, Barburski M, et al. Experimental determination of the permeability of engineering textiles: Benchmark II. Compos Part A Appl Sci Manuf 2014;61:172–84. doi:10.1016/j.compositesa.2014.02.010.

[12] Yalcinkaya MA, Sarioglu A, Sozer EM. A novel mold design for one-continuous permeability measurement of fiber preforms. J Reinf Plast Compos 2015. doi:10.1177/0731684415581630.

[13] Lundström TS, Gebart BR, Sandlund E. In-plane permeability

measurements on fiber reinforcements by the multi-cavity parallel flow technique. Polym Compos 1999;20. doi:10.1002/pc.10342.

[14] Gebart BR, Lidstrom P. Measurement of in-plane permeability of anisotropic fiber reinforcements. Polym Compos 1996;17:43–51. doi:10.1002/pc.10589.

[15] Gauvin R, Trochu F, Lemenn Y, Diallo L. Permeability Measurement and Flow Simulation Through Fiber Reinforcement. Polym Compos 1996;17:34–42.

[16] Weitzenböck JR, Shenoi RA, Wilson PA. Radial flow permeability measurement. Part B: application. Compos Part A Appl Sci Manuf 1999;30:797–813. doi:10.1016/S1359-835X(98)00184-5.

[17] Slade J, Sozer EM, Advani SG. Fluid impregnation of deformed preforms. J Reinf Plast Compos 2000;19:552–68. doi:Doi 10.1106/Qj79-4797-Qala-Dkk1.

[18] Tanoglu M, Tugrul Seyhan A. Investigating the effects of a polyester preforming binder on the mechanical and ballistic performance of E-glass fiber reinforced polyester composites. Int J Adhes Adhes 2003;23:1–8. doi:10.1016/S0143-7496(02)00061-1.

[19] Fu S-Y, Feng X-Q, Lauke B, Mai Y-W. Effects of particle size, particle/matrix interface adhesion and particle loading on mechanical properties of particulate–polymer composites. Compos Part B Eng 2008;39:933–61. doi:10.1016/j.compositesb.2008.01.002.

[20] Lee GW, Park M, Kim J, Lee JI, Yoon HG. Enhanced thermal conductivity

of polymer composites filled with hybrid filler. Compos Part A Appl Sci Manuf 2006;37:727–34. doi:10.1016/j.compositesa.2005.07.006.

[21] Aktas L, Dharmavaram S, Hamidi YK, Altan MC. Filtration and Breakdown of Clay Clusters during Resin Transfer Molding of Nanoclay/Glass/Epoxy Composites. J Compos Mater 2008;42:2209–29. doi:10.1177/0021998308094556.

[22] Reia Da Costa EF, Skordos AA, Partridge IK, Rezai A. RTM processing and electrical performance of carbon nanotube modified epoxy/fibre composites. Compos Part A Appl Sci Manuf 2012;43:593–602. doi:10.1016/j.compositesa.2011.12.019.

[23] Chisholm N, Mahfuz H, Rangari VK, Ashfaq A, Jeelani S. Fabrication and mechanical characterization of carbon/SiC-epoxy nanocomposites. Compos Struct 2005;67:115–24. doi:10.1016/j.compstruct.2004.01.010.

[24] Kessler MR, Sottos NR, White S. Self-healing structural composite materials. Compos Part A Appl Sci Manuf 2003;34:743–53. doi:10.1016/S1359-835X(03)00138-6.

[25] Manfredi E, Cohades A, Richard I, Michaud V. Assessment of solvent capsule-based healing for woven E-glass fibre-reinforced polymers. Smart Mater Struct 2015;24:15019. doi:10.1088/0964-1726/24/1/015019.

[26] Zhang X, Wang P, Zhou Y, Li X, Yang E-H, Yu TX, et al. The effect of strain rate and filler volume fraction on the mechanical properties of hollow glass microsphere modified polymer. Compos Part B Eng 2016;101:53–63. doi:10.1016/j.compositesb.2016.06.079.

[27] Porfiri M, Gupta N. Effect of volume fraction and wall thickness on the elastic properties of hollow particle filled composites. Compos Part B Eng 2009;40:166–73. doi:10.1016/j.compositesb.2008.09.002.

[28] Kostornov AG, Moroz AL, Shapoval AA, Kabov O, Strizhak P, Legros JC. Composite structures with gradient of permeability to be used in heat pipes under microgravity. Acta Astronaut 2015;115:52–7. doi:10.1016/j.actaastro.2015.04.022.

[29] Tanoglu M, Seyhan AT. Compressive mechanical behaviour of E-glass/polyester composite laminates tailored with a thermoplastic preforming binder. Mater Sci Eng A 2003;363:335–44. doi:10.1016/j.msea.2003.08.005.

[30] Wu W, Klunker F, Xie L, Jiang B, Ziegmann G. Simultaneous binding and ex situ toughening concept for textile reinforced pCBT composites: Influence of preforming binders on interlaminar fracture properties. Compos Part A Appl Sci Manuf 2013;53:190–203. doi:10.1016/j.compositesa.2013.06.013.

[31] Hillermeier RW, Seferis JC. Interlayer toughening of resin transfer molding composites. Compos Part A Appl Sci Manuf 2001;32:721–9. doi:10.1016/S1359-835X(00)00088-9.

[32] Fu S-Y, Lauke B. Fracture resistance of unfilled and calcite-particle-filled ABS composites reinforced by short glass fibers (SGF) under impact load. Compos Part A Appl Sci Manuf 1998;29:631–41. doi:10.1016/S1359-835X(97)00111-5.

[33] Gupta N, Priya S, Islam R, Ricci W. Characterization of mechanical and electrical properties of epoxy-glass microballoon syntactic composites. Ferroelectrics 2006;345:1–12. doi:10.1080/00150190601018002.

[34] Wang P, Xu S, Li Z, Yang J, Zheng H, Hu S. Temperature effects on the mechanical behavior of aluminum foam under dynamic loading. Mater Sci Eng A 2014;599:174–9. doi:10.1016/j.msea.2014.01.076.

[35] Loix F, Badel P, Orgéas L, Geindreau C, Boisse P. Woven fabric permeability: From textile deformation to fluid flow mesoscale simulations. Compos Sci Technol 2008;68:1624–30. doi:10.1016/j.compscitech.2008.02.027.

[36] Di Fratta C, Klunker F, Trochu F, Ermanni P. Characterization of textile permeability as a function of fiber volume content with a single unidirectional injection experiment. Compos Part A Appl Sci Manuf 2015;C:238–47. doi:10.1016/j.compositesa.2015.05.021.

[37] Nordlund M, Fernberg SP, Lundström TS. Particle deposition mechanisms during processing of advanced composite materials. Compos Part A Appl Sci Manuf 2007;38:2182–93. doi:10.1016/j.compositesa.2007.06.009.

[38] Garay AC, Heck V, Zattera AJ, Souza JA, Amico SC. Influence of calcium carbonate on RTM and RTM light processing and properties of molded composites. J Reinf Plast Compos 2011;30:1213–21. doi:10.1177/0731684411416033.

[39] Gnidakouong JRN, Roh HD, Kim J, Park Y. In situ assessment of carbon nanotube flow and filtration monitoring through glass fabric using

electrical resistance measurement. Compos Part A Appl Sci Manuf 2016;90:137–46. doi:10.1016/j.compositesa.2016.07.005.

[40] Lefevre D, Comas-Cardona S, Binetruy C, Krawczak P. Modelling the flow of particle-filled resin through a fibrous preform in liquid composite molding technologies. Compos Part A Appl Sci Manuf 2007;38:2154–63. doi:10.1016/j.compositesa.2007.06.008.

[41] Lefevre D, Comas-Cardona S, Binetruy C, Krawczak P. Coupling filtration and flow during liquid composite molding: Experimental investigation and simulation. Compos Sci Technol 2009;69:2127–34. doi:10.1016/j.compscitech.2009.05.008.

[42] Haji H, Saouab A, Nawab Y. Simulation of coupling filtration and flow in a dual scale fibrous media. Compos Part A Appl Sci Manuf 2015;76:272–80. doi:10.1016/j.compositesa.2015.06.004.

[43] Reia Da Costa EF, Skordos AA. Modelling flow and filtration in liquid composite moulding of nanoparticle loaded thermosets. Compos Sci Technol 2012;72:799–805. doi:10.1016/j.compscitech.2012.02.007.

[44] Frishfelds V, Lundström TS. Modelling of particle deposition during impregnation of dual scale fabrics. Plast Rubber Compos 2011;40:65–9. doi:10.1179/174328911X12988622800936.

[45] Lundström TS, Frishfelds V. Modeling filtration of particulate flow during impregnation of dual-scale fabrics. J Compos Mater 2012;47:1907–15. doi:10.1177/0021998312452026.

[46] Hwang WR, Advani SG, Walsh SM. Direct simulations of particle

deposition and filtration in dual-scale porous media. Compos Part A Appl Sci Manuf 2011;42:1344–52. doi:10.1016/j.compositesa.2011.05.017.

[47] Yun M, Sas H, Simacek P, Advani SG. Characterization of 3D fabric permeability with skew terms. Compos Part A Appl Sci Manuf 2017;97:51–9. doi:10.1016/j.compositesa.2016.12.030.

[48] Shih CH, Lee LJ. Tackification of textile fiber preforms in resin transfer molding. J Compos Mater 2001;35:1954–81. doi:10.1177/002199801772661452.

[49] Rohatgi V, Lee LJ. Moldability of tackified fiber preforms in liquid composite molding. J Compos Mater 1997;31:720–44. doi:10.1177/002199839703100705.

[50] Estrada G, Vieux-Pernon C, Advani SG. Experimental characterization of the influence of tackifier material on preform permeability. J Compos Mater 2002;36:2297–310. doi:Doi 10.1106/002199802027542.

[51] Becker D, Mitschang P. Influence of preforming technology on the out-of-plane impregnation behavior of textiles. Compos Part A Appl Sci Manuf 2015;77:248–56. doi:10.1016/j.compositesa.2015.05.001.

[52] Rimmel O, Becker D, Mitschang P. Maximizing the out-of-plane-permeability of preforms manufactured by dry fiber placement. Adv Manuf Polym Compos Sci 2016;2:93–102. doi:10.1080/20550340.2016.1260900.

[53] Manfredi E, Michaud V. Packing and permeability properties of E-glass fibre reinforcements functionalised with capsules for self-healing

applications. Compos Part A Appl Sci Manuf 2014;66:94–102. doi:10.1016/j.compositesa.2014.07.006.

[54] Kessels JFA, Jonker AS, Akkerman R. Optimising the flow pipe arrangement for resin infusion under flexible tooling. Compos Part A Appl Sci Manuf 2007;38:2076–85. doi:10.1016/j.compositesa.2007.04.008.

[55] Sánchez F, Domenech L, García V, Montés N, Falcó A, Cueto E, et al. Fast and reliable gate arrangement pre-design of resin infusion processes. Compos Part A Appl Sci Manuf 2015;77:285–92. doi:10.1016/j.compositesa.2015.04.018.

[56] Sas HS, Simacek P, Advani SG. A methodology to reduce variability during vacuum infusion with optimized design of distribution media. Compos Part A Appl Sci Manuf 2015;78:223–33. doi:10.1016/j.compositesa.2015.08.011.

[57] Chung Hae Park, Woo L. Modeling void formation and unsaturated flow in liquid composite molding processes: a survey and review. J Reinf Plast Compos 2011;30:957–77. doi:10.1177/0731684411411338.

[58] Michaud V. A review of non-saturated resin flow in liquid composite moulding processes. Transp Porous Media 2016.

[59] Hammami A, Gebart BR. Analysis of the vacuum infusion molding process. Polym Compos 2000;21:28–40. doi:10.1002/pc.10162.

[60] Han K, Jiang S, Zhang C, Wang B. Flow modeling and simulation of SCRIMP for composites manufacturing. Compos Part A Appl Sci Manuf 2000;31:79–86. doi:10.1016/S1359-835X(99)00053-6.

[61] Kang M, Lee W Il, Hahn HT. Analysis of vacuum bag resin transfer molding process. Compos Part A Appl Sci Manuf 2001;32:1553–60. doi:10.1016/S1359-835X(01)00012-4.

[62] Correia N, Robitaille F, Long AC, Rudd CD, Simacek P, Advani SG. Analysis of the vacuum infusion moulding process: I. Analytical formulation. Compos Part A Appl Sci Manuf 2005;36:1645–56. doi:10.1016/j.compositesa.2005.03.019.

[63] Correia N, Robitaille F, Long AC, Rudd CD, Simacek P, Advani SG. Use of resin transfer molding simulation to predict flow, saturation, and compaction in the VARTM process. J Fluids Eng 2004;126:210–5. doi:10.1115/1.1669032.

[64] Joubaud L, Achim V, Trochu F. Numerical simulation of resin infusion and reinforcement consolidation under flexible cover. Polym Compos 2005;26:417–27. doi:10.1002/pc.20069.

[65] Celle P, Drapier S, Bergheau J-M. Numerical modelling of liquid infusion into fibrous media undergoing compaction. Eur J Mech - A/Solids 2008;27:647–61. doi:10.1016/j.euromechsol.2007.11.002.

[66] Bruschke M, Advani SG. A finite element/control volume approach to mold filling in anisotropic porous media. Polym Compos 1990;11:398–405. doi:10.1002/pc.750110613.

[67] Phelan F. Simulation of the injection process in resin transfer molding. Polym Compos 1997;18:460–76.

[68] Dong C (Jonathan). A modified rule of mixture for the vacuum-assisted

resin transfer moulding process simulation. Compos Sci Technol 2008;68:2125–33. doi:10.1016/j.compscitech.2008.03.019.

[69] Andersson HM, Lundström TS, Gebart BR. Numerical model for vacuum infusion manufacturing of polymer composites. Int J Numer Methods Heat Fluid Flow 2003;13:383–94. doi:10.1108/09615530310464553.

[70] Joshi SC, Lam YC, Liu X-L. Mass conservation in numerical simulation of resin flow. Compos Part A Appl Sci Manuf 2000;31:1061–8. doi:10.1016/S1359-835X(00)00067-1.

[71] Kang M, Lee W Il. A flow-front refinement technique for the numerical simulation of the resin-transfer molding process. Compos Sci Technol 1999;59:1663–74. doi:10.1016/S0266-3538(99)00029-9.

[72] Joshi SC. Reducing loss of resin flowing in porous fibrous media in simulation of composites fabrication. Polym Compos 2010;31:226–35. doi:10.1002/pc.20790.

[73] Samir J, Echaabi J, Hattabi M. Numerical algorithm and adaptive meshing for simulation the effect of variation thickness in resin transfer molding process. Compos Part B Eng 2011;42:1015–28. doi:10.1016/j.compositesb.2011.03.027.

[74] Govignon Q, Bickerton S, Kelly PA. Simulation of the reinforcement compaction and resin flow during the complete resin infusion process. Compos Part A Appl Sci Manuf 2010;41:45–57. doi:10.1016/j.compositesa.2009.07.007.

[75] Yenilmez B, Sozer EM. Compaction of e-glass fabric preforms in the

Vacuum Infusion Process, A: Characterization experiments. Compos Part A Appl Sci Manuf 2009;40:499–510. doi:10.1016/j.compositesa.2009.01.016.

[76] Yenilmez B, Senan M, Sozer EM. Variation of part thickness and compaction pressure in vacuum infusion process. Compos Sci Technol 2009;69:1710–9. doi:10.1016/j.compscitech.2008.05.009.

[77] Tackitt K, Walsh SM. Experimental study of thickness gradient formation in the VARTM process. Mater Manuf Process 2005;20:607–27. doi:10.1081/AMP-200041896.

[78] Williams CD, Grove SM, Summerscales J. The compression response of fibre-reinforced plastic plates during manufacture by the resin infusion under flexible tooling method. Compos Part A Appl Sci Manuf 1998;29:111–4. doi:10.1016/S1359-835X(97)00038-9.

[79] Yenilmez B, Akyol T, Caglar B, Sozer EM. Minimizing thickness variation in the Vacuum Infusion (VI) process. Adv Compos Lett 2011;20:157–67.

[80] Kessels JFA, Jonker AS, Akkerman R. Fully flow modeling of resin infusion under flexible tooling using unstructured meshes and wet and dry compaction properties. Compos Part A Appl Sci Manuf 2007;38:51–60. doi:10.1016/j.compositesa.2006.01.025.

[81] Yalcinkaya MA, Sozer EM. Effect of part thickness variation on the mold filling time in vacuum infusion process. J Reinf Plast Compos 2014;33:2136–50. doi:10.1177/0731684414554938.

[82] Govignon Q, Bickerton S, Morris J, Kelly PA. Full field monitoring of the resin flow and laminate properties during the resin infusion process.

Compos Part A Appl Sci Manuf 2008;39:1412–26. doi:10.1016/j.compositesa.2008.05.005.

[83] Govignon Q, Bickerton S, Kelly PA. Experimental investigation into the post-filling stage of the resin infusion process. J Compos Mater 2013;47:1479–92. doi:10.1177/0021998312448500.

[84] Andersson HM, Lundström TS, Gebart BR, Synnergren P. Application of digital speckle photography to measure thickness variations in the vacuum infusion process. Polym Compos 2003;24:448–55.

[85] Timms J, Bickerton S, Kelly PA. Laminate thickness and resin pressure evolution during axisymmetric liquid composite moulding with flexible tooling. Compos Part A Appl Sci Manuf 2012;43:621–30. doi:10.1016/j.compositesa.2011.12.012.

[86] Molimard J, Navarro L. Uncertainty on fringe projection technique: A Monte-Carlo-based approach. Opt Lasers Eng 2013;51:840–7. doi:10.1016/j.optlaseng.2013.01.023.

[87] Lemmens M. A survey on stereo matching techniques. Int Arch Photogramm Remote Sens 1988;27:11–23.

[88] Schindelin J, Arganda-Carreras I, Frise E, Kaynig V, Longair M, Pietzsch T, et al. Fiji: an open-source platform for biological-image analysis. Nat Methods 2012;9:676–82. doi:10.1038/nmeth.2019.

[89] Meijering E. FeatureJ: An ImageJ Plugin Suite for Image Feature Extraction 2003. http://www.imagescience.org/meijering/software/featurej/.

[90] Chalencon F, Orgéas L, Dumont PJJ, Foray G, Cavaillé JY, Maire E, et al.

Lubricated compression and X-ray microtomography to analyse the rheology of a fibre-reinforced mortar. Rheol Acta 2010;49:221–35. doi:10.1007/s00397-009-0393-5.

[91] Maire E, Colombo P, Adrien J, Babout L, Biasetto L. Characterization of the morphology of cellular ceramics by 3D image processing of X-ray tomography. J Eur Ceram Soc 2007;27:1973–81. doi:10.1016/j.jeurceramsoc.2006.05.097.

[92] Rolland du Roscoat S, Decain M, Thibault X, Geindreau C, Bloch JF. Estimation of microstructural properties from synchrotron X-ray microtomography and determination of the REV in paper materials. Acta Mater 2007;55:2841–50. doi:10.1016/j.actamat.2006.11.050.

[93] Koponen A, Kataja M, Timonen J. Permeability and effective porosity of porous media. Phys Rev E 1997;56:3319–25. doi:10.1103/PhysRevE.56.3319.

[94] Amico S, Lekakou C. Mathematical modelling of capillary micro-flow through woven fabrics. Compos Part A Appl Sci Manuf 2000;31:1331–44. doi:10.1016/S1359-835X(00)00033-6.

[95] Gebart BR. Permeability of unidirectional reinforcements for RTM. J Compos Mater 1992;26:1100–33. doi:10.1177/002199839202600802.

[96] Geodict, The Virtual Material Laboratory, Math2Market GmbH, www.geodict.com, Accessed 20 September 2016.

[97] Auriault J, Boutin C, Geindreau C. Homogenization of coupled phenomena in heterogenous media. John Wiley & Sons; 2010.

[98] Rolland du Roscoat S, Decain M, Geindreau C, Thibault X, Bloch J.

Microstructural analysis of paper using synchrotron X-ray microtomography: numerical estimation of the permeability and effective thermal conductivity. Appita J J Tech Assoc Aust New Zeal Pulp Pap Ind 2008;61:286–90.

[99] Chalencon F, Dumont PJJ, Orgéas L, Foray G, Cavaillé JY, Maire E. Homogeneous and heterogeneous rheology and flow-induced microstructures of a fresh fiber-reinforced mortar. Cem Concr Res 2016;82:130–41. doi:10.1016/j.cemconres.2015.12.012.

[100] Koivu V, Decain M, Geindreau C, Mattila K, Bloch J-F, Kataja M. Transport properties of heterogeneous materials. Combining computerised X-ray micro-tomography and direct numerical simulations. Int J Comut Fluid Dyn 2009;23:713–21. doi:10.1080/10618561003727512.

[101] Kuentzer N, Simacek P, Advani SG, Walsh SM. Permeability characterization of dual scale fibrous porous media. Compos Part A Appl Sci Manuf 2006;37:2057–68. doi:10.1016/j.compositesa.2005.12.005.

[102] Zhou F, Simacek P, Kuentzer N, Walsh SM, Advani SG. Analytic characterization of the permeability of dual-scale fibrous porous media. Compos Sci Technol 2006;66:2795–803. doi:10.1016/j.compscitech.2006.02.025.

[103] Amico S, Lekakou C. An experimental study of the permeability and capillary pressure in resin-transfer moulding. Compos Sci Technol 2001;61:1945–59. doi:10.1016/S0266-3538(01)00104-X.

[104] Michaud V, Mortensen A. Infiltration processing of fibre reinforced

composites: Governing phenomena. Compos - Part A Appl Sci Manuf 2001;32:981–96. doi:10.1016/S1359-835X(01)00015-X.

[105] Wolfrath J, Michaud V, Modaressi A, Manson JA. Unsaturated flow in compressible fibre preforms. Compos Part A Appl Sci Manuf 2006;37:881–9. doi:10.1016/j.compositesa.2005.01.008.

[106] Baranau V, Tallarek U. Random-close packing limits for monodisperse and polydisperse hard spheres. Soft Matter 2014;10:3826–41. doi:10.1039/c3sm52959b.

[107] Wang P, Drapier S, Molimard J, Vautrin A, Minni J-C. Characterization of Liquid Resin Infusion (LRI) filling by fringe pattern projection and in situ thermocouples. Compos Part A Appl Sci Manuf 2010;41:36–44. doi:10.1016/j.compositesa.2009.09.007.

[108] Huang PS, Zhang S. Fast three-step phase-shifting algorithm. Appl Opt 2006;45:5086–91.

[109] Zhang S. Recent progresses on real-time 3D shape measurement using digital fringe projection techniques. Opt Lasers Eng 2010;48:149–58. doi:10.1016/j.optlaseng.2009.03.008.

[110] Huang PS, Song Zhang. Novel method for structured light system calibration. Opt Eng 2006;45:83601. doi:10.1117/1.2336196.

[111] Huang PS, Hu Q, Jin F, Chiang F-P. Color-encoded digital fringe projection technique for high-speed three-dimensional surface contouring. Opt Eng 1999;38:1065. doi:10.1117/1.602151.

[112] Ghiglia D, Pritt M. Two-dimensional phase unwrapping: theory,

algorithms, and software. New York: Wiley; 1998.

[113] Dai J, Gong C, Zhang S. Three-dimensional shape measurement with dual reference phase maps. Opt Eng 2014;53:14102. doi:10.1117/1.OE.53.1.014102.

[114] Yenilmez B. Vacuum Infusion (VI) process modeling and material characterization with viscoelastic compaction models. Phd thesis. Koc University, 2014.

[115] Yenilmez B, Caglar B, Sozer EM. Pressure-controlled compaction characterization of fiber preforms suitable for viscoelastic modeling in the Vacuum Infusion process. J Compos Mater 2017.

[116] Simacek P, Eksik O, Heider D, Gillespie JW, Advani SG, Eksik Ö, et al. Experimental validation of post-filling flow in vacuum assisted resin transfer molding processes. Compos Part A Appl Sci Manuf 2012;43:370–80. doi:10.1016/j.compositesa.2011.10.002.

[117] Vilà J, González C, LLorca J. A level set approach for the analysis of flow and compaction during resin infusion in composite materials. Compos Part A Appl Sci Manuf 2014;67:299–307. doi:10.1016/j.compositesa.2014.09.002.

[118] Huebner KH, Dewhirst DL, Smith DE, Byrom TG. The finite element method for Engineers. 4th ed. John Wiley & Sons; 2001.

[119] Reddy JN. An introduction to the finite element method. 2nd ed. New York: McGraw-Hill; 1993.

[120] Maier RS, Rohaly TF, Advani SG, Fickie KD. A fast numerical method for

isothermal resin transfer mold filling. Int J Numer Methods Eng 1996;39:1405–17. doi:Doi 10.1002/(Sici)1097-0207(19960430)39:8<1405::Aid-Nme910>3.0.Co;2-S.

[121] Yenilmez B, Sozer EM. Compaction of e-glass fabric preforms in the vacuum infusion process: (a) use of characterization database in a model and (b) experiments. J Compos Mater 2012;47:1959–75. doi:10.1177/0021998312453075.

[122] Bickerton S, Buntain MJ, Somashekar AA. The viscoelastic compression behavior of liquid composite molding preforms. Compos Part A Appl Sci Manuf 2003;34:431–44. doi:10.1016/S1359-835X(03)00088-5.

[123] Kelly PA, Umer R, Bickerton S. Viscoelastic response of dry and wet fibrous materials during infusion processes. Compos Part A Appl Sci Manuf 2006;37:868–73. doi:10.1016/j.compositesa.2005.02.008.